ANGLE-RESOLVED PHOTOEMISSION SPECTROSCOPY OF $Sr_{1-x}La_xCuO_2$ THIN FILMS GROWN BY MOLECULAR-BEAM EPITAXY

A Dissertation

Presented to the Faculty of the Graduate School

of Cornell University

in Partial Fulfillment of the Requirements for the Degree of

Doctor of Philosophy

by

John Wallace Harter

May 2013

ANGLE-RESOLVED PHOTOEMISSION SPECTROSCOPY OF $Sr_{1-x}La_xCuO_2$ THIN FILMS GROWN BY MOLECULAR-BEAM EPITAXY

John Wallace Harter, Ph.D.

Cornell University 2013

Among the multitude of known cuprate material families and associated structures, the archetype is "infinite-layer" $ACuO_2$, where perfectly square and flat CuO_2 planes are separated by layers of alkaline earth atoms. The infinite-layer structure is free of magnetic rare earth ions, oxygen chains, orthorhombic distortions, incommensurate superstructures, ordered vacancies, and other complications that abound among the other material families. Furthermore, it is the only cuprate that can be made superconducting by both electron and hole doping, making it a potential platform for decoding the complex many-body interactions responsible for high-temperature superconductivity. Research on the infinite-layer compound has been severely hindered by the inability to synthesize bulk single crystals, but recent progress has led to high-quality superconducting thin film samples.

Here we report *in situ* angle-resolved photoemission spectroscopy measurements of epitaxially-stabilized $Sr_{1-x}La_xCuO_2$ thin films grown by molecular-beam epitaxy. At low doping, the material exhibits a dispersive lower Hubbard band typical of other cuprate parent compounds. As carriers are added to the system, a continuous evolution from Mott insulator to superconducting metal is observed as a coherent low-energy band develops on top of a concomitant remnant lower Hubbard band, gradually filling in the Mott gap. For $x = 0.10$, our results reveal a strong coupling between electrons and (π, π) antiferromagnetism, inducing a Fermi surface reconstruction that pushes the nodal states below the Fermi level and realizing nodeless superconductivity. Electron diffraction mea-

surements indicate the presence of a surface reconstruction that is consistent with the polar nature of $Sr_{1-x}La_xCuO_2$.

Most knowledge about the electron-doped side of the cuprate phase diagram has been deduced by generalizing from a single material family, $Re_{2-x}Ce_xCuO_4$, where robust antiferromagnetism has been observed past $x \approx 0.14$. In contrast, in all hole-doped cuprates, Néel order is rapidly suppressed by $x \approx 0.03$, with superconductivity following at higher doping levels. Studies of cuprates, however, often yield material-specific features that are idiosyncratic to particular compounds. By studying a completely different electron-doped cuprate, we can for the first time independently confirm that the cuprate phase diagram is fundamentally asymmetric and provide a coherent framework for understanding the generic properties of all electron-doped cuprates.

BIOGRAPHICAL SKETCH

John Harter was born in Syracuse—just one hour north of Cornell—in the summer of 1984. From a very young age, he demonstrated an unrelenting curiosity about the natural world and dreamed of becoming a scientist. When he was seven years old, John's parents decided they were fed up with the weather of central New York and moved the family to sunny Florida. There, high school presented John's first exposure to physics, and he fell in love with its beauty and simplicity. In 2002, he was salutatorian of his high school graduating class and moved to Gainesville to attend the University of Florida. He majored in physics and mathematics after reluctantly dropping a third major—chemistry. During the last year of his undergraduate education, John performed theoretical research on superconductivity under the advisement of Professor Peter Hirschfeld, published his first manuscript, and earned a National Science Foundation Graduate Research Fellowship. In 2006, he graduated *summa cum laude* with Bachelor of Science degrees in physics and mathematics and moved to Ithaca to start graduate school at Cornell University. There he became the first student to join Professor Kyle Shen's new research group, helping to build the laboratory up from scratch. He received a Master of Science degree in physics from Cornell in 2010 while pursuing research on angle-resolved photoemission spectroscopy of thin films grown by molecular-beam epitaxy. The results of this research would eventually form his doctoral dissertation, presented here.

"The electron is not as simple as it looks."

— Sir William Lawrence Bragg

ACKNOWLEDGEMENTS

Graduate research is rarely a solitary endeavor, especially for an experimentalist. I am blessed to have had many kind, intelligent, and considerate people in my life, both professionally and personally. It may be cliché, but it is no less true: Without the help and support of others, I could not have gotten this far.

I owe a great deal of gratitude to Kyle Shen, who hired me as his first student way back in the spring of 2007. Since then, he has taught me everything I know about ultra-high vacuum, photoelectron spectroscopy, and creating a world-class physics laboratory. Kyle has always been hands-on and down-to-earth, and I am grateful for his enthusiasm, approachability, and general "coolness." After all, how many professors will buy a flat screen TV, rock-climbing harness, or 3D printer for their lab?

I am indebted to all of the current and former members of the Shen group. Eric Monkman, Danny Shai, and Dawei Shen were there from the very beginning, and I still have vivid memories of traveling with them to Penn State. I remember living above Saint's Cafe during our first summer in State College, before wisely choosing to rent a house in the middle of a corn field but away from the noise of the city. Since those days, Yuefeng Nie, Bulat Burganov, Shouvik Chatterjee, Phil King, Masaki Uchida, Ed Lochocki, and Haofei Wei have joined the group and have made it a pleasure to work in the lab every day (and sometimes nights).

The close collaboration that was forged with Darrell Schlom's research group in the Penn State days has contributed tremendously to my research. I would be remiss if I did not acknowledge Darrell's guidance and the heroic efforts that Carolina Adamo and Gino Maritato sustained in order to grow thin films for me—Carolina for the $SrFeO_3/SrTiO_3$ and ruthenate projects at Penn State, and Gino for the cuprate project that makes up this dissertation. Gino, in particular, has taught me everything I know about growing cuprate films via molecular-beam epitaxy.

Within Clark Hall, I owe thanks to all of the hard-working people that have made research in the physics department possible: Eric Smith, who continues to tolerate our abuse of helium dewars; Leonard Freelove, who has delivered hundreds of packages to our office without misplacing a single one; Stan Carpenter and Rodney Bowman, who have had to put up with crazy construction and machining requests over the years; Linda Hatch, who has had to process more purchase orders than I would like to think about; and Nate Ellis, who introduced me to the joys of machining. I will always remember Nate's wit, humor, and outstanding teaching skills.

The life of a graduate student is sometimes inhumane, especially in a small town like Ithaca. I could not have lasted these seven years without the help (and commiseration) of my good friends: Brant, Charlie, Ben, Pablo, Nick, Emily, Antonio, and everyone else I have met while here. The conversations, meals, parties, and *heavy* drinking that we've shared have made all the difference. The Golden Girls theme song says it perfectly: "Thank you for being a friend."

Lastly, and most importantly, I would like to thank my family for all of the support they have given me throughout my life. My parents have always encouraged my love of learning. As a young child, I remember Dad teaching me about evaporation by leaving a shallow dish of salt water out overnight, and I remember Mom ordering hard-to-find educational books over the phone because I had checked them out from the library and wanted to own them. From the moment I was born, my sister has stood up for me. Amanda's friendship, wisdom, and unwavering support has been invaluable. I could not ask for a better family, and this dissertation is dedicated to them.

John W. Harter

March 2013

TABLE OF CONTENTS

LIST OF TABLES

LIST OF FIGURES

CHAPTER 1

INTRODUCTION

Condensed matter physics is the branch of modern science dedicated to studying the physical phenomena that arise when matter, at low temperatures and high densities, condenses to form solids, liquids, and gases. Of the four fundamental forces of nature, it is the electromagnetic force that dominates condensed matter systems and, along with gravitation, encompasses the whole of our everyday experiences. The attraction and repulsion of refrigerator magnets, the melting of ice cubes in a glass of water, the rigidity of steel bridges, and the flow of electrons in a semiconducting microchip are all examples of phenomena that emerge from condensed phases of matter interacting via the electromagnetic force. Indeed, a defining characteristic of a condensed matter system is the presence of *interactions* among different constituents of the system. The treatment of these interactions presents an immense intellectual difficulty often deemed "the many-body problem."

1.1 The many-body problem

When describing a real physical system, interactions among constituents are unavoidable. The planets of the solar system interact via their gravitational pull on each other, modifying their orbits in often profound ways. In liquids, the van der Waals attraction between nearby molecules gives rise to surface tension. In crystalline solids, where atoms are bonded together in a periodic array, the long-range Coulomb interaction of electrons and ions dominates. The difficulties associated with many-body problems arise from the fact that the presence of interactions often makes the behavior of a physical system impossible to predict analytically and extremely difficult to simulate numerically. The many-body problem is ubiquitous in physics and presents a serious challenge. To quote Richard D. Mattuck:

> "In eighteenth-century Newtonian mechanics, the three-body problem was insoluble. With the birth of general relativity around 1910 and quantum electrodynamics in 1930, the two- and one-body problems became insoluble. And within modern quantum field theory, the problem of zero bodies (vacuum) is insoluble. So, if we are after exact solutions, no bodies at all is already too many!" [1]

Fortunately, certain kinds of systems with sufficiently weak interactions are amenable to simple analyses. In particular, this dissertation deals with conducting metals, where a powerful idea called "Fermi liquid theory" allows interactions between mobile electrons to be treated in a simple, comprehensive, and consistent way. The concept of a Fermi liquid serves as a straightforward starting point for the investigation of stronger electronic interactions, which will be a major subject of this dissertation.

1.2 Fermi liquid theory

The concept of a Fermi liquid is primarily due to Lev Landau [2–4] in his attempt to explain why the noninteracting electronic band theory of Felix Bloch [5] seemed to work so well. A basic understanding of the theory can be obtained by considering what occurs when the interaction term in the Hamiltonian of an electronic system is slowly turned on. The starting wavefunction, consisting of independent one-electron levels (a Fermi gas), will no longer remain an eigenstate of the Hamiltonian: the individual energy levels will shift and electrons will start scattering between states. If the scattering rate is low, the system may be treated like an independent electron system, but with modified energy levels and a finite particle lifetime [6,7]. The key point is that if the interactions are sufficiently weak, the basic structure of the wavefunction will not change. This is illustrated in Fig-

ure 1.1, where the wavefunctions of the infinite square well and the quantum harmonic oscillator are compared. The Hamiltonians of the two systems are qualitatively similar, leading to approximately congruent wavefunctions. In the same way, the wavefunctions of a weakly interacting Fermi liquid will retain the same basic structure of a Fermi gas.

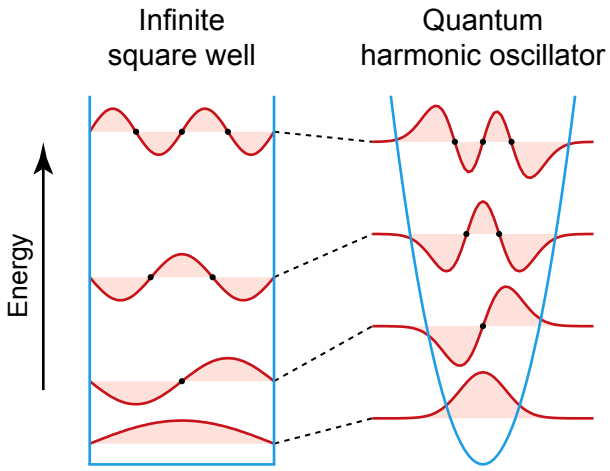

Figure 1.1: Illustration of the basic idea behind Fermi liquid theory. Changing the Hamiltonian from the infinite square well to the quantum harmonic oscillator does not alter the basic structure of the wavefunctions. For example, the number of wavefunction nodes is conserved.

It turns out that the Pauli exclusion principle significantly restricts the scattering rate of electrons near the Fermi energy in a metal [1,7]. In order for an electron with energy ϵ_1 to scatter, it must interact with another electron with energy ϵ_2 lying below the Fermi level (because at low temperatures those are the only occupied states). The exclusion principle forbids double occupancy of states and therefore demands that the electrons scatter into the unoccupied states ϵ_3 and ϵ_4 lying above the Fermi level. Energy conservation during the scattering process requires that

$$\epsilon_1 + \epsilon_2 = \epsilon_3 + \epsilon_4. \tag{1.1}$$

If ϵ_1 lies within an energy difference Δ with respect to the Fermi level, the other three energies are only allowed to vary within an energy shell of thickness Δ about the Fermi

surface. This restriction of phase space leads to a scattering rate of order Δ^2. This means that at zero temperature, an electron on the Fermi surface ($\Delta = 0$) will never scatter. At finite temperatures, $\Delta \sim k_B T$ and the lifetime τ of single-particle states will vary as

$$\frac{\hbar}{\tau} \sim (k_B T)^2 , \tag{1.2}$$

where $\hbar$ is Planck's constant, k_B is Boltzmann's constant, and T is the temperature of the system. Thus, in a metal the scattering rate near the Fermi surface can be made as small as one wishes by going to sufficiently low temperatures. This reduced scattering rate greatly expands the range of applicability of the Fermi liquid theory, provided that upon moving from a Fermi gas to a Fermi liquid the exclusion principle is retained among the fundamental excitations of the system.

1.2.1 Quasiparticles

We have described how the fundamental excitations of a Fermi liquid remain in one-to-one correspondence with the independent electron levels of a Fermi gas. Weak interactions simply "renormalize" the energies and lifetimes of the single-particle levels. These new states are called "quasiparticles" because they retain the same basic form of free electrons but can be imagined to carry a "cloud" of agitated neighbors as they move through the system. Figure 1.2 shows a cartoon comparing a Fermi gas of noninteracting particles to a Fermi liquid with interacting quasiparticles. In a Fermi liquid, quasiparticles are long-lived resonances of the many-body Hamiltonian that behave like single particles, but are not true eigenstates.

Fermi liquid theory and the quasiparticle concept form a basic starting point for understanding the many-body problem in strongly interacting electronic materials. Indeed, interpretations of experimental data on electron systems often use the language of quasi-

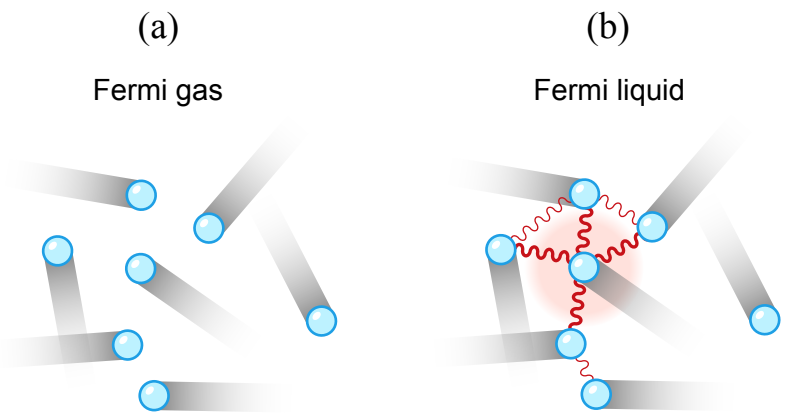

Figure 1.2: Cartoon of a quasiparticle. (a) In a Fermi gas, electrons do not interact with each other and behave independently. (b) In a Fermi liquid, interactions modify the properties of individual electrons, transforming them into so-called "quasiparticles" that have a renormalized dispersion and a finite lifetime.

particles: dispersion relations, self-energies, lifetimes, and scattering rates, for example. This dissertation investigates a particular class of transition metal oxides where strong interactions manifest themselves in interesting ways, and the quasiparticle concept serves as a framework for discussing the effects of such interactions.

1.3 Outline of the text

In this chapter, we have introduced the central framework supporting modern condensed matter physics of conducting electronic materials: Fermi liquid theory and its associated quasiparticles. The remainder of this dissertation is outlined as follows: Chapters 2 and 3 review the experimental techniques of angle-resolved photoemission spectroscopy and molecular-beam epitaxy, respectively. These techniques form the basic tools for the experimental work discussed later. Chapter 4 examines high-temperature superconductors, with special attention to their general electronic structure. Chapter 5 introduces the

infinite-layer cuprate material family, reviewing the current state of experimental understanding and enumerating known properties. Chapter 6 presents the electronic structure of infinite-layer $Sr_{0.90}La_{0.10}CuO_2$, where the coexistence of strong (π, π) antiferromagnetic order with presumably d-wave superconductivity is observed to have significant ramifications for the Fermi surface of the material. The results can explain many experimental inconsistencies related to the infinite-layer superconductors. In Chapter 7, the doping dependence of the electronic structure of $Sr_{1-x}La_xCuO_2$ is examined. At low doping, a lower Hubbard band characteristic of cuprate parent compounds is observed. As carriers are added to the system, the Mott gap gradually fills in. Chapter 8 describes an apparent surface reconstruction observed in $Sr_{1-x}La_xCuO_2$ thin films, which can be explained in terms of the polar nature of the infinite-layer structure. Finally, Chapter 9 offers concluding remarks, speculations, and future directions of research.

CHAPTER 2

ANGLE-RESOLVED PHOTOEMISSION SPECTROSCOPY

Angle-resolved photoemission spectroscopy, better known as ARPES, plays a unique and invaluable role in the field of condensed matter physics by offering a direct momentum-space probe of the underlying electronic structure of solids. Indeed, the band structure, Fermi surfaces, and energy gaps of countless materials have been measured with high precision by ARPES. Despite the complexities involved in implementing the technique, ARPES is based on a simple physical phenomenon first observed more than a century ago.

2.1 History

In 1887, Heinrich Hertz observed that the electromagnetic radiation emitted from an electrical arc could trigger nearby electrodes to spark [8]. It soon became apparent that electrons were emitted from a metal surface when exposed to ultraviolet light and these electrons were the cause of the sparking [9]. This experimental phenomenon was named the photoelectric effect.

2.1.1 The photoelectric effect

Figure 2.1(a) shows a schematic diagram of the apparatus used by early investigators to measure the photoelectric effect. The device consisted of an evacuated glass vessel containing three metal electrodes, the first of which was exposed to ultraviolet radiation via a window. By increasing the voltage V applied to a second electrode until the photocurrent I flowing between the first and third electrode dropped to zero, one could measure the

maximum kinetic energy, eV, of the photoemitted electrons. Investigators observed that although the measured photocurrent I was proportional to the incident light intensity, the stopping potential V was independent of it.

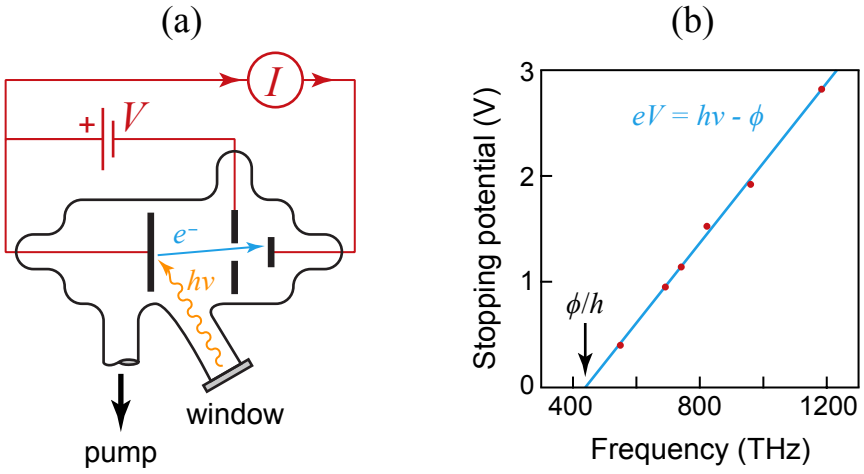

Figure 2.1: The photoelectric effect. (a) Schematic diagram of the early apparatus used by Hertz, Lenard, Millikan, and others to measure the photoelectric effect. (b) Millikan's measurements of photoemission from sodium [12]. The data obey Equation 2.1.

2.1.2 The Einstein equation

It was Albert Einstein who in 1905, while simultaneously working on special relativity and Brownian motion, solved the riddle of the photoelectric effect by considering the particle-like properties of light [10]. Prompted by Max Planck's analysis of blackbody radiation [11], Einstein assumed that light consisted of discrete particles called photons, each with energy $h\nu$, where h is Planck's constant and ν is the frequency of the light. A simple consideration of energy conservation then gives the equation

$$E_{max} = h\nu - \phi, \tag{2.1}$$

where E_{max} is the maximum electron kinetic energy measured and ϕ is the so-called work function of the material, which describes the energy necessary for an electron to break

free of the metal surface. The equation predicted a linear dependence of the stopping potential on frequency. Robert Millikan, in 1916 using monochromatic ultraviolet light sources, verified Einstein's prediction. Figure 2.1(b) shows the data obtained by Millikan on a sodium electrode [12]. Einstein's solution was a triumph for the newly emerging quantum theory.

2.1.3 History of ARPES

In the 1960s, researchers realized that the photoelectric effect could be used as a powerful probe of electronic structure. In 1964, the electronic density of states of copper and silver metal were measured in the seminal works of Berglund and Spicer [13, 14]. Their angle-integrated measurements agreed well with predictions from noninteracting band theory. In that same year, E. O. Kane proposed that the angular distribution of photoelectrons could yield information about the momentum-dependent band structure of a material [15]. However, it was not until 1974 that the first angle-dependent band mappings were performed [16, 17]. Technology progressed, and in 1981, Kai Siegbahn shared the Nobel prize in physics "for his contribution to the development of high-resolution electron spectroscopy."

The discovery of high-temperature superconductivity by J. G. Bednorz and K. A. Müller in 1986 [18] spurred the development of high-resolution ARPES. Before then, the typical energy resolution in an ARPES experiments was $\sim$100 meV. Advances in instrumentation in the 1990s and 2000s pushed the energy resolution down to $\sim$1 meV, with a similar improvement in angular resolution. In addition, the multichannel electron analyzers developed during that period significantly decreased the time required for measurements. While improvements were being made to electron spectrometers, photon

sources also progressed. For example, the development of laser-based low-energy light sources in the 2000s expanded the capabilities of ARPES and revealed new features in the electronic structure of superconducting cuprates. Today, hundreds of laboratories, synchrotron beamlines, and research groups around the world are working to further push the limits of ARPES.

2.2 Theory of photoemission

Photoemission is a quantum transition involving the absorption of a single photon's energy and spin by an electron, with a corresponding excitation of that electron. The process conserves energy, so that if an electron within a solid has binding energy E_B relative to the Fermi energy E_F, then the electron's kinetic energy after absorption of the photon and exit from the solid, E_{kin}, is given by

$$E_{kin} = h\nu - \phi - E_B, \tag{2.2}$$

where, as in the Einstein equation, $h\nu$ is the incident photon energy and ϕ is the work function of the system [19, 20]. Figure 2.2(a) shows how the energy distribution of electrons evolves in the photoemission process.

Because the solid's surface breaks translational symmetry only in the normal direction $\hat{\mathbf{c}}$, the electron's momentum is conserved in the two orthogonal directions $\hat{\mathbf{a}}$ and $\hat{\mathbf{b}}$. Momentum conservation gives

$$\mathbf{p} \cdot \hat{\mathbf{a}} = \sqrt{2mE_{kin}} \sin\theta \cos\varphi, \tag{2.3}$$

$$\mathbf{p} \cdot \hat{\mathbf{b}} = \sqrt{2mE_{kin}} \sin\theta \sin\varphi, \tag{2.4}$$

where $\mathbf{p}$ is the momentum of the electron within the solid *before* being photoemitted, m is the electron mass, and the angles θ and φ are defined in Figure 2.2(b). The photon's

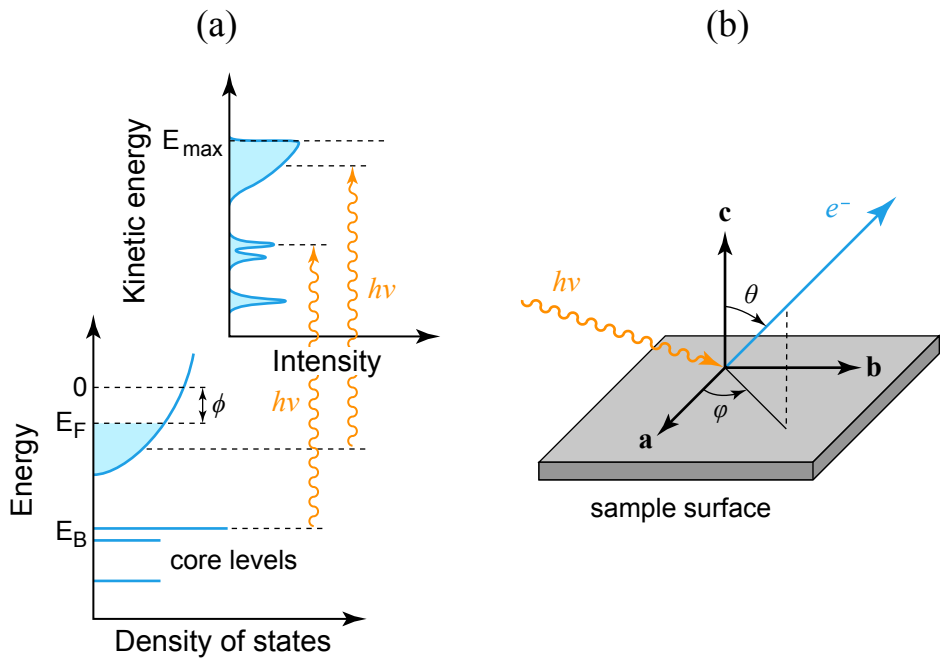

Figure 2.2: Diagram of photoemission. (a) Energy level diagram of the photoemission process showing the evolution of the electron energy distribution. (b) Definition of electron exit angles in a photoemission experiment.

momentum is ignored because it usually contributes a negligible amount to the total momentum of the process [20]. For example, a 21.2 eV photon (He-Iα) carries a momentum less than 0.7% of the length of a reciprocal lattice vector for a perovskite crystal.

2.2.1 The three-step model

Although in reality photoemission takes place as a single physical event, it is conceptually simpler to regard it as composed of three distinct consecutive processes. This ubiquitous simplification is called the "three-step model" [13, 19, 20].

In the first step, an electron within the solid absorbs a photon and is promoted via a so-called "direct" transition into an excited energy state with the same crystal momentum $\mathbf{k}$,

leaving behind a positively-charged hole. This final-state hole can have significant ramifications for the measured spectrum. In fact, ARPES directly measures the hole spectral function of the material under study. Because the electron absorbs not only the photon's energy but also its angular momentum, the process must obey optical selection rules. This results in a polarization dependence of the measured spectrum.

In the second step, the photoexcited electron travels to the sample surface and may scatter inelastically during its journey. Researchers have noticed that many different elemental metals fall on the same general mean free path versus kinetic energy curve. This so-called "universal curve" [19, 21] is displayed in Figure 2.3. For kinetic energies relevant to most ARPES experiments, the universal curve gives electronic scattering rates corresponding to mean free paths only a few atomic layers thick. As a result, photoemission requires atomically clean crystal surfaces and ultra-high vacuum systems in order to prevent unwanted adsorbates from condensing onto the sample. In addition, one must always consider to what extent the measured spectrum is representative of bulk rather than surface properties of the material under study.

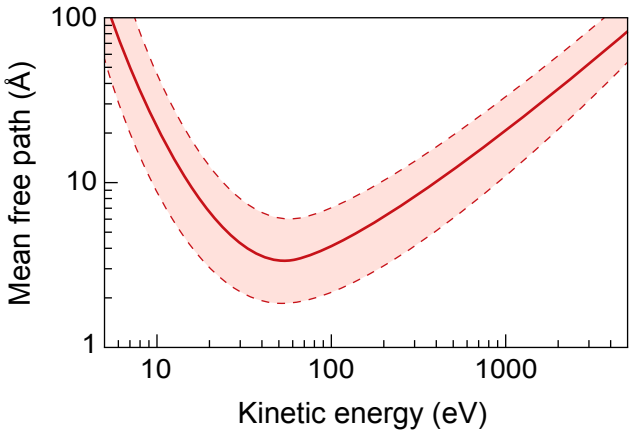

Figure 2.3: The fabled "universal curve" showing the generic dependence of electron mean free path on kinetic energy in elemental metals [19, 21].

In the third step, the electron breaks free of the solid and escapes into vacuum, possibly traveling into an electron analyzer to be detected in an ARPES experiment. At a microscopic level, this final step is not as simple as it seems. The electron must overcome the work function of the sample surface, losing energy as it travels through the surface dipole and charge distributions. Furthermore, the very presence of a crystal surface strongly modifies the electromagnetic field of the incident photons, but it is not clear how this affects the photoemission process.

2.2.2 Fermi's golden rule and the sudden approximation

The intensity measured in photoemission spectroscopy experiments is dominated by the first step in the three-step model. Assuming the electromagnetic field of the incident light adds only a small perturbation $\mathcal{H}'$ to the Hamiltonian of the electronic system, we may employ Fermi's golden rule to compute the electron photoexcitation rate [22]:

$$\omega_{i\to f} = \frac{2\pi}{\hbar} \left|\langle \Psi_f \left|\mathcal{H}'\right| \Psi_i\rangle\right|^2 \delta\left(E_f - E_i - h\nu\right), \tag{2.5}$$

where Ψ_i and Ψ_f are the initial and final wavefunction of the system and E_i and E_f are their corresponding energies. If we assume the many-body wavefunctions are Slater determinants of N single-particle orbitals, we can write

$$\Psi_i = \mathcal{A}\psi_i^{\mathbf{k}}\Psi_i^{N-1}, \tag{2.6}$$

$$\Psi_f = \mathcal{A}\psi_f^{\mathbf{k}}\Psi_f^{N-1}, \tag{2.7}$$

where $\mathcal{A}$ is the antisymmetrization operator, $\psi_i^{\mathbf{k}}$ and $\psi_f^{\mathbf{k}}$ are the initial and final orbitals of the photoelectron (with conserved crystal momentum $\mathbf{k}$ and implicit band index), and Ψ_i^{N-1} and Ψ_f^{N-1} are the initial and final wavefunctions of the $N-1$ remaining electrons in the system.

The main approximation used to interpret photoemission data is the ubiquitous "sudden approximation," in which the excited electron immediately leaves the solid without interacting with or altering the remaining $N-1$ electrons. This approximation is only valid in the high-energy limit, but appears to work sufficiently well for kinetic energies as low as 20 eV [23]. In this case, the wavefunction of the remaining electrons can be written

$$\Psi_i^{N-1} = \hat{c}_{\mathbf{k}} \Psi_0^N, \tag{2.8}$$

where Ψ_0^N is the ground state of the N-electron system and $\hat{c}_{\mathbf{k}}$ is the second quantization annihilation operator for the photoelectron. This state is not in general the ground state of the $(N-1)$-electron system, but can be written as a sum of its excited states:

$$\Psi_i^{N-1} = \sum_s c_s^{\mathbf{k}} \Psi_s^{N-1}, \tag{2.9}$$

where the index s enumerates the excited states and $c_s^{\mathbf{k}} = \langle \Psi_s^{N-1} | \Psi_i^{N-1} \rangle = \langle \Psi_s^{N-1} | \hat{c}_{\mathbf{k}} | \Psi_0^N \rangle$ are the coefficients of the sum.

Within minimal coupling [$\mathbf{p} \to \mathbf{p} + (e/c)\mathbf{A}$] and working in a gauge where the scalar potential vanishes, the perturbation of the electronic Hamiltonian by the electromagnetic field of the incident photons is given by

$$\mathcal{H}' = \frac{e}{2mc} (\mathbf{A} \cdot \mathbf{p} + \mathbf{p} \cdot \mathbf{A}) + \frac{e^2}{2mc^2} A^2, \tag{2.10}$$

where $\mathbf{A}$ is the electromagnetic vector potential. This expression can be greatly simplified. First, the intensity of light in ARPES experiments is always sufficiently low that two-photon processes can be ignored ($A^2 \to 0$). Second, the dipole approximation can be employed, where the vector potential is taken as approximately constant spatially. For example, a 21.2 eV photon (He-Iα) has a wavelength of 585 Å, more than two orders of magnitude larger than typical atomic distances in solids. This results in $\mathbf{p} \cdot \mathbf{A} \approx \mathbf{A} \cdot \mathbf{p}$, and the simplified perturbation becomes

$$\mathcal{H}' \approx \frac{e}{mc} \mathbf{A} \cdot \mathbf{p}, \tag{2.11}$$

which is proportional to $\hat{\mathbf{e}} \cdot \mathbf{p}$, where $\hat{\mathbf{e}}$ is the polarization vector of the light. It should be noted that it is not clear under what circumstances the dipole approximation may be rigorously applied because the dielectric response of the crystal surface strongly modifies the electromagnetic field of the incident light, drawing into question the assumptions of the approximation. Indeed, there is some evidence that the gradient of the vector potential cannot be neglected at low energies [19].

Combining all of the equations above, the total photoemission rate expected for electrons with momentum $\mathbf{k}$ can be written

$$\omega_{\mathbf{k}} = \sum_f \omega_{i \to f} = \frac{2\pi}{\hbar} \left(\frac{eA}{mc}\right)^2 |M_{\mathbf{k}}|^2 \sum_s \left|c_s^{\mathbf{k}}\right|^2 \delta\left(E_{kin} + E_s - E_0 - h\nu\right), \tag{2.12}$$

where $M_{\mathbf{k}} = \langle \psi_f^{\mathbf{k}} | \hat{\mathbf{e}} \cdot \mathbf{p} | \psi_i^{\mathbf{k}} \rangle$ is the so-called "matrix element" of the transition, E_{kin} is the kinetic energy of the photoelectron, and E_0 is the ground state energy of the original N-electron system. Photoemission only occurs when $E_0 + h\nu = E_{kin} + E_s$, ensuring conservation of energy.

2.2.3 The spectral function

One of the tasks of solid state physics is determining the band structure of materials. Specifically, knowledge about the quasiparticle energy dispersion $E(\mathbf{k})$ and lifetime $\tau(\mathbf{k})$ is desired. ARPES is a powerful experimental technique because it can provide *direct* access to this information via the spectral function.

The many-body Green's function propagator $G(\mathbf{k}, E)$, which describes how a material responds to a single-particle excitation, is defined by

$$G(\mathbf{k}, E) = \sum_s \frac{\left|\left\langle \Psi_s^{N-1} \left| \hat{c}_{\mathbf{k}} \right| \Psi_0^N \right\rangle\right|^2}{E - (E_s - E_0) - i\eta}, \tag{2.13}$$

where η is an infinitesimal bookkeeping variable and this definition is for hole-like excitations in which an electron is removed from the system [1]. The Green's function has poles whenever the energy E matches an excitation energy of the system. The spectral function $A(\mathbf{k}, E)$ is formally defined as the imaginary part of the Green's function:

$$A(\mathbf{k}, E) = \frac{1}{\pi}\mathrm{Im}\left[G(\mathbf{k}, E)\right], \tag{2.14}$$

Applying the identity

$$\frac{1}{z - i\eta} = \mathcal{P}\frac{1}{z} + i\pi\delta(z), \tag{2.15}$$

where $\mathcal{P}$ denotes the Cauchy principal value, to Equation 2.13 and using Equation 2.14, one immediately finds

$$A(\mathbf{k}, E) = \sum_s \left|\left\langle \Psi_s^{N-1} \left|\hat{c}_\mathbf{k}\right| \Psi_0^N \right\rangle\right|^2 \delta\left(E - (E_s - E_0)\right). \tag{2.16}$$

$A(\mathbf{k}, E)$ is essentially a probability density function describing the likelihood or "spectral weight" of finding a particle with a given crystal momentum $\mathbf{k}$ at the excitation energy E. As such, it obeys the rules of probability densities:

$$A(\mathbf{k}, E) \geq 0, \tag{2.17}$$

$$\int_{-\infty}^{\infty} A(\mathbf{k}, E)dE = 1. \tag{2.18}$$

Using the Lehmann representation, the Green's function can be expressed as an integral of $A(\mathbf{k}, E)$ over all energies,

$$G(\mathbf{k}, E) = \int_{-\infty}^{\infty} \frac{A(\mathbf{k}, E')}{E - E' - i\eta}dE', \tag{2.19}$$

so the spectral function encodes all possible information about single-quasiparticle dynamics.

By comparing Equation 2.16 to Equation 2.12, one sees that the photoemission rate measured by ARPES is directly proportional to the spectral function:

$$\omega_\mathbf{k} = \frac{2\pi}{\hbar}\left(\frac{eA}{mc}\right)^2 |M_\mathbf{k}|^2 f(h\nu - E_{kin})A(\mathbf{k}, h\nu - E_{kin}), \tag{2.20}$$

where the Fermi-Dirac distribution $f(E)$ has been added explicitly to account for measurements at finite temperature. ARPES provides access to the spectral function of a material, and because theorists are often able to compute Green's functions for model Hamiltonians, this allows for direct experimental tests of calculations and theories.

Utilizing Dyson's equation, the Green's function can also be written

$$G(\mathbf{k}, E) = \frac{1}{E - \epsilon(\mathbf{k}) - \Sigma(\mathbf{k}, E)}, \tag{2.21}$$

where $\Sigma(\mathbf{k}, E)$ is the so-called self-energy of the quasiparticle, which encodes modifications of the bare (noninteracting) dispersion $\epsilon(\mathbf{k})$ and lifetime of the quasiparticle due to interactions with other electrons. Substituting this expression into Equation 2.14, we get

$$A(\mathbf{k}, E) = \frac{\mathrm{Im}\left[\Sigma(\mathbf{k}, E)\right]/\pi}{\left(E - \epsilon(\mathbf{k}) - \mathrm{Re}\left[\Sigma(\mathbf{k}, E)\right]\right)^2 + \mathrm{Im}\left[\Sigma(\mathbf{k}, E)\right]^2}. \tag{2.22}$$

In a noninteracting system, single-particle excitations are eigenstates of the Hamiltonian. Therefore, $\tau(\mathbf{k}) \to \infty$ and $A(\mathbf{k}, E)$ consists of Dirac δ-functions at $E(\mathbf{k}) = \epsilon(\mathbf{k})$. For sufficiently weak interactions in which the quasiparticle concept can be applied, the spectral function is simply a normalized Lorentzian centered at $E(\mathbf{k}) = \epsilon(\mathbf{k}) + \mathrm{Re}\left[\Sigma(\mathbf{k}, E)\right]$ and with width $\hbar/\tau(\mathbf{k}) = \mathrm{Im}\left[\Sigma(\mathbf{k}, E)\right]$.

For stronger interactions, the spectral function can be artificially separated into a "coherent" part which takes the shape of a Lorentzian with total weight $Z < 1$ (the quasiparticle residue), and a broad "incoherent" background with total weight $1 - Z$. Figure 2.4 sketches the spectral function observed by ARPES in the case of a material with no interactions (a Fermi gas) and weak interactions (a Fermi liquid) and discusses a model for the origin of the incoherent part of $A(\mathbf{k}, E)$.

As discussed in the introduction, the Fermi liquid concept relies on the existence of quasiparticles with sufficiently long lifetimes. This requirement holds only near the Fermi surface of a metal and at low temperatures. In fact, with the same phase space arguments

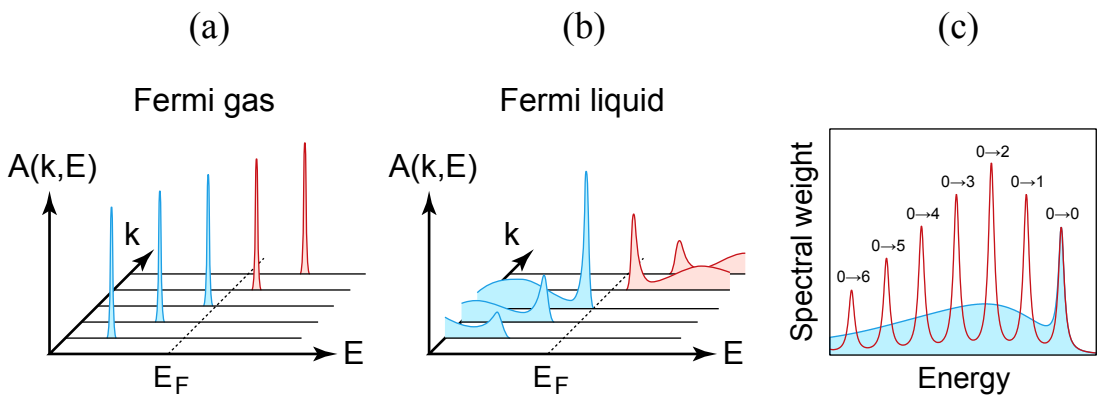

Figure 2.4: The spectral function $A(\mathbf{k}, E)$. (a) In a noninteracting Fermi gas, the spectral function is made up of Dirac δ-functions that track the noninteracting bandstructure of the solid. (b) When interactions are turned on, the spectral function broadens in energy and a tail of incoherent spectral weight develops. (c) The tail of spectral weight comes from transitions in which the ground state of the N-electron system has a transition into the manifold $\{s\}$ of excited states of the $(N-1)$-electron system (denoted by $0 \to s$). The quasiparticle peak occurs when s is the long-lived ground state of the $(N-1)$-electron system ($0 \to 0$). Other transitions ($s > 0$) have shorter lifetimes and are broadened into a "hump"-like structure.

used to derive Equation 1.2, the inverse quasiparticle lifetime can be shown to depend quadratically on distance from the Fermi level [1,7]:

$$\frac{\hbar}{\tau(\mathbf{k})} \sim \left[E(\mathbf{k}) - E_F\right]^2 . \tag{2.23}$$

Thus, far away from E_F lifetimes are short and quasiparticles do not exist.

2.3 Experimental aspects

The previous section showed that ARPES can provide valuable information about the electronic structure of solids because the measured photoemission intensity is proportional to the spectral function of the material under study. There are a number of experimental complications that must be considered when performing ARPES.

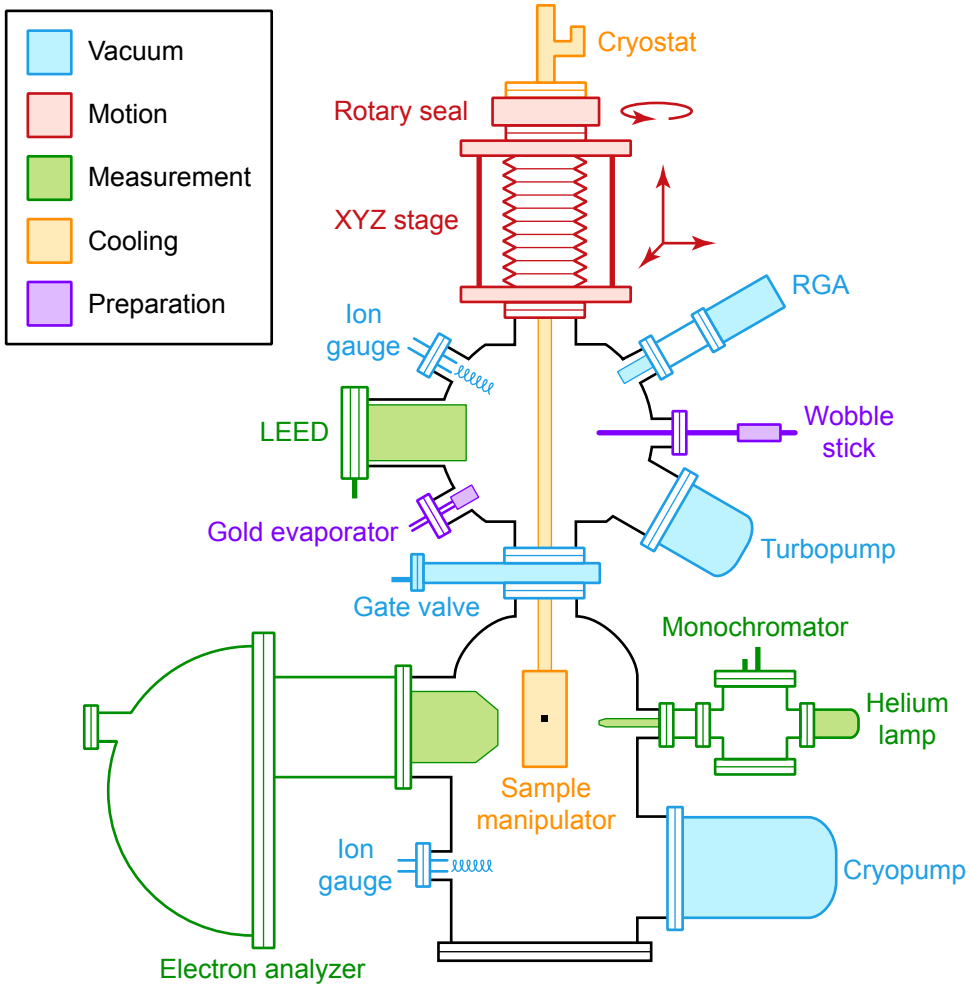

Figure 2.5: Schematic diagram of a typical ARPES system comprised of an upper preparation and lower measurement chamber. The parts of the system are colored based on their function: vacuum pumps and gauges (blue), sample motion (red), measurement apparatus (green), sample cooling (orange), and preparation (purple).

Figure 2.5 shows a typical ARPES system consisting of an upper and lower vacuum chamber separated by a gate valve. The upper chamber possesses a number of tools necessary to prepare the sample for measurement, including a wobble stick, a gold evaporator, and a port allowing transfer of the sample into the sample manipulator (not shown). The upper chamber also contains a low-energy electron diffractometer, used to characterize the surface quality and structure of samples. The lower chamber contains the equip-

ment necessary to perform ARPES: a photon source and an electron analyzer. Both upper and lower chambers contain pumps and gauges needed to maintain an ultra-high vacuum (UHV) within the system. The sample manipulator, which holds and rotates the sample, is mounted to the bottom of a cryostat and enters at the top of the upper chamber. It is lowered by the XYZ stage into the lower chamber during ARPES measurements.

2.3.1 Maintaining vacuum

As discussed in the previous section, ARPES probes the top few atomic layers of a crystal. Therefore, the measured photoemission intensity is extremely sensitive to unwanted adsorbates that may condense on the surface of the sample. As a result, ARPES must be performed under UHV conditions on cleaved or freshly grown samples. This restriction requires that the ARPES system be equipped with a number of pumps and vacuum gauges.

To estimate the level of vacuum necessary for photoemission, one can compute the time necessary for a single monolayer of adsorbate to form on the surface of a sample as a function of the background chamber pressure. This will give an estimate on the length of time that a given sample can be measured at that pressure. From the kinetic theory of gases, the number of gas molecules impinging on a surface of unit area per unit time is given by

$$\frac{\delta N}{\delta A \delta t} = \frac{P}{\sqrt{2\pi M R T}}, \tag{2.24}$$

where P is the pressure of the gas, M is the molecular weight of the gas, R is the molar gas constant, and T is the temperature [24]. Let us first conservatively assume that all molecules that collide with the sample stick to its surface. Then for a typical crystal at room temperature ($\sim$300 K) with lattice constant $\sim$4 Å within a gas with an average

molecular weight of ∼30 g/mol, the time for one monolayer of gas to be adsorbed is

$$\delta t \approx \frac{1.7 \times 10^{-6}\ \text{s·Torr}}{P}. \tag{2.25}$$

Thus, the estimated pressure required is less than 5×10^{-10} Torr for a one-hour measurement and less than 2×10^{-11} Torr for a one-day measurement. Fortunately, for most materials studied by ARPES, the sticking fraction is much less than one and higher pressures can be tolerated. Typical ARPES systems maintain base pressures in the range 10^{-10} to 10^{-11} Torr. At these pressures, most samples can be measured for many days. It is interesting to note that at a pressure of 10^{-11} Torr, there are only ∼300 gas molecules in every cubic millimeter of volume.

The pumps used in most ARPES systems are commercial turbomolecular pumps, cryopumps, ion pumps, and sublimation pumps. These "dry pumps" do not use oil and therefore ensure the ARPES system remains free of contaminants. In turbomolecular pumps, a rapidly spinning turbine imparts momentum to gas molecules, forcing them out of the UHV system and into a backing pump (usually a dry scroll pump or a diaphragm pump) to be exhausted. Cryopumps, ion pumps, and sublimation pumps act to capture and sequester gas molecules. They must be regenerated periodically.

The most common pressure gauges used for UHV are Bayard-Alpert ionization gauges, in which a heated filament emits electrons that are accelerated by an applied grid voltage. The electrons collide with gas molecules and ionize them. The gas ions are attracted to a central electrode and their current is amplified and converted into a pressure reading. Another useful gauge for UHV systems is the residual gas analyzer (RGA). An RGA is a mass spectrometer that can give information about the composition of residual gases in a UHV system. As such, it is extremely useful when searching for leaks in a vacuum chamber and for detecting contaminated materials.

2.3.2 The sample manipulator

Unlike vacuum pumps and gauges, which are widely available commercially, the sample manipulator in an ARPES system is a custom-made apparatus designed to meet certain performance specifications. Figure 2.6 shows the Mk-II manipulator designed and constructed by the author in 2010. The job of a sample manipulator is threefold: it must hold the sample in place and move it to various positions within the vacuum chambers, it must be able to rotate the sample so that wider momentum regions can be accessed during ARPES measurements, and it must cool the sample to low temperatures.

The sample manipulator is mounted at the bottom of a cryostat, which is attached to a rotary flange sitting on top of an XYZ stage. The XYZ stage allows for translation of the sample manipulator within the vacuum chamber, and the rotary flange allows for one degree of rotation of the sample—rotation of the azimuthal angle θ. The other two possible rotational degrees of freedom are actuated by rotating the sample within the sample manipulator head. For example, the copper "rotation arm" visible on the far right of Figure 2.6 is used to change the polar angle ϕ of the sample while keeping its position fixed in space. It is crucial that an ARPES manipulator be able to access a wide angular range because this allows for measuring large momenta. Figure 2.7 shows some examples of momentum regions accessible using He-Iα photons for various angular capabilities of the sample manipulator.

The sample manipulator is responsible for cooling the sample to low temperatures (often below 10 K). This requirement severely constrains its design. In ARPES, low temperatures are desired because the presence of phonons results in elevated electron scattering rates, greatly reducing the lifetime of quasiparticles. In addition, broadening of the Fermi-Dirac distribution function suppresses peaks in the spectral function near E_F. The main heat load on the sample manipulator (and the sample itself) is blackbody radiation

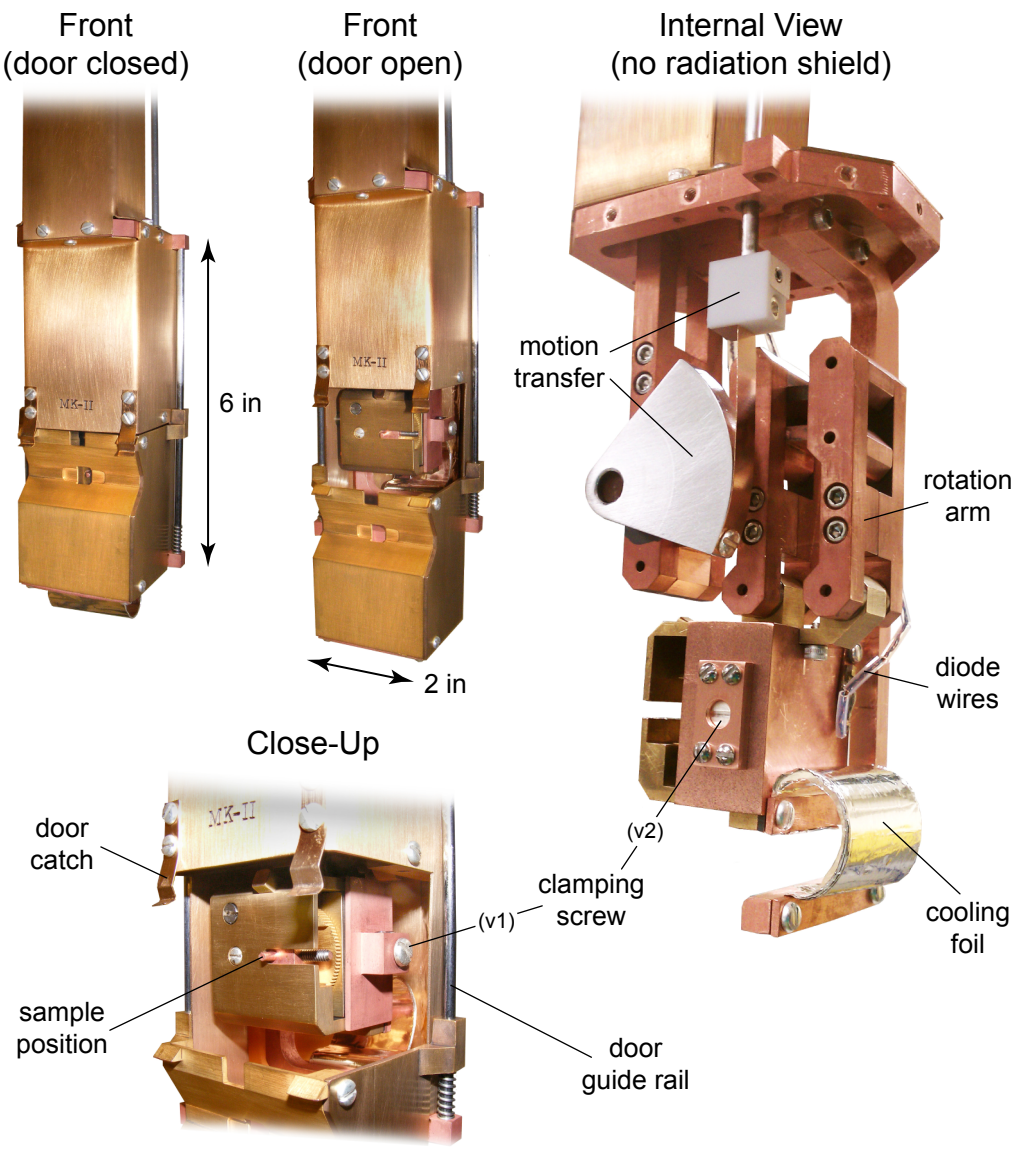

Figure 2.6: Photographs of the Mk-II sample manipulator designed and constructed by the author in 2010. Front views show the radiation shield door closed and open. Internal and close-up views show the manipulator mechanism. Selected parts are labeled.

from the surrounding vacuum chamber, which is usually at room temperature. For this reason, low-temperature sample manipulators contain outer radiation shields that block the internal mechanism from blackbody radiation. The Mk-II manipulator has a radiation shield with exposed area $A \sim 600$ cm^2. It is electroplated with gold in order to reduce the emissivity to $\epsilon \sim 0.1$. With these parameters, the Stefan-Boltzmann law can be used to

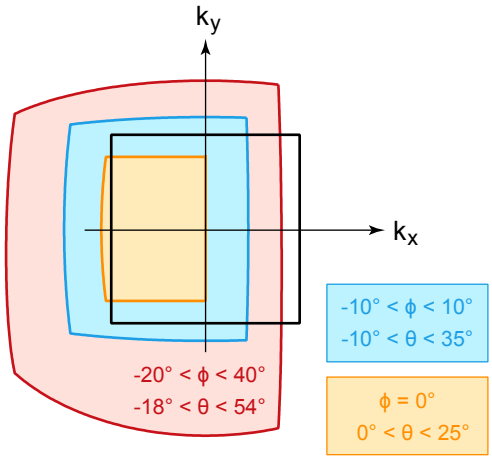

Figure 2.7: Examples of regions in momentum space accessible by ARPES using He-Iα photons ($E_{kin} \sim 17$ eV) for various angular capabilities of the sample manipulator. The third rotational degree of freedom, rotation around the sample normal, is assumed fixed. The black box shows the first Brillouin zone for a typical perovskite crystal with lattice constant 3.9 Å. The red region is the design range for the Mk-II manipulator.

compute the total heat load on the manipulator's radiation shield:

$$P = A\epsilon\sigma T^4 \approx 2.8\,\mathrm{W}, \tag{2.26}$$

where $\sigma = 5.67 \times 10^{-8}$ W/m^2·K^4 is the Stefan-Boltzmann constant. In a typical open-flow cryostat cooled with helium, this heat is carried away via the helium vapor exhausted from the cold head. The cold head itself, which cools the internal mechanism of the manipulator (and therefore the sample), is cooled via vaporization of liquid helium. Therefore the base temperature of the cryostat under no heat load is 4.2 K at atmospheric pressure and 1.8 K if the exhaust is pumped. The Mk-II manipulator can reach a base temperature of 6.9 K at the location of the sample.

One other important feature of an ARPES sample manipulator is a cold location where polycrystalline gold can be periodically evaporated. This is useful when determining the absolute Fermi level E_F, temperature, and instrumental broadening. Because the sample and gold are in electrostatic contact, their Fermi levels will be identical. During an ARPES

measurement, fresh polycrystalline gold presents a clean, dispersionless spectral function from which the Fermi energy, temperature, and instrumental broadening can be extracted much more easily than from the sample itself, which may exhibit quasiparticle peaks or a gapped Fermi surface.

2.3.3 The photon source

A key component of photoemission is the photon source, which is often a synchrotron because the light must be simultaneously bright and possess a narrow spectral bandwidth (in order to maintain a high energy resolution). A common alternative to synchrotrons is the commercial laboratory-based noble gas plasma lamp, of which helium is by far the most common, with spectral bandwidths on the order of $\sim$1 meV. In these devices, a waveguide is used to direct the output of a microwave generator into a small cavity filled with a noble gas at low pressure. The microwaves sustain a plasma of the gas, which emits photons at characteristic frequencies associated with atomic transitions.

Table 2.1: Atomic lines emitted by a helium plasma

Line	**Atomic Transition**	**Energy (eV)**	**Intensity (%)**
He-Iα	2p ^{1}P $\rightarrow$ 1s^2 ^{1}S	21.2	88
He-Iβ	3p ^{1}P $\rightarrow$ 1s^2 ^{1}S	23.1	5
He-Iγ	4p ^{1}P $\rightarrow$ 1s^2 ^{1}S	23.7	1
He-Iδ	5p ^{1}P $\rightarrow$ 1s^2 ^{1}S	24.0	0.2
He-IIα	2p ^{2}P $\rightarrow$ 1s ^{2}S	40.8	5
He-IIβ	3p ^{2}P $\rightarrow$ 1s ^{2}S	48.4	0.5
He-IIγ	4p ^{2}P $\rightarrow$ 1s ^{2}S	51.0	0.1

A major drawback of plasma lamps is the fact that the photon energy is fixed at a discrete set of atomic lines. For a helium lamp, this mainly encompasses the He-Iα line at 21.2 eV and the He-IIα line at 40.8 eV. Table 2.1 enumerates the complete set of atomic lines for a helium lamp. Often a toroidal grating monochromator and glass capillary is used in

conjunction with a plasma lamp in order to separate the discrete atomic lines and focus the plasma radiation onto the sample. A series of differentially pumped stages are required so that the plasma, operating at relatively high pressures, has a direct line-of-sight to the sample without spoiling the main chamber pressure. Even with these additions, the chamber pressure during measurement often increases by a few 10^{-11} Torr.

The spectral lines from plasma lamps, as well as typical photon energies used at synchrotrons, sit close to the minimum of the universal curve shown in Figure. 2.3. Some benefits of using low-energy light sources therefore include an enhanced sensitivity to more bulk-like properties of the system under study, an increased tolerance to unwanted adsorbates on the sample surface, and a higher momentum resolution. As a result, the development and use of low-energy sources have recently become common in the ARPES community. These are typically laser based: one such source supplies 7 eV photons by using the nonlinear optical crystal $KBe_2BO_3F_2$ to generate the second harmonic of a frequency-tripled Nd:YVO_4 laser [25], and a similar 6 eV light source based on the crystal β-BaB_2O_4 generates the fourth harmonic of a titanium-sapphire laser [26]. Another low-energy photon source in use employs a low-pressure xenon discharge lamp, which has a number of discrete atomic lines spanning the energy range 8 to 11 eV [27,28].

One major disadvantage of the laser sources described above is a fixed photon energy, which is a particularly important issue at low energies because of the sensitivity to photon wavelength caused by final-state matrix element effects. The ability to tune the photon energy, however, can mitigate this issue. The author has therefore developed a new low-energy photon source for ARPES consisting of a laser-driven xenon plasma lamp coupled to a Czerny-Turner monochromator [29]. Figure 2.8 shows a schematic diagram of the photon source. Under typical operation, the device delivers $>10^{12}$ ph/s at a 10 meV spectral bandwidth. The brightness, energy tunability, and adjustable spectral bandwidth

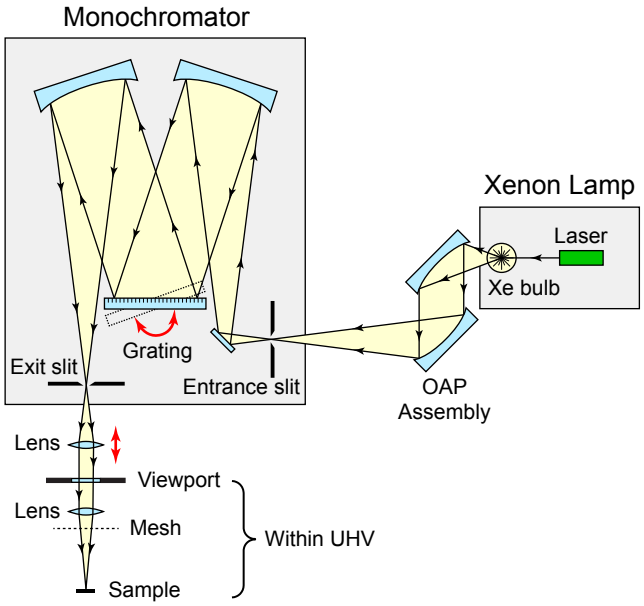

Figure 2.8: Schematic diagram of the low-energy photon source developed by the author. Within the xenon lamp housing, an internal laser excites a plasma contained inside the xenon bulb. The light emitted from the plasma is focused onto the entrance slit of the monochromator with a pair of off-axis parabolic (OAP) mirrors. At the exit slit of the monochromator, a pair of lenses focuses the light through an ultra-high vacuum viewport and onto the sample.

of the light source make it ideally suited for laboratory-based high-resolution ARPES experiments.

2.3.4 The electron analyzer

Perhaps the most crucial instrument in an ARPES system is the electron spectrometer, which detects the energies and exit angles of electrons photoemitted from a sample. The most common electron analyzer design is the spherical deflection analyzer, shown schematically in Figure 2.9. In this design, incident electrons are retarded by an electrostatic lens to a fixed "pass energy." The electrons then pass through an entrance slit and

enter a region between two concentric hemispheres held at a fixed voltage difference. The electrostatic field between the hemispheres bends the path of the electrons, producing a trajectory with an E_{kin}-dependent radius. Finally, the electrons collide with a microchannel plate (MCP), which accelerates and amplifies the electron charge and causes an adjacent phosphor screen to fluoresce. A video camera records the phosphor screen, where electrons disperse in energy along one spatial direction and angle along the perpendicular direction. This angle multiplexing feature has revolutionized the field of ARPES by significantly reducing the time needed to collect data.

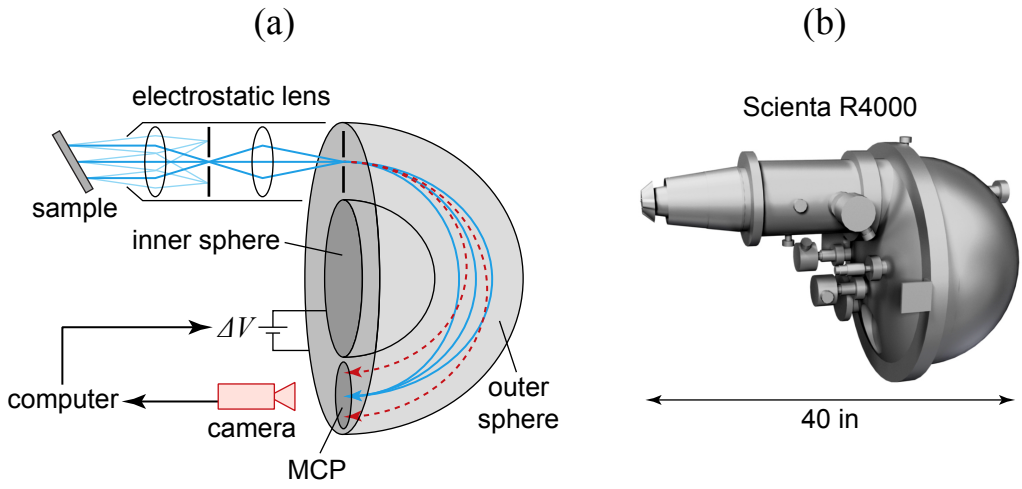

Figure 2.9: The electron analyzer. (a) Schematic diagram of a spherical deflection electron analyzer. Electrons with energies matching the pass energy of the analyzer are shown by solid blue lines and electrons with energies slightly greater and less than the pass energy are shown by dashed red lines. (b) Computer rendering of the Scienta R4000 electron spectrometer.

The energy resolving power of an electron analyzer depends on the hemisphere radius, the pass energy, the entrance slit width, and the resolution of the MCP. A fixed pass energy is used in order to keep the energy resolution of the analyzer constant for a given energy scan. The most common advanced electron analyzer on the market is the VG Scienta R4000, which has a resolving power of up to 4000 and an angular detection range of up to $\pm 15^{\circ}$. Table 2.2 shows the energy range covered by the MCP (in fixed mode) and

the energy resolution (using a 0.2 mm entrance slit width) of the R4000 spectrometer for the set of pass energies used in ARPES experiments.

Table 2.2: R4000 analyzer pass energies

PE (eV)	Energy Window (eV)	Resolution (meV)
1	0.08	2.9
2	0.17	3.5
5	0.42	4.9
10	0.84	7.2
20	1.68	12.2

Magnetic shielding

ARPES is extremely sensitive to magnetic fields. As an example, consider a photoelectron with $E_{kin} = 20$ eV moving perpendicularly to the earth's magnetic field. After traveling a distance of only 1 cm away from the sample, the electron will experience a deflection of 2°, distorting and possibly destroying the angular information collected in an experiment. To avoid this, both the electron analyzer and the lower chamber must be shielded from the earth's field and from any stray magnetic fields near the ARPES system. The most common material used for magnetic shielding is mu-metal, which is a nickel-iron-copper alloy with a relative magnetic permeability of up to 10^5. Magnetic shielding works by creating a low reluctance path so that magnetic field lines can flow around the vacuum chamber rather than through it. The shielding often takes the form of an internal shell near the inside wall of the measurement chamber. This shell can consist of two layers of mu-metal separated by a gap in order to further reduce the magnetic field. In some cases the chamber itself is made of mu-metal.

Patch fields

Different materials have different work functions. For example, the work function of cesium metal is 1.8 eV while that of tungsten is 4.5 eV [7]. In addition, the work function of a material depends on whether the surface is planar or rough and on the orientation of the surface with respect to the crystal lattice; even the same material may have a variable work function depending upon how it is prepared. Because of this, electric "patch" fields will form near surfaces with different work functions, with field lines flowing from one surface to another. In order to minimize these fields, which may interfere with photoelectrons, the internal components of electron analyzers and the mu-metal shielding are coated in a thin layer of polycrystalline graphite. This results in a uniform work function for all materials near the photoelectrons, minimizing the effects of patch fields.

2.4 Analysis of data

The basic methods for the analysis of ARPES data are well established. These include transformations from angle and kinetic energy into momentum and binding energy, respectively, as well as the extraction of physically relevant parameters from the measured spectral function—for example, the quasiparticle dispersion and lifetime.

2.4.1 Transformation from angle to momentum

We have seen that modern electron analyzers can, with great precision, directly detect the exit angle of an electron as it is photoemitted from the surface of a sample. In order to convert this information into a physically meaningful quantity—the in-plane momentum of

the electron—a series of non-commuting rotations must be applied to the sample surface basis vectors $\hat{\mathbf{a}}$ and $\hat{\mathbf{b}}$. These transformations take into account the sample manipulator azimuthal (θ) and polar (ϕ) angles, as well as rotation about the surface normal (ω), which depends on both the manipulator and the sample mounting orientation.

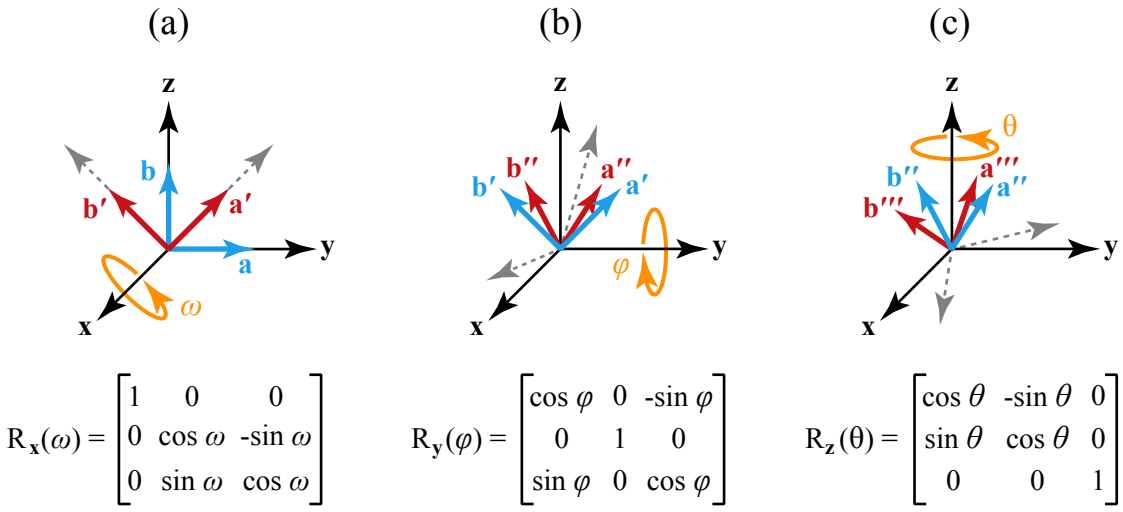

Figure 2.10: Series of rotations and corresponding matrices applied to the sample surface basis vectors $\hat{\mathbf{a}}$ and $\hat{\mathbf{b}}$. (a) Rotation about the sample normal. This degree of freedom can be controlled by both the manipulator and the sample mounting orientation (b) Rotation of the sample manipulator polar angle. (c) Rotation of the sample manipulator azimuthal angle.

Figure 2.10 shows diagrams and corresponding matrices for the three required rotational transformations. Axes are drawn assuming that the analyzer lens is pointing at the sample along $-\hat{\mathbf{x}}$, with the analyzer entrance slit oriented along the $\pm\hat{\mathbf{z}}$ direction. An electron with measured exit angle ξ will then have the normalized momentum vector

$$\hat{\mathbf{p}} = [\cos\xi \quad 0 \quad \sin\xi]^T, \tag{2.27}$$

where T denotes transposition of the row vector into a column vector. We wish to decompose this vector into components along the fully rotated sample basis vectors $\hat{\mathbf{a}}'''$ and $\hat{\mathbf{b}}'''$, which represent the physically meaningful intrinsic lattice vectors of the crystal under

study after rotation by the sample manipulator:

$$\hat{\mathbf{a}}''' = R_{\mathbf{z}}(\theta)R_{\mathbf{y}}(\phi)R_{\mathbf{x}}(\omega)\,[0 \quad 1 \quad 0]^T\,, \tag{2.28}$$

$$\hat{\mathbf{b}}''' = R_{\mathbf{z}}(\theta)R_{\mathbf{y}}(\phi)R_{\mathbf{x}}(\omega)\,[0 \quad 0 \quad 1]^T\,. \tag{2.29}$$

This is done with a simple dot product. Carrying through the matrix and vector products and simplifying, one obtains:

$$\hat{\mathbf{p}} \cdot \hat{\mathbf{a}}''' = [\sin\omega(\cos\phi\sin\xi - \cos\theta\sin\phi\cos\xi) - \cos\omega\sin\theta\cos\xi]\,, \tag{2.30}$$

$$\hat{\mathbf{p}} \cdot \hat{\mathbf{b}}''' = [\cos\omega(\cos\phi\sin\xi - \cos\theta\sin\phi\cos\xi) + \sin\omega\sin\theta\cos\xi]\,. \tag{2.31}$$

These formulae allow for a straightforward transformation from angle into momentum, provided the momentum components are scaled by a factor of $\sqrt{2mE_{kin}}$, where E_{kin} is the measured kinetic energy of the electron.

2.4.2 Energy referencing

As discussed in Section 2.3.2, polycrystalline gold is periodically measured during an ARPES experiment. By measuring the Fermi edge of the gold, which is in electrostatic contact with the sample and presents a clean, dispersionless spectral function, one can determine the absolute Fermi energy, temperature, and instrumental broadening. To do this, the spectral function is assumed to take the functional form of a resolution-broadened Fermi step with an underlying linear density of states:

$$F(E) = \frac{a + b(E - E_F)}{e^{(E-E_F)/k_BT} + 1} \otimes \frac{e^{-E^2/2\sigma^2}}{\sqrt{2\pi}\sigma} + c, \tag{2.32}$$

where $\otimes$ signifies convolution and σ is the standard deviation of the instrumental broadening. The set of variational parameters $\{a, b, c, E_F, T, \sigma\}$ are adjusted until a good match to the momentum-averaged spectrum of the gold is found. Often the temperature is

known to good precision in an experiment and is therefore held constant in the least-squares fitting routine. Figure 2.11 shows an example of the results of this procedure.

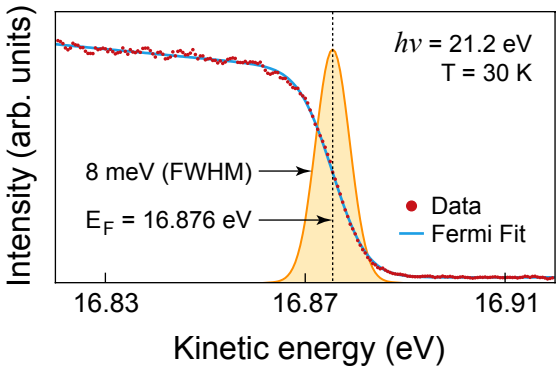

Figure 2.11: The Fermi level is determined by fitting a momentum-averaged energy distribution curve for polycrystalline gold to the Fermi-Dirac distribution function. The orange curve shows the instrumental broadening function determined by the fit.

2.4.3 Display of data

ARPES experiments yield large amounts of data. Typically, individual energy spectra are collected at thousands of points in momentum space. This data may be displayed in a number of ways. The four most common arrangements are Fermi surface maps and momentum space cuts, which are two-dimensional, and energy distribution curves (EDCs) and momentum distribution curves (MDCs), which are one-dimensional. Figure 2.12 shows a schematic diagram of a momentum space cut and Fermi surface map for a two-dimensional free electron gas and Figure 2.13 shows examples of these four methods for a relatively simple electron-like pocket on the surface of CdO [29]. In this material, the electronic structure is well-approximated by a free electron gas:

$$E(k_x, k_y) = \frac{1}{2m^*}\left(k_x^2 + k_y^2\right), \tag{2.33}$$

where m^* is the effective mass of the electrons. The circular Fermi surface and parabolic band dispersion are clearly visible in the image plots and compare well to the expectations in Figure 2.12. Such simple models work best for two-dimensional materials. The introduction of a third dimension in which the energy bands can disperse often makes ARPES data, and in particular Fermi surface maps, more difficult to interpret.

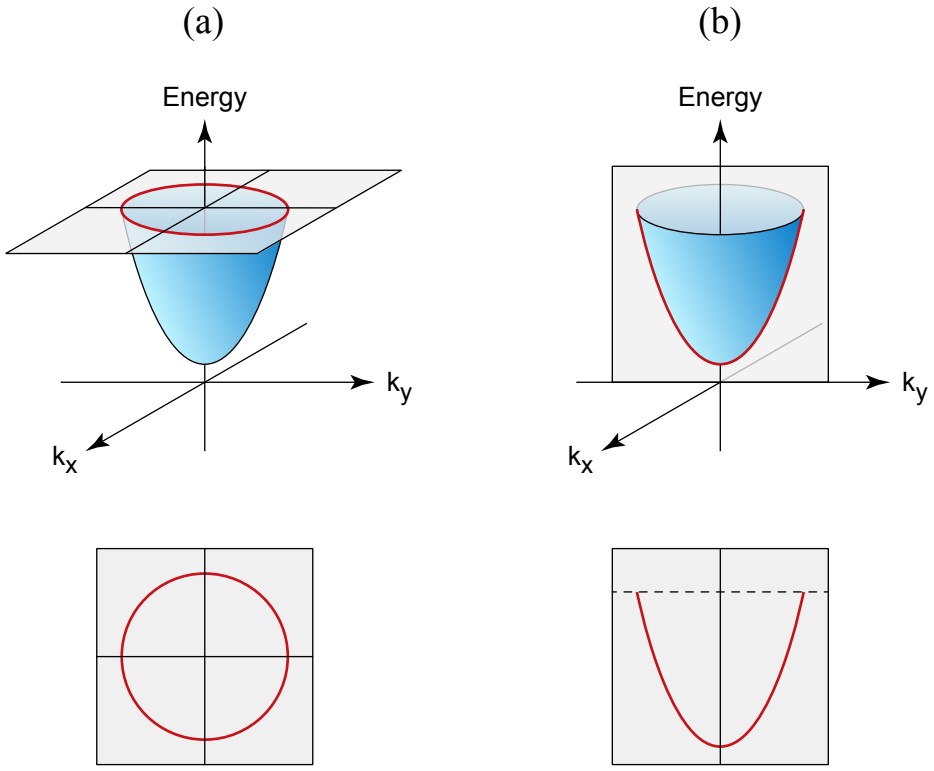

Figure 2.12: Two-dimensional cuts through ARPES data for a free electron gas in two dimensions. (a) A Fermi surface map shows the spectral weight of electrons in momentum space at the Fermi energy—the Fermi surface. (b) A dispersion image shows the energy of electrons as a function of momentum in a fixed direction.

By fitting the peak positions in EDCs and MDCs, one can track the band dispersion of a quasiparticle. This yields information about the real part of the self energy (by comparison to calculations based on density functional theory or tight binding models) as well as coupling to bosonic modes (which manifest as low-energy kinks in the dispersion). Quasiparticle lifetimes may also be extracted by measuring EDC and MDC peak widths.

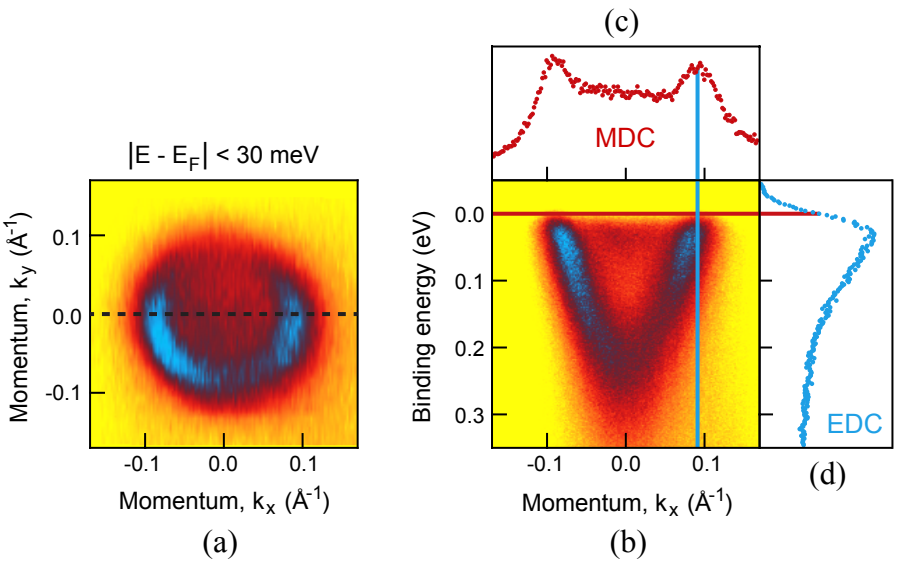

Figure 2.13: Real measurements showing typical arrangements of ARPES data. (a) A Fermi surface map shows spectral weight integrated within a small interval near the Fermi energy over an extended two-dimensional region of momentum space. This arrangement is beneficial for viewing Fermi surfaces. (b) An individual momentum space cut [dashed line in panel (a)] shows the spectral intensity as a function of energy and momentum. Band dispersions can be visualized clearly in this kind of display. (c) An MDC shows spectral intensity as a function of momentum at a fixed energy [red line in panel (b)]. (d) An EDC shows spectral intensity as a function of energy at a fixed momentum point [blue line in panel(b)].

Phenomenological models of the spectral function, such as the one discussed in Section 6.3 below, can be fit to EDCs in order to extract other kinds of parameters, such as superconducting energy gaps or the presence of band folding. In general, ARPES data is rich with information and there are countless ways to analyze and display it.

CHAPTER 3

MOLECULAR-BEAM EPITAXY

Molecular-beam epitaxy (MBE), sometimes described colloquially as "atomic spray painting," is a method of thin-film growth involving the evaporation of atoms onto the surface of a heated substrate and the corresponding crystallization of those atoms in registry with the substrate. In practice, the deposition rate of atomic layers is typically low ($\sim$3 monolayer/min for oxides), thereby allowing for control over the composition of single atomic layers. Indeed, MBE is the only existing technology that can control the placement of individual atoms on a large scale (albeit in one dimension only).

3.1 History

MBE was invented in the late 1960s at Bell Laboratories by A. Y. Cho and J. R. Arthur [30]. The technique was initially developed in order to understand the surface chemical reactions occurring during the growth of III-V compound semiconductors, but the method rapidly became a means of growing extremely high-purity materials [31]. Development of MBE in the 1970s and 1980s was driven largely by the growth of GaAs/Al_xGa_{1-x}As heterostructures, and the Nobel prize for the discovery of the fractional quantum hall effect was awarded to researchers studying high-mobility GaAs/Al_xGa_{1-x}As heterojunctions grown by MBE [32]. Today, state-of-the-art MBE systems are available commercially, and the manufacturing of electronic and optoelectronic semiconducting devices dominates the field [33]. The diode lasers in Blu-ray Disc players, for example, are manufactured by an MBE process.

3.1.1 Oxide MBE

The first example of oxide MBE was the growth of Al_2O_3 on $Al_xGa_{1-x}As$ in 1979 [34]. A few years later, the distorted perovskite $LiNbO_3$ was synthesized [35]. This was a critical historical development: the first demonstration of MBE growth of a multifunctional (ferroelectric, pyroelectric, and piezoelectric) crystalline oxide [36]. MBE became a valuable growth technique after the discovery of layered cuprate high-temperature superconductors in 1986 [18], allowing researchers to synthesize high quality superconducting films. During this period, advancements in the MBE technique included the use of reactive ozone [37] and better metal sources [38]. At the beginning of the 2000s, transmission electron microscopy and x-ray diffraction measurements revealed that oxide MBE films were approaching the structural quality of $GaAs/Al_xGa_{1-x}As$ heterostructures [39, 40]. Today, MBE is an extremely powerful growth technique for oxide thin films, particularly those with the perovskite or layered Ruddlesden-Popper structures [41, 42].

3.2 Experimental aspects

The basic principles of MBE are relatively simple, but there are a number of unique and complex experimental details that must be considered. Figure 3.1 shows a schematic diagram of a typical oxide MBE growth chamber. In addition to the pumps, valves, and gauges necessary for maintaining ultra-high vacuum, MBE chambers contain two essential categories of equipment: those necessary for the growth of films and those necessary for monitoring that growth. Not shown in Figure 3.1 is a transfer chamber and load lock, which are necessary in order to transfer substrates into and out of the growth module. The latest MBE systems are completely automated, transferring substrates between chambers with a robotic arm.

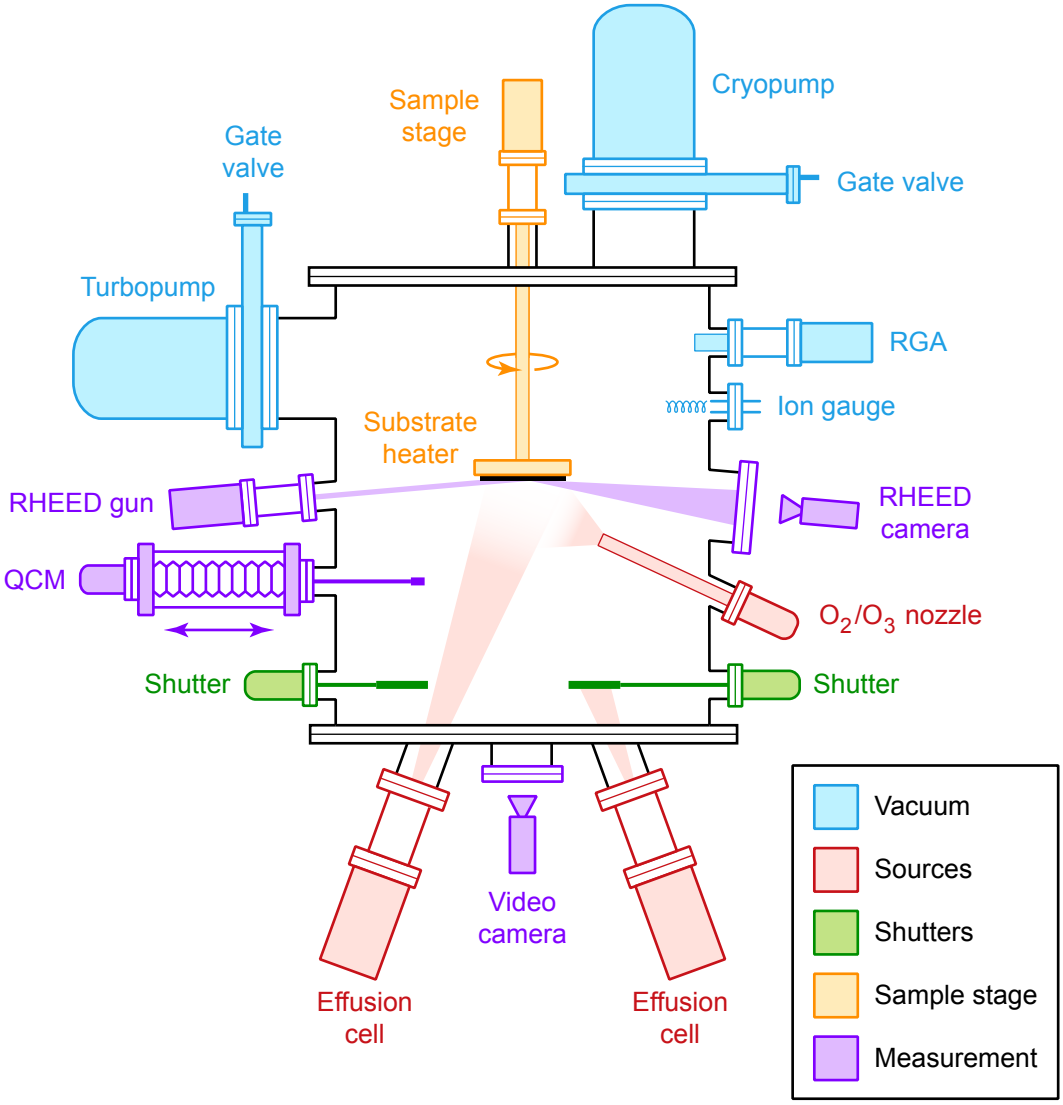

Figure 3.1: Schematic diagram of a typical MBE growth chamber. The parts of the system are colored based on their function: vacuum pumps and gauges (blue), sources (red), shutters (green), sample manipulation and heating (orange), and measurement/characterization (purple).

The components necessary to grow MBE films include a sample stage with a substrate heater, atomic effusion cells, an oxygen source, and shutters. The sample stage contains a silicon carbide heating element able to heat the substrate radiatively to temperatures above 1000 °C (although growth temperatures are usually significantly less). The temperature of the substrate is measured with a thermocouple; a pyrometer can be used to

verify the measurement. Most materials cannot withstand such high temperatures in an oxidizing environment, but certain stainless steel alloys, such as Haynes #217 [43], can endure such environments. In order to improve film quality, the substrate is often rotated by the sample stage during growth in order to average over atomic flux gradients. MBE is a line-of-sight technique; the substrate must be directly exposed to the atomic sources. Effusion cells therefore lie at the bottom of the growth module and point up towards the substrate. High-speed shutters control what sources are evaporating onto the substrate at which times.

The equipment necessary to characterize the growth of films include a quartz crystal microbalance (QCM), a reflection high-energy electron diffractometer (RHEED), and a video camera to monitor the substrate. The QCM is used during initial calibration of the atomic fluxes and helps determine the temperatures at which the effusion cells should be maintained for growth of films. RHEED is by far the most important characterization tool during growth and is used to fine-tune the shutter times so that only a single atomic layer is deposited after each shutter cycle.

3.2.1 Maintaining vacuum

MBE requires UHV environments because residual gases are much more likely to be adsorbed onto freshly deposited surfaces, where free chemical bonds are present. This can lead to incorporation of the gas molecules as impurities or to disruption of the growth process [44]. The vacuum apparatus for MBE systems—pumps, gauges, and valves—are very similar to those of ARPES systems; dry pumps such as turbomolecular pumps, cryopumps, ion pumps, and sublimation pumps are used for pumping, and Bayard-Alpert ionization gauges and RGAs are used to measure and characterize the level of vacuum.

The sizable volume of MBE growth chambers and large oxidant load necessitate the use of pumps with high capacities. In addition, most MBE chambers contain so-called "cryopanels," extensive internal surfaces that are cooled by liquid nitrogen in order to adsorb condensible gases (notably water and hydrocarbons) during particularly impurity-sensitive growths [31,44]. A special complication arises if ozone is used during growth: ozone will be adsorbed by a cryopump, creating a potential safety hazard when the cryopump is regenerated. Because of this, cryopumps on MBE growth chambers are gated off when ozone is being used.

3.2.2 Knudsen effusion cells

Requirements for atomic sources in MBE include reproducibility, stability, a uniform flux distribution over the substrate, an absence of impurities (for film quality), reliability, and low working temperature (in order to minimize outgassing). Knudsen effusion cells [45] (sometimes called "K-cells") satisfy these requirements and are used as molecular sources in nearly all MBE systems [33,44]. According to one manufacturer of commercial Knudsen cells:

> "Effusion cell design and construction are critical to the MBE process because the cells have a significant impact on the purity, composition, and uniformity of the grown layers. They also greatly affect system uptime and throughput. In fact, effusion cells are the most important components in an MBE system." [46]

Figure 3.2 shows a diagram of a Knudsen effusion cell. The cell contains a conical, open-faced crucible with a large exit aperture containing the evaporant element. The crucible is heated radiatively by tungsten or tantalum filaments and a thermocouple mea-

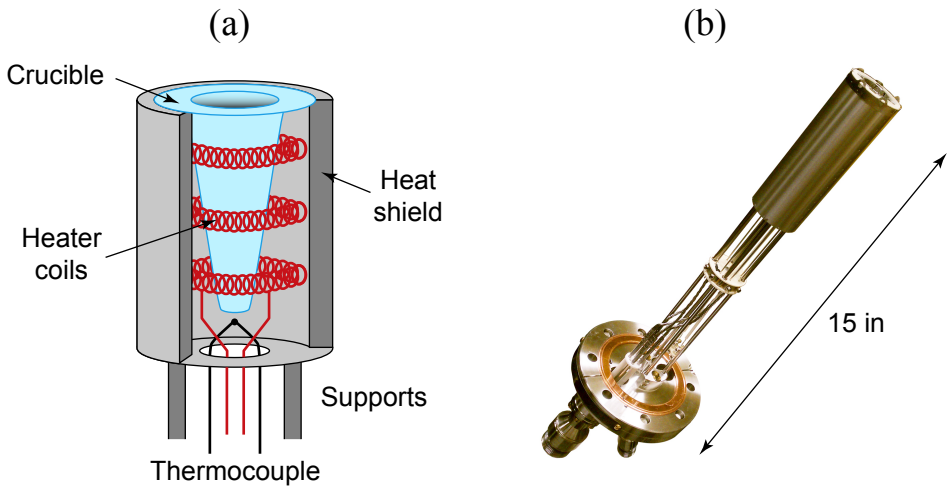

Figure 3.2: A Knudsen effusion cell. (a) Schematic diagram showing the head of a Knudsen effusion cell. Tungsten or tantalum heating filaments radiatively heat the conically-shaped crucible, and a thermocouple measures its temperature. The entire apparatus is surrounded by a heat shield. (b) Photograph of a Knudsen effusion cell.

sures the temperature in order to regulate the current flowing through the heating filaments via a feedback loop. One or more layers of a refractory metal are wrapped around the cell in order to minimize heat loss. Water cooling is used to cool the source flange. Some effusion cells are "dual filament," where two independent heaters control the temperature at the base of the crucible and at the tip near the crucible aperture. The tip temperature is usually held at 10 to 100 °C above the base in order to prevent condensation of the source element at the crucible lip.

Knudsen cells operate in the 200 to 1400 °C range [44], where they can be used to evaporate most elements. Table 3.1 shows typical source temperatures during growth for selected elements. There is no simple correspondence between the melting point of the element and the temperature of the source during growth because there is, in general, little correlation between melting point and vapor pressure. In some cases, the growth temperature exceeds the melting point of the element, highlighting the need for strict vertical alignment of sources. If the source is melted, it is usually maintained at a temperature

above the melting point even in an idle state in order to prevent cracking of the crucible upon solidification of the source material.

Table 3.1: Selected MBE source temperatures

Element	**Melting point (°C)**	**Growth temp. (°C)**
Ba	727	550
Bi	272	500
Ca	842	450
Cu	1085	1000
Fe	1538	1180
La	920	1400
Mn	1246	720
Ni	1455	1200
Sr	777	450

Depending on the source element, crucibles in Knudsen effusion cells can be constructed from a variety of materials. Careful attention must be made when choosing crucibles because of the possibility at high temperatures of forming a eutectic mixture of the crucible and the source element, which can have disastrous consequences. Common crucible materials include alumina, boron nitride, quartz, tungsten, and graphite, which are vacuum compatible even at high temperatures.

As discussed above, each effusion cell contains a thermocouple and an independent heater control unit that can be controlled via computer. The source heater power is continuously adjusted in order to maintain a stable desired temperature. For example, a feedback loop using proportional-integral-derivative (PID) control can regulate a source temperature to better than 0.1 °C. In PID control, the instantaneous heater power $P(t)$ is calculated using the equation

$$P(t) = C_P \Delta T(t) + C_I \int_0^t \Delta T(\tau) d\tau + C_D \frac{dT(t)}{dt}, \tag{3.1}$$

where $\Delta T(t) = T^* - T(t)$ is the difference between the set point temperature T^* and the instantaneous temperature $T(t)$ measured by the thermocouple at time t. C_P, C_I, and C_D

are constant gain factors that can be tuned based on the thermal properties of the source. With only the proportional term, the equilibrium temperature will clearly always be less than the set point temperature. With the integral term, this problem is remedied. The derivative term helps smooth the output of the heater and reduce overshoot effects.

Alternatives

For elements with exceptionally low vapor pressures (ruthenium or iridium, for example), Knudsen effusion cells cannot reach the high temperatures necessary to generate a sufficient flux for film growth. A different type of source is required. The most common alternative is the e-beam source, which can reach temperatures in excess of 2000 °C. An e-beam heater bombards the source element with a high-energy electron beam (5 to 12 keV, requiring 1 to 10 kW of power), heating the source material much more efficiently than through radiative heating [44]. The electron beam is usually scanned over the source material in a specific pattern in order to create a uniformly heated region and minimize the formation of hot spots. Users of e-beam sources must be extremely careful because of the risk of burning a hole through the MBE vacuum chamber with the electron beam!

3.2.3 Shutters

Shutters on MBE systems, although serving the relatively mundane purpose of blocking atomic fluxes generated by sources, are important because they must open and close well within the time needed to deposit one monolayer (generally less than 0.1 s [33]), and they must do so reliably for over a million cycles. The most common design for small MBE systems is a bellows-coupled shutter, where an external pneumatic actuator pushes a shutter in or out and motion is transfered into vacuum through a linear bellows. This

design ensures high reliability without the need for UHV bearings. Source shutter blades are usually bent into a 'V' shape in order to reduce the amount of heat reflected back into the source when the shutter is closed. Otherwise, the thermal environment of the cell will change depending on the position of the shutter, causing problems with the source heater control loop [44]. In addition to the source shutters, MBE systems usually have one large main shutter that is used to shield the substrate heater. This prevents evaporation onto the heater during QCM calibration, which can cause problems when the heater is later turned on for film growth.

3.2.4 Ozone generation

Oxide MBE systems must provide a source of oxygen during film growth. Although gaseous O_2 flowing into the growth chamber using a pressure-controlled leak valve is sufficient for certain kinds of films, a more powerful oxidizing agent is often required. The development of reactive ozone sources for MBE was driven by the desire to grow high-temperature superconducting cuprates in the early 1990s. Commercial ozone generators are limited to 10 to 15% O_3, produced by high voltage discharge from a gaseous O_2 supply. In order to increase the concentration of O_3 to 100%, an ozone still is necessary. Modern ozone stills use a silica gel in order to capture condensed O_3, allowing residual O_2 molecules to be pumped away [47, 48]. Figure 3.3 shows a schematic diagram of a distilled ozone source for an MBE system.

Ozone at high concentrations and elevated temperatures is toxic, unstable, and extremely dangerous. Numerous safety precautions must be taken when implementing an ozone system, including a so-called "blast cabinet" for the still. A reliable liquid nitrogen source is essential in order to keep the stored ozone at low temperatures. A dangerous

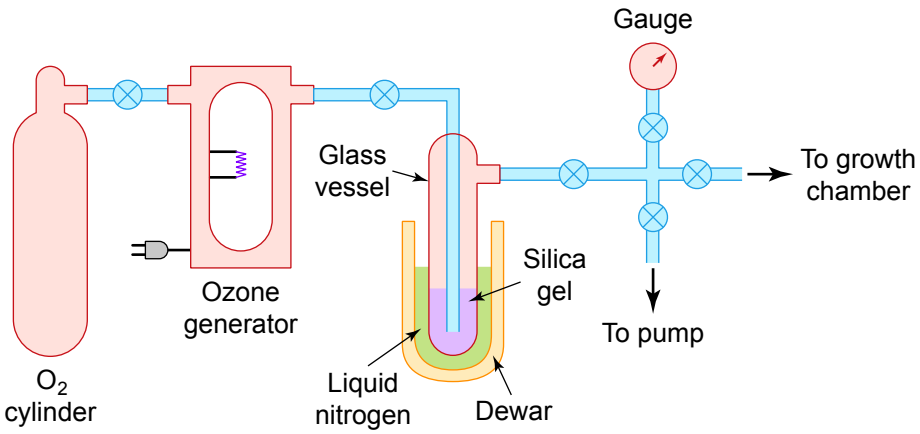

Figure 3.3: Schematic diagram of an ozone still. A commercial ozone generator, fed by a supply of high-purity O_2 gas, generates a continuous supply of $\sim$10% O_3, which is directed into a silica gel filled glass vessel cooled with liquid nitrogen. O_3 condenses and is captured by the silica gel and the residual O_2 is pumped away. Once the silica gel has been "charged" with a sufficient quantity of O_3, the charging process is halted and the glass vessel is slowely heated in order to boil off the ozone at a suitable rate for film growth.

situation can occur, for example, if power is lost to the building or the liquid nitrogen system breaks down. The explosive decomposition reaction

$$2O_3 \longrightarrow 3O_2 \tag{3.2}$$

releases 3 kJ of energy per gram of ozone, which is roughly half the explosive power of dynamite. The use of silica gel in modern ozone stills minimizes the risk of explosion by safely storing the ozone in an unreactive state.

All materials coming into contact with the ozone gas before it reaches the substrate, including the glass vessel, tubing, and valves, must be prevented from reacting with the ozone. Otherwise, the concentration of ozone in the growth chamber will be diminished. It is therefore often necessary to "passivate" new items in the ozone system by flowing a large quantity of ozone through them before growth can be accomplished.

3.2.5 Quartz crystal microbalance

A quartz crystal microbalance is an essential part of an MBE system because it is used in the first step of MBE film growth: determining the absolute molecular fluxes generated by the effusion cells. This information is used to set the temperatures of sources (so that a sufficient molecular flux is achieved) and ultimately to calculate the shutter times for each element in a film during growth. A QCM uses an oscillating (typically at $\sim$6 MHz) quartz crystal to detect changes in mass resulting from the accumulation of deposited atoms. As such, it directly detects accumulated mass rather than flux, but a simple differentiation and conversion factor can be applied to convert the mass change into an absolute atomic flux F:

$$F = \left(\frac{1}{MA}\right)\frac{dm}{dt}, \tag{3.3}$$

where M is the atomic mass of the source element, A is the area of the QCM oscillator exposed to the molecular beam, and dm/dt is the time rate of change of the oscillator mass. dm/dt is calculated based on the frequency shift and the acoustic impedance of the quartz oscillator [44].

The main assumption used when applying QCM measurements is that the measured flux is identical to the flux on the substrate during growth. This approximation can fail for a number of reasons, including geometrical effects and a material or temperature dependence of the atomic sticking coefficient. The former issue can be solved with a so-called "tooling factor," which corrects for the relative distances of the QCM and substrate to the effusion cells. The latter problem cannot be remedied; QCM flux calibration merely serves as the starting point for more precise and accurate methods, such as monitoring RHEED intensity oscillations.

3.2.6 Reflection high-energy electron diffraction

Reflection high-energy electron diffraction, known more commonly as RHEED, is a characterization tool whereby a beam of electrons at grazing incidence diffracts off the surface of a substrate/film and is detected by a fluorescent phosphor screen. The technique can yield extremely valuable real-time information about surface structure and quality and about film growth, which can be performed simultaneously. In fact, the detection of oscillations in the RHEED intensity, which occur when full atomic layers are deposited on a growing film, is the main calibration method for oxide MBE.

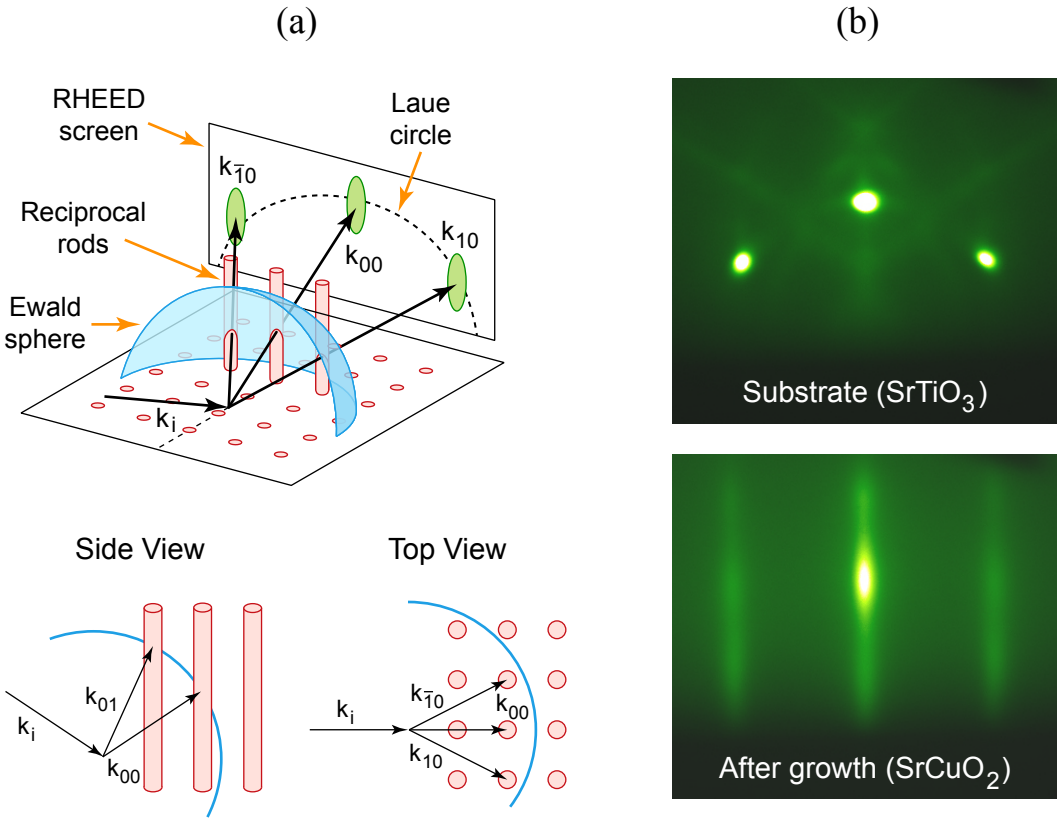

Figure 3.4: Characterization of a sample surface by RHEED. (a) Schematic diagram of the RHEED process, as described in the text. (b) Example RHEED images. The top image is a bare substrate, showing well defined diffraction peaks. The bottom image shows RHEED after MBE film growth, showing characteristic streaks.

Figure 3.4 shows a diagram of a RHEED system, as well as selected RHEED images before and after growth of a film. An electron gun generates a beam of electrons (typically at $\sim$10 keV) which is aimed at the substrate with momentum $\mathbf{k}_i$ (usually at a glancing angle of $\sim 5^\circ$). At the opposite side of the chamber, a phosphor-coated window detects the electrons that have diffracted off the sample surface. The small incidence angle of the electrons limits the diffraction to the topmost atomic layers of the film, and the reciprocal lattice of this two-dimensional system consists of arrays of rods parallel to the substrate surface normal vector. The Bragg diffraction condition is fulfilled whenever these rods intersect the Ewald sphere of the incident electron beam. The corresponding image formed at the phosphor screen is composed of peaks falling on so-called "Laue circles." Each peak can be labeled with a two-dimensional diffraction order (for example, $\mathbf{k}_{10}$ or $\mathbf{k}_{\bar{1}0}$). RHEED images of films often show "streaks" rather than peaks because of crystal imperfections, which broaden the diameter of the reciprocal rods. When these rods intersect the Ewald sphere (which is also broadened because of the finite divergence and energy spread of the electron beam) long streaks rather than peaks are formed [49].

3.3 Growth

The growth of MBE films is as much an art as it is a science. The two main methods of growth are codeposition, in which thermodynamics dictates the formation of stoichiometric crystalline samples, and shuttered layer-by-layer deposition, where the evaporation of individual atomic layers is controlled so that complex films and superlattices can be built up. With these different MBE methods, there are a number of physical modes of film growth, and RHEED intensity oscillations and the choice of substrate play immensely important roles.

3.3.1 Growth methods

If possible, codeposition is the first choice for the growth of a material because it is comparatively easy, not requiring precise absolute calibration of fluxes (although flux ratios may be important). Unfortunately, many materials cannot be grown by codeposition, usually because of structural complexity (for example, superlattices with large periods). In this case, shuttered layer-by-layer growth is necessary.

Codeposition

Historically, the first MBE growth technique to be developed was codeposition, which is used to grow compound semiconductors. In codeposition, the substrate is exposed to fluxes from all elements at the same time. Often the ratio of elemental fluxes can be far off stoichiometry (not "congruent"), but thermodynamic effects ensure stoichiometric films. When growing GaAs, for example, As_2 molecules are only adsorbed on the film surface if previously-deposited free gallium atoms are available to form bonds. By flooding the substrate with As_2, one can control the growth of GaAs films with the gallium flux alone, since excess arsenic atoms will leave the surface [30].

Other materials can be grown using codeposition as long as source fluxes are in the right stoichiometric ratio. Film growth is then dictated by the phase diagram of the material, which, if known, can tell the grower what substrate temperature and oxidant pressure to use. In this case, the material forms much like in solution-phase growth, where mobile atoms on the surface diffuse and crystallize to lower the free energy of the system. In codeposition, film thickness is controlled by monitoring RHEED intensity oscillations, where each period corresponds to one monolayer of growth.

Shuttered layer-by-layer growth

Part of the power of the MBE technique lies in the ability to synthesize nontrivial films such as superlattices, heterostructures, or other systems impossible to create with conventional crystal growth methods. For these kinds of metastable systems, the free energy difference between the desired structure and a manifold of other crystal phases is so small that thermodynamics alone cannot be used to control growth. Instead, these films are grown actively using shuttered layer-by-layer deposition, where precise control over the composition of individual atomic layers is possible. In layer-by-layer growth, the flux of each element must be determined with absolute accuracy. The oxidant gas flows continuously and shuttering restricts metal and cation atoms to be deposited one monolayer at a time (or less than a monolayer in the case of dopants). The growth temperature is chosen in order to kinetically limit decomposition of the deposited layers [44]. With current techniques, the accuracy of absolute fluxes using RHEED calibration can reach $\sim$1% [33, 50], allowing for the growth of high-quality oxide films.

3.3.2 Growth modes

Experimentally, three main mechanisms of epitaxial film growth have been observed: Volmer–Weber island growth [51], Stranski–Krastanov mixed growth [52], and Frank–van der Merwe layer-by-layer growth [53]. The latter mode is the only one acceptable for growing thin films using the shuttered layer-by-layer MBE technique. Figure 3.5 illustrates the three modes.

In Volmer–Weber island growth, discrete finite islands of adsorbate are formed, each of which grows as more atoms are deposited. Three-dimensional aggregates form because of a strong attraction between adsorbates or insufficient surface diffusion (due, for

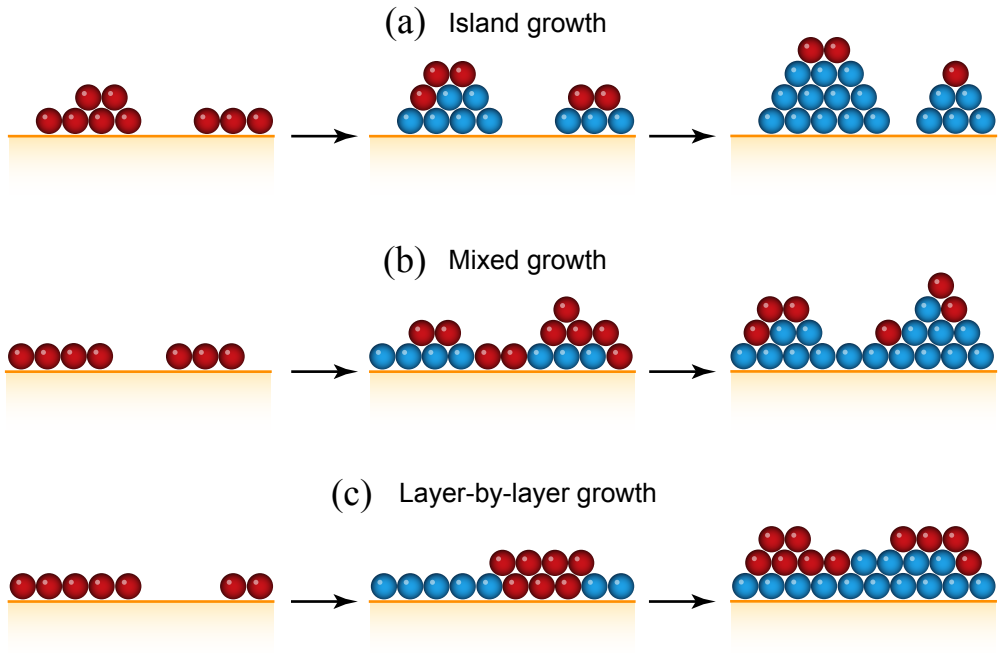

Figure 3.5: Modes of epitaxial film growth. Newly-deposited atoms are shown in red. (a) Volmer–Weber island growth, where discrete three-dimensional aggregates form due to a strong attraction between atoms or insufficient surface diffusion. (b) Stranski–Krastanov mixed growth, where initial atomic layers lower the energy barrier for island formation. (c) Frank–van der Merwe layer-by-layer growth, where monolayers are deposited consecutively because of fast surface diffusion.

example, to a low growth temperature). Islands preferentially nucleate at substrate defect sites. RHEED patterns during Volmer–Weber island growth resemble spots rather than streaks, often indicating the need to increase the substrate temperature.

In Frank–van der Merwe layer-by-layer growth, adsorbate atoms are added in complete layers, which is analogous to total wetting of the film surface at each time period corresponding to the deposition of one monolayer. This method is assisted by fast surface diffusion of atoms. Usually, growth of a single layer occurs via step-edge propagation, whereby newly deposited atoms migrate to the boundary contour of the newly forming monolayer and attach there, growing the boundary. The Frank–van der Merwe growth mode matches the shuttered layer-by-layer deposition method and is the goal during

MBE growth, resulting in films with the highest crystalline quality. RHEED patterns during Frank–van der Merwe layer-by-layer growth will show streaks rather than spots, and RHEED intensity oscillations will be stable.

Finally, in Stranski–Krastanov mixed growth, a combination of island and layer-by-layer growth occurs. Frank–van der Merwe layered growth occurs first for a finite number of monolayers, followed by Volmer–Weber island growth on top of those layers. The transition occurs due to a change in energetics, usually after the substrate has been wetted by the adsorbate.

3.3.3 RHEED oscillations

The observation of RHEED intensity oscillations during growth is a crucial factor in the synthesis of high-quality multicomponent oxide thin films [50, 54]. RHEED oscillations show the total integrated intensity of a RHEED streak (usually the first-order $\mathbf{k}_{10}$ or $\mathbf{k}_{11}$ peak) as a function of time as material is deposited on the substrate. Intensity oscillations allow fluxes to be calibrated with high precision, serve as an *in situ* measure of the rate of growth (for example, allowing the counting of monolayers), and enable characterization of surface structure and quality.

Figure 3.6 illustrates the qualitative theory of RHEED oscillations. As atoms are deposited during Frank–van der Merwe growth, the surface of the film changes from smooth to rough (at half coverage) and back to smooth at the completion of one monolayer. When the film surface is smooth, RHEED diffraction intensities are maximal; when the surface is rough, destructive interference of the electron beam suppresses the diffraction, causing minima in the measured intensity. The net result is an oscillating RHEED intensity commensurate with the layer-by-layer growth of the film. A count of the total

number of oscillation periods yields the number of atomic layers in the film [44, 54, 55]. As film growth progresses, the amplitude of the RHEED oscillations will dampen because the structural quality of the film will degrade. At the end of growth, the RHEED intensity often rises rapidly as the surface of the film relaxes and recovers long-range order.

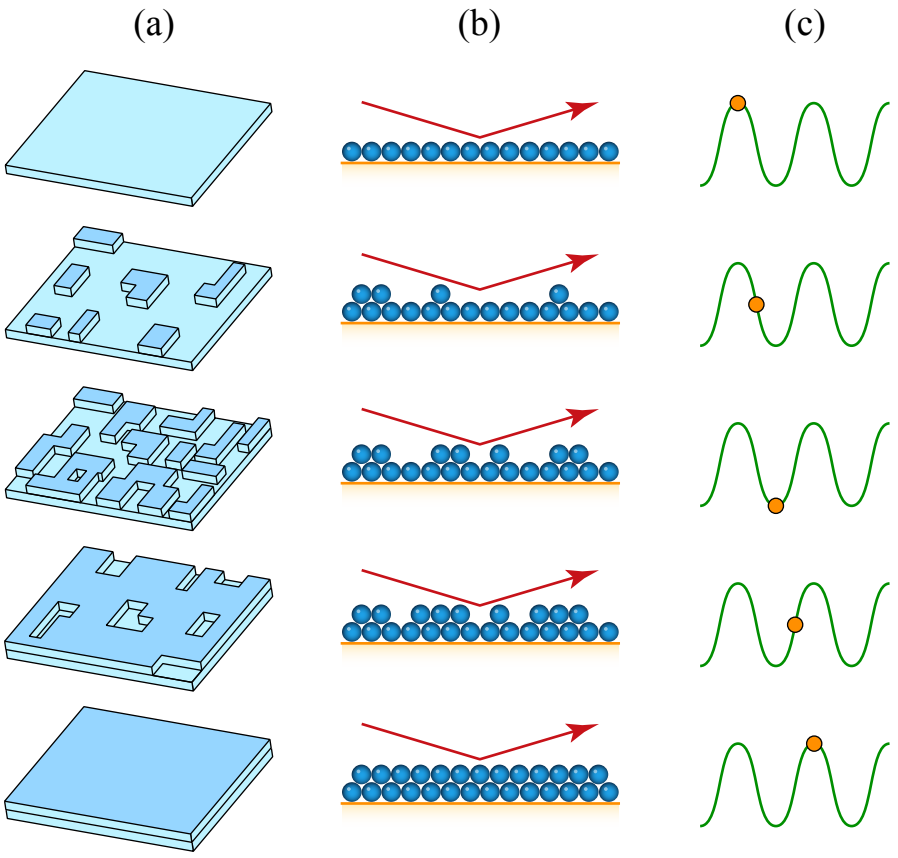

Figure 3.6: Qualitative theory of RHEED intensity oscillations. As a new atomic monolayer is deposited, the surface of the film first roughens and then smooths. RHEED spots are least intense at maximum surface roughness, when half a monolayer has been deposited. (a) Three-dimensional schematic view of the growing film. (b) Side view showing diffraction of the RHEED electron beam off the atoms of the film. (c) RHEED intensity oscillations.

The above qualitative explanation is somewhat simplified; reality is a far more complicated beast. For example, Figure 3.7 shows RHEED oscillations during the growth of a $SrCuO_2$ film. The intensity increases as a monolayer of strontium atoms is deposited, but then decreases upon deposition of copper atoms. This behavior cannot be explained

by the simple model discussed above. Indeed, much theoretical and experimental work remains in order to elucidate the mechanism of RHEED oscillations in the growth of complex oxide materials. Because of this, RHEED intensity oscillations are primarily used for the qualitative, rather than quantitative, characterization of film growth.

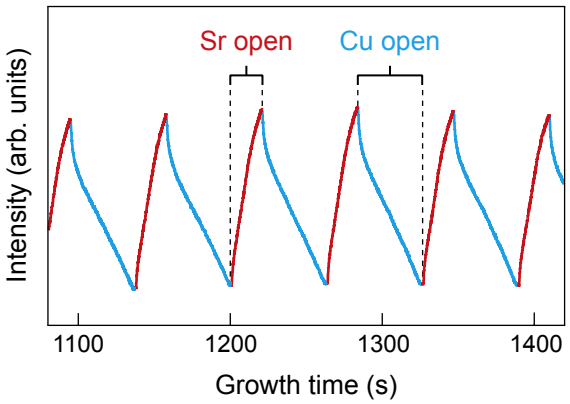

Figure 3.7: Example of RHEED oscillations in the middle of the growth of a $SrCuO_2$ film. RHEED intensity rises during the deposition of Sr atoms and falls during the deposition of Cu atoms.

3.4 Substrates

The choice of substrate is an immensely important factor in the growth of MBE films. Lattice matching plays a large role in determining if a material can be grown on a certain substrate, and substrate quality can affect film growth and quality because MBE is an epitaxial process. Furthermore, the availability of exotic substrates is sometimes limited, and access to these rare substrates can be crucial for the growth of certain materials.

Most oxide materials grown by MBE take the cubic perovskite (ABO_3) or tetragonal Ruddlesden-Popper ($A_{n+1}B_nO_{3n+1}$) structures [41, 42]. In fact, the perovskite structure is the limiting case of the Ruddlesden-Popper series when $n \rightarrow \infty$. Figure 3.8 shows the perovskite unit cell. The B-site metal atoms, surrounded by oxygen octahedra, are

separated by the A-site cations. In the layered Ruddlesden-Popper materials (Figure 3.9), a slab of n perovskite ABO_3 layers is separated by a single AO layer. These materials therefore often exhibit more two-dimensional electronic structure due to the suppression of tunneling between adjacent metallic ABO_3 slabs by the insulating AO layers.

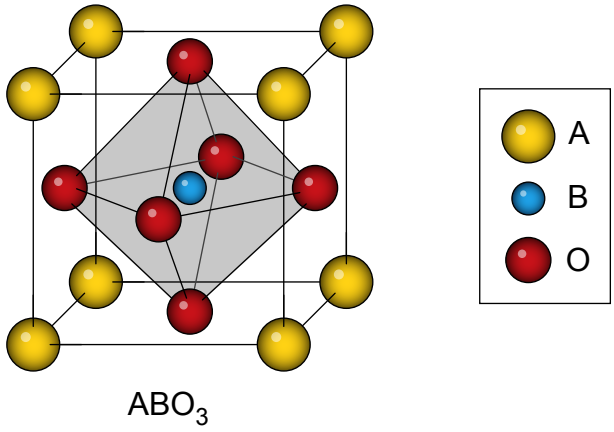

Figure 3.8: The ABO_3 perovskite unit cell consists of A-site cations at the eight corners of a cube, with the B-site sitting in the middle and surrounded by an octahedral cage of oxygen atoms (shaded gray).

Fortunately, the wide variety of perovskite and Ruddlesden-Popper oxides have similar in-plane lattice constants. Therefore, one may be used as a substrate for another, and two or more may be grown adjacently to form a multicomponent superlattice. By using a substrate with a slightly mismatched (up to ~2%) lattice constant, both compressive and tensile strained films may be grown. Table 3.2 displays some commonly available substrates used in oxide MBE. Substrates with $a \neq b$ are those supporting a distorted perovskite structure due to slight octahedral rotations of the oxygen atoms.

The development of etching recipes for a number of common substrates used in MBE [56, 57] has contributed significantly to progress in the growth of high-quality oxide thin films. For example, the most common and widely available substrate for MBE, $SrTiO_3$, can be etched so that an atomically flat TiO_2-terminated step-and-terrace surface

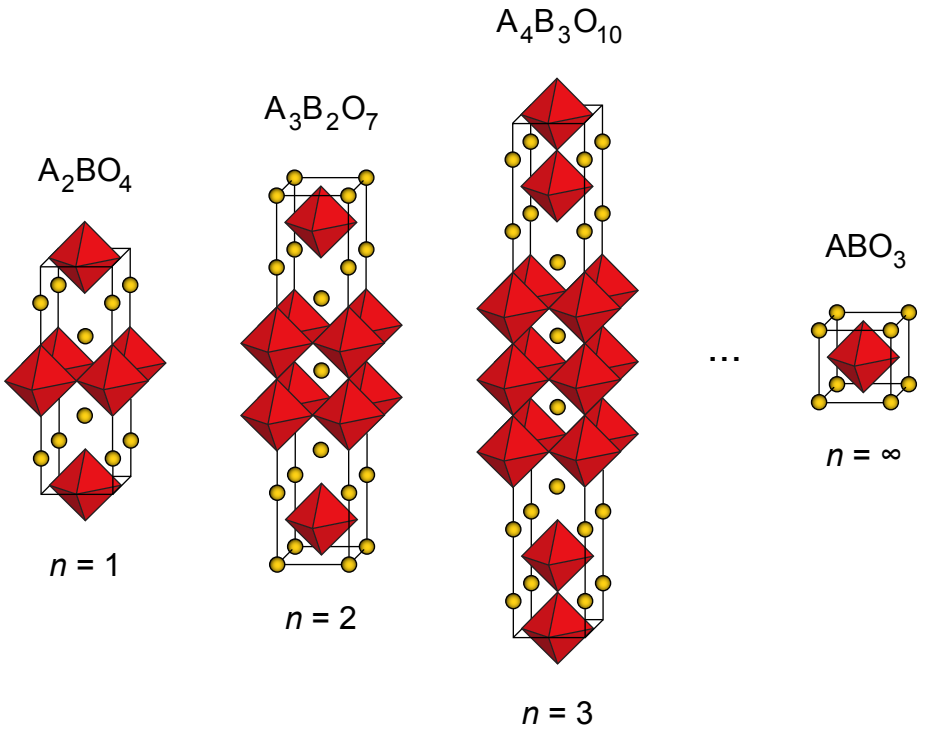

Figure 3.9: The Ruddlesden-Popper series $A_{n+1}B_nO_{3n+1}$ consists of a slab of n perovskite ABO_3 layers separated by a single AO layer. The most two-dimensional structure is $n = 1$ and the most three-dimensional is $n = \infty$, which corresponds to the cubic perovskite structure shown in Figure 3.8.

is ensured. The etch recipe involves treating the $SrTiO_3$ substrate first with water [to form $Sr(OH)_2$] and then with an NH_4F-buffered HF acid solution, which dissolves the $Sr(OH)_2$ on the surface of the substrate. Etching of rare-earth scandate substrates involves treating the substrate with a NaOH solution, dissolving the rare-earth ion and leaving ScO_2-terminated surfaces.

Along with an optional etching procedure, substrates used in MBE are often annealed to improve the surface quality. This can drastically improve the properties of films grown on such substrates. In addition, all substrates are backside-coated with 10 nm of titanium (a wetting layer) and 200 nm of platinum via sputtering. This creates an opaque layer on the underside of the substrate, enabling radiative coupling of the substrate heater to the

substrate. Otherwise, the infrared radiation would be transmitted through the optically transparent substrate, resulting in inefficient and slow heating.

Table 3.2: Common substrates for MBE

Substrate	**Orientation**	**a (Å)**	**b (Å)**	**Etch?**
$GdScO_3$	(110)	3.966	3.970	Yes
$DyScO_3$	(110)	3.946	3.952	Yes
$SrTiO_3$	(100)	3.905	—	Yes
LSAT	(100)	3.868	—	No
$NdGaO_3$	(110)	3.854	3.862	No
$LaAlO_3$	(100)	3.821	—	No

CHAPTER 4

CUPRATE SUPERCONDUCTORS

Superconductivity is a quantum phenomenon in which, at sufficiently low temperatures, electrons in a material condense into a macroscopic quantum state displaying no electrical resistance and the complete expulsion of magnetic field. Most superconductors operate at extremely low temperatures, but one material family, the cuprates, displays superconductivity under relatively warm conditions. Because the mechanism of superconductivity in the cuprates is not yet understood and because of the potential revolutionary applications of a room-temperature superconductor, the cuprates remain one of the most well-studied systems in condensed matter physics.

4.1 History of superconductivity

In 1911, soon after the cryogenic apparatus was developed to liquefy helium, thereby allowing access to unprecedentedly low temperatures, H. Kamerlingh Onnes discovered superconductivity [58]. He was studying the electrical resistance of mercury as a function of temperature and noticed an abrupt transition into a zero-resistance state at 4.2 K. For his discovery, which he named superconductivity, Onnes was awarded the 1913 Nobel Prize in Physics. Other elemental metals were soon discovered to superconduct, each with its own critical temperature T_c, including lead at 7.2 K (discovered in 1913) and niobium at 9.3 K (discovered in 1930). The state of matter discovered by Onnes was unlike anything ever before encountered, defying physical intuition: the persistence time for current flowing around a superconducting ring has been measured to be larger than 10^5 years and the theoretical lifetime is orders of magnitude longer than the age of the universe [59]!

4.1.1 The Meissner effect

Zero resistance is perhaps the most striking feature of superconductivity, but another defining property is the complete expulsion of magnetic field. This perfect diamagnetism, called the Meissner effect, was discovered by W. Meissner and R. Ochsenfield in 1933 [60]. It should be noted that the Meisnner effect, illustrated in Figure 4.1, cannot be explained by perfect conductivity alone, which would tend to lock magnetic flux inside the superconductor at the transition rather than expel it completely.

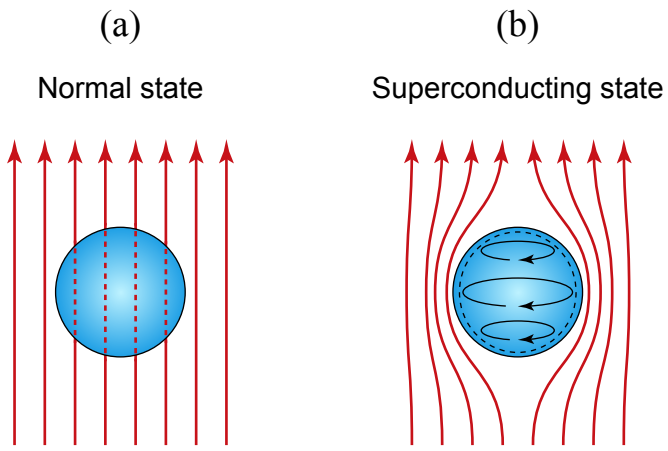

Figure 4.1: Illustration of the Meissner effect. (a) Above T_c in the normal state, magnetic flux lines penetrate the material. (b) Below T_c in the superconducting state, magnetic flux is completely excluded from the superconductor due to circulating electrical currents. The dashed line shows a thin shell-like region at the surface of the superconductor over which the magnetic field is suppressed.

In reality, the magnetic field does not terminate abruptly at the surface of the superconductor. Instead, flux penetrates into the superconductor over a microscopic length scale called the penetration depth, which is on the order of 10 to 1000 nm depending upon the material. The Meissner effect implies that a sufficiently strong magnetic field will destroy superconductivity when the energy required to readjust the magnetic field distribution exceeds the condensation energy of the superconducting phase.

4.1.2 Material families

After the initial discovery of superconductivity, there was a slow but steady progression towards ever-higher transition temperatures. Figure 4.2 shows a timeline of the highest known T_c for the four main superconducting material categories known today. The first class of superconductors, the so-called conventional superconductors, were elemental metals and simple binary compounds. Then, in 1979, superconductivity was discovered in a heavy-fermion material, where occupied f-orbitals strongly influence magnetic interactions [61].

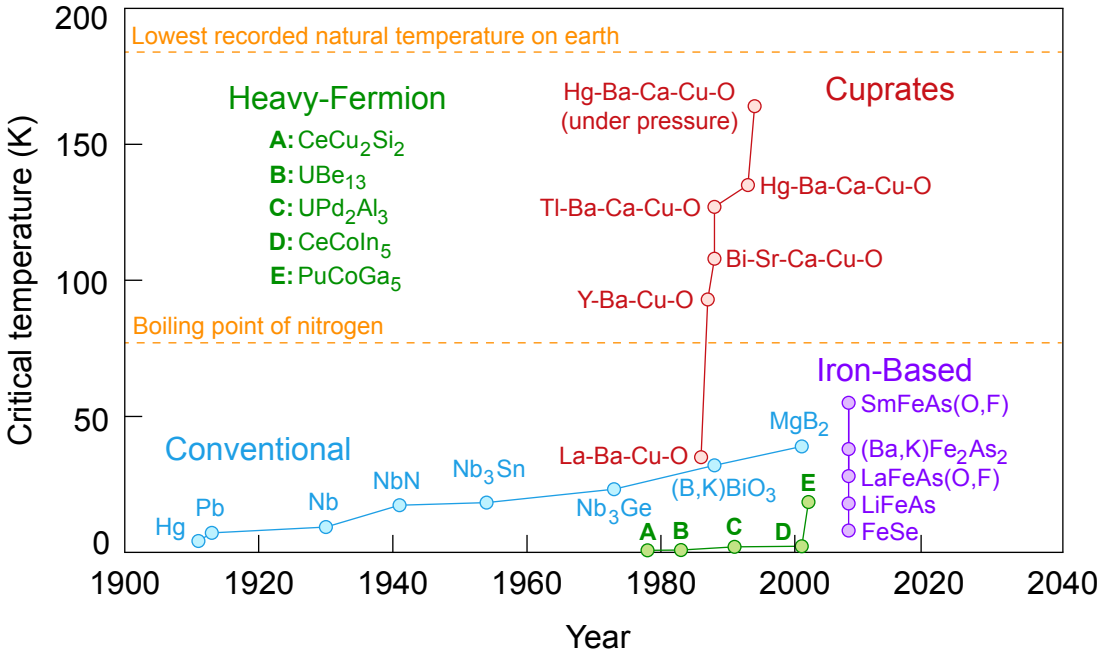

Figure 4.2: Critical temperatures for selected superconducting materials as a function of discovery year. The materials are divided into four distinct categories: conventional superconductors (blue), heavy-fermion superconductors (green), cuprates (red), and iron-based superconductors (purple).

A profound revolution occurred in 1986 when J. G. Bednorz and K. A. Müller discovered superconductivity at 35 K in a ceramic La-Ba-Cu-O compound [18]. The next year they were awarded the Nobel Prize in Physics for their discovery. In that same year, the

maximum T_c of the cuprates was pushed to 93 K with the discovery of the Y-Ba-Cu-O family [62]. This was a significant milestone because, for the first time, superconductivity could be induced with liquid nitrogen cooling, a relatively inexpensive refrigerant.

Another revolution occurred in 2008 when superconductivity was discovered at 26 K in an iron pnictide material [63]. A host of related iron-based superconductors were synthesized within a few months of that discovery, and much of the excitement of that time can be attributed to the hope that studying the iron-based superconductors would help solve the problem of the cuprates. Despite the continual discovery of new superconducting materials, today no material family comes close to the transition temperatures of the cuprates.

4.1.3 Theories of superconductivity

It took more than four decades after the discovery of superconductivity for physicists to develop a satisfactory theory. The phenomenological London equations proposed in 1935 helped researchers understand the electrodynamic properties of superconductors, but did not offer a microscopic picture [64]. V. L. Ginzburg and L. D. Landau made headway in 1950 by proposing a macroscopic coarse-grained superconducting wavefunction [65]. But it was in 1957 that J. Bardeen, L. N. Cooper, and J. R. Schrieffer published what is now known as the "BCS Theory," offering the first microscopic mechanism of conventional superconductivity and revolutionizing the field [66]. For their work, they won the 1972 Nobel Prize in Physics.

The London equation

In 1935, the brothers H. and F. London proposed an equation describing the magnetic field within a superconductor [64]:

$$\mathbf{B} = -\mu_0 \lambda^2 \nabla \times \mathbf{J}, \tag{4.1}$$

where $\lambda = \sqrt{\epsilon_0 mc^2/n_s e^2}$ is a constant related to the density of superconducting electrons and **J** is the superconducting current density. Taking the curl of Ampère's Law and substituting in Equation 4.1, one arrives at the expression

$$\nabla^2 \mathbf{B} = \frac{\mathbf{B}}{\lambda^2}. \tag{4.2}$$

Thus, external magnetic field are exponentially screened within a superconductor, with characteristic decay length λ. For example, in the case of a flat semi-infinite slab of superconducting material with a constant external magnetic field B_0 pointing parallel to the boundary surface, the magnitude of the field within the superconductor will decay as

$$B(z) = B_0 e^{-z/\lambda}, \tag{4.3}$$

where z is the distance into the superconductor from the surface. The London equation therefore immediately explains the Meissner effect.

Ginzburg-Landau theory

The next step in developing a theory of superconductivity was taken by V. L. Ginzburg and L. D. Landau, who in 1950 proposed a complex wavefunction $\psi(\mathbf{r})$ as an order parameter of superconductivity within Landau's theory of second-order phase transitions [59, 65]. In the theory, the squared magnitude of the order parameter represents the density $n(\mathbf{r})$ of superconducting electrons:

$$n(\mathbf{r}) = |\psi(\mathbf{r})|^2 . \tag{4.4}$$

By expanding the free energy of the superconductor in powers of ψ and $\nabla\psi$, Ginzburg and Landau were able to derive a differential equation guiding the form of ψ:

$$\frac{1}{2m^*}\left(\frac{\hbar}{i}\nabla - \frac{e^*}{c}\mathbf{A}\right)^2 \psi + \beta\left|\psi\right|^2\psi + \alpha(T)\psi = 0, \tag{4.5}$$

where m^* and e^* are the mass and charge of the superconducting carriers and $\alpha(T)$ and β are expansion coefficients of the free energy. This is equivalent to Schrödinger's equation for a free particle, but with the addition of a nonlinear term. The equation introduces a new length scale, called the coherence length, which describes distances above which the superconducting order parameter can vary without unduly increasing the free energy.

The triumph of the Ginzburg-Landau theory was the ability to treat spatial variations of the superconducting density and the suppression of superconductivity by magnetic fields. In 1957, A. A. Abrikosov used the theory to show that for materials where the coherence length is less than the penetration depth (type-II superconductors), two transitions occur as a function of magnetic field [67]. At the lower critical field, H_{c1}, magnetic flux penetrates the superconductor and forms so-called "vortices" of supercurrent: tubes with $\psi(\mathbf{r}) = 0$ carrying one quantum of flux. Only at a higher critical field, H_{c2}, is superconductivity completely suppressed. Abrikosov also predicted that the vortices would form a regular array, called an Abrikosov lattice, and this prediction has since been confirmed by a number of experimental techniques.

The BCS theory

In 1956, L. N. Cooper proposed that electrons with opposite momenta in a Fermi sea would form a bound singlet pair if there existed an arbitrarily weak net attraction between them [68]. He pointed out that in superconductors this behavior could explain the energy gap of size $\sim k_B T_c$ that many experiments had detected. A year later, Cooper, with

J. Bardeen and J. R. Schrieffer, published what is now known as the "BCS theory," offering the first microscopic mechanism of conventional superconductivity [66]. The BCS theory proposed that the electron-phonon interaction in superconductors gives rise to a net attractive force between electrons, forming Cooper pairs. When these bosonic pairs condense into a wavefunction with a single macroscopic phase, a superconducting state arises.

The mechanism of the phonon-mediated attraction within the BCS theory, illustrated in Figure 4.3, was first proposed by H. Fröhlich in 1950. He noted that the exchange of phonons could produce an attractive electron–electron interaction [69], which can be understood by considering the separation of time scales between electron and lattice dynamics. When an electron moves through the lattice, the positively-charged ions are polarized. The lattice remains distorted after the electron leaves, creating a channel of positive charge that attracts the electron with opposite momentum. The close relationship between phonons and superconductivity did not come as a surprise when the BCS theory emerged; previous experiments had demonstrated an "isotope effect" in which T_c was shown to have a dependence on the masses of the lattice ions [70,71].

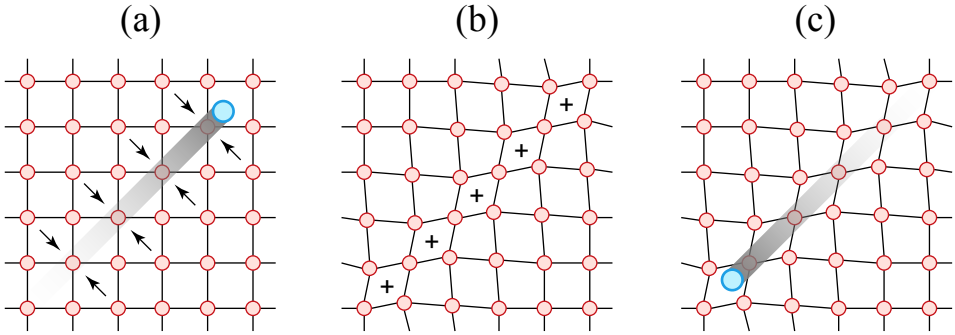

Figure 4.3: Cartoon showing the mechanism of phonon-mediated pairing in the BCS theory. (a) An electron travels through the lattice, polarizing the positively-charged ions in its wake. (b) The fast-moving electron leaves, but the distorted lattice has a slower response time. A channel of positive charge is created along the trajectory of the electron. (c) An electron with opposite momentum travels through the channel, lowering its energy.

As mentioned above, in the BCS theory superconductivity arises as a result of the condensation of Cooper pairs. This condensed state is represented by the BCS wavefunction

$$|\Psi_{BCS}\rangle = \prod_{\mathbf{k}} \left(u_{\mathbf{k}} + v_{\mathbf{k}} \hat{c}^{\dagger}_{\mathbf{k}\uparrow} \hat{c}^{\dagger}_{-\mathbf{k}\downarrow}\right) |0\rangle \,, \tag{4.6}$$

where $u_{\mathbf{k}}$ and $v_{\mathbf{k}}$ are variational parameters subject to the constraint $|u_{\mathbf{k}}|^2 + |v_{\mathbf{k}}|^2 = 1$ and $|0\rangle$ represents the filled Fermi sea. Essentially, $v_{\mathbf{k}}$ represents the probability density that the Cooper pair $(\mathbf{k}\uparrow, -\mathbf{k}\downarrow)$ is occupied. The parameters $u_{\mathbf{k}}$ and $v_{\mathbf{k}}$ are complex numbers, and their $\mathbf{k}$-independent phase difference represents the phase of the macroscopic condensate wavefunction—the phase of Landau and Ginzburg's $\psi(\mathbf{r})$ function.

Assuming a simple pairing Hamiltonian, the energy of the BCS wavefunction can be minimized variationally, giving expressions for $u_{\mathbf{k}}$ and $v_{\mathbf{k}}$:

$$v^2_{\mathbf{k}} = \frac{1}{2}\left(1 - \frac{\epsilon_{\mathbf{k}}}{\sqrt{\Delta^2 + \epsilon^2_{\mathbf{k}}}}\right), \tag{4.7}$$

$$u^2_{\mathbf{k}} = 1 - v^2_{\mathbf{k}}, \tag{4.8}$$

where $\epsilon_{\mathbf{k}}$ is the underlying band dispersion of the material relative to the chemical potential and Δ is an energy scale related to the electron-phonon coupling. In the weak-coupling limit, BCS derived an expression for Δ in terms of the lattice Debye energy $\hbar\omega_D$, the density of states at the Fermi level $N(0)$, and the effective electron-phonon interaction potential V:

$$\Delta \approx 2\hbar\omega_D e^{-1/N(0)V}. \tag{4.9}$$

It is interesting to note that this is a non-analytic function of the coupling constant, a property that contributed to the difficulty in developing a theory of superconductivity using perturbation methods [59]. A number of other results can be derived from the BCS wavefunction, including the temperature dependence of the energy gap near the superconducting transition ($T \approx T_c$):

$$\frac{\Delta(T)}{\Delta(0)} \approx 1.74\sqrt{1 - \frac{T}{T_c}}, \tag{4.10}$$

the energies of elementary excitations:

$$E(\mathbf{k}) = \sqrt{\Delta^2 + \epsilon_{\mathbf{k}}^2}, \tag{4.11}$$

and the electronic density of states:

$$\frac{N(E)}{N(0)} = \frac{E}{\sqrt{E^2 - \Delta^2}}. \tag{4.12}$$

The last two expressions show that in the superconducting state, an energy gap of size 2Δ is formed around the chemical potential. The spectral weight normally falling within the gap is pushed outside it, forming so-called "coherence peaks" at $E = \pm\Delta$. One of the key predictions of the BCS theory is that $\Delta = 1.764 k_B T_c$. This prediction has been tested by numerous experiments and has been found to hold to a good approximation in many conventional superconductors. The energy gap is the key to resistanceless conduction: if the temperature is low enough, crystal imperfections and thermal fluctuations will not be sufficiently energetic to break Cooper pairs, and they may flow freely.

The original BCS theory is a fairly simplistic weak-coupling [$N(0)V \ll 1$] model in which the phonon dispersion and other properties of the lattice are completely neglected. Soon after its introduction, A. B. Migdal and G. M. Eliashberg were able to refine the BCS theory by properly handling the electron-phonon interaction, including in the theory spatial locality and time retardation effects [72, 73]. With this improved strong-coupling method, researchers were able to calculate the expected superconducting transition temperature of materials. Based on realistic phonon properties, many researchers predicted that superconductors with transition temperatures exceeding ~30 K could not exist. That prediction was falsified with Bednorz and Müller's discovery of the cuprates.

Theories of cuprate superconductivity

To date, no consensus has been reached on the microscopic mechanism of high-temperature superconductivity, but a number of general conclusions have been drawn by comparing properties across the entire cuprate family [74]. For example, the parent compounds of the cuprates are antiferromagnetic insulators, and chemical doping is required to destroy the antiferromagnetism and induce superconductivity. In addition, all superconducting cuprates are layered materials with two-dimensional CuO_2 planes. In some cases, individual planes are isolated from each other by layers of other atoms, and in other cases they form slabs of two or more adjacent planes within the crystal cell. Although it is clear that superconductivity originates in the two-dimensional CuO_2 planes, superconducting currents can flow in all three dimensions because of inter-plane coupling. Table 4.1 lists some common cuprate superconductors.

Table 4.1: Selected cuprate superconductors

Material	T_c **(K)**	**Doping**
$Nd_{2-x}Ce_xCuO_4$	24	n-type
$La_{2-x}Sr_xCuO_4$	38	p-type
$Sr_{1-x}La_xCuO_2$	42	n-type
$YBa_2Cu_3O_7$	92	p-type
$Bi_2Sr_2Ca_2Cu_3O_{10}$	110	p-type
$Tl_2Ba_2Ca_2Cu_3O_{10}$	125	p-type
$HgBa_2Ca_2Cu_3O_8$	130	p-type

Superconductivity in the cuprates differs markedly from the BCS-like picture. First, properties are highly anisotropic due to the layered nature of the cuprates (whereas most conventional superconductors are three-dimensional). Second, superconducting coherence lengths are much smaller, suggesting an entirely different pairing mechanism than phonon exchange. Finally, the superconducting gap has a different symmetry than conventional superconductors: whereas in the BCS theory the energy gap Δ is assumed to

be independent of $\mathbf{k}$ (s-wave symmetry), in all of the cuprate superconductors, gaps with a d-wave ($\Delta_{\mathbf{k}} \propto k_x^2 - k_y^2$) dependence—a symmetry lower than that of the underlying crystal lattice—have been measured by phase sensitive experiments [75, 76]. The d-wave symmetry of the gap, illustrated in Figure 4.4, reveals crucial information about the mechanism of pairing in the cuprates, suggesting for example the importance of spin degrees of freedom.

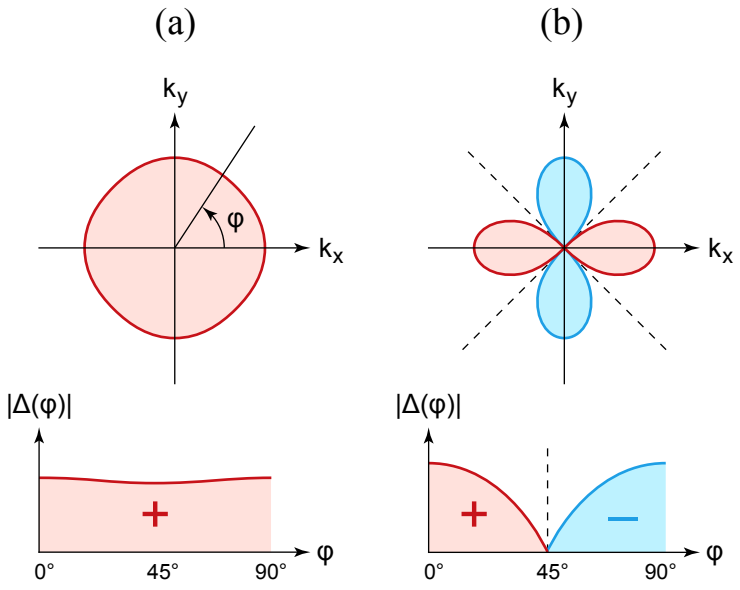

Figure 4.4: Two of the possible symmetries of the pairing energy gap in superconductors. (a) The gap in superconductors with s-wave symmetry does not change sign, although anisotropy may occur due to the lattice symmetry. (b) A superconductor with a d-wave gap has four nodes—lines in momentum space without an energy gap—occurring along the diagonal directions. In both panels, red shading represents a positive gap and blue shading represents a negative gap. However, only the magnitude and relative phase differences are relevant to measurable properties.

Many mechanisms of high-temperature superconductivity have been proposed for the cuprates. Shortly after their discovery, P. W. Anderson proposed his resonating valence bond theory, in which singlet bonds between pairs of copper atoms form a kind of fluctuating quantum spin liquid [77]. When the material is doped, the valence bonds become mobile and condense into a sea of Cooper pairs. Because of the unique magnetic

properties of the cuprates, spin fluctuations are another leading possibility. In this theory, pairing is mediated by magnons rather than phonons. It is often said that there are as many theories of high-T_c as there are theorists working on the problem. Even after a quarter century, cuprate superconductivity is still a subject of vigorous research.

4.2 Electronic structure of the cuprates

The low-energy electronic structure of the cuprates can be described as that of a two-dimensional doped Mott (or, more accurately, charge-transfer) insulator. The undoped parent compounds are half-filled antiferromagnetic insulators exhibiting strong electron–electron correlations, and doping electrons or holes into the CuO_2 plane induces an insulator-to-superconductor transition.

4.2.1 Chemical structure

All of the essential physics of cuprate superconductivity occurs within the two-dimensional CuO_2 planes. With a nominal $+2$ charge, the copper ions take a $3d^9$ configuration with one hole per atom. The in-plane oxygen ions, situated midway between copper neighbors, have fully occupied $2p^6$ shells. The copper $3d$ and oxygen $2p$ orbitals strongly hybridize with each other, but remain relatively uncoupled from the other atoms in the unit cell. This picture has led to a widely held schematic view of the cuprates, shown in Figure 4.5, in which the CuO_2 planes are separated by "charge reservoir" or "blocking" layers: slabs of atoms that dope carriers into the planes but do not otherwise contribute to the low-energy electronic structure. Doping may be achieved via the addition or removal of oxygen atoms or by chemical substitution of cations. In either case,

doping inhomogeneity is introduced in the blocking layers rather than the CuO_2 planes themselves, a relatively "clean" method similar to modulation doping of semiconductors. Typical resistivity anisotropies of the cuprates exceed $\rho_c/\rho_{ab} \sim 10^3$, highlighting the confinement of mobile charge carriers to the two-dimensional CuO_2 planes.

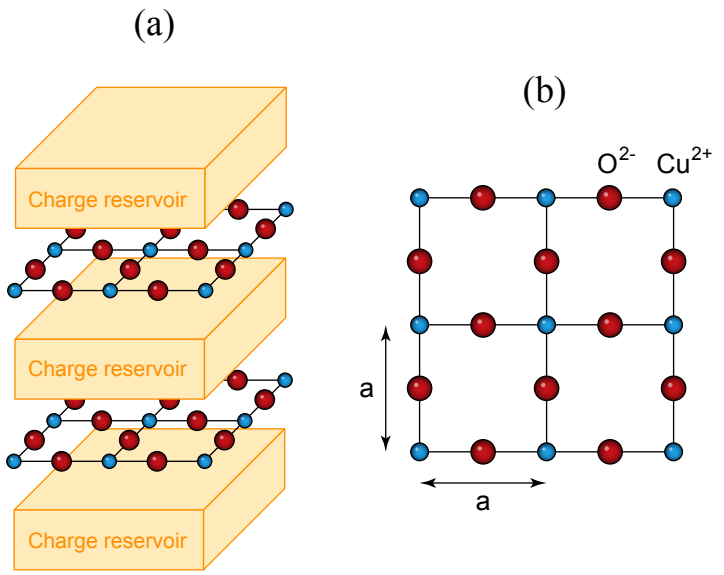

Figure 4.5: Schematic view of the crystal structure of the cuprates. (a) The layered structure of the cuprates. One or more CuO_2 planes are separated by "charge reservoirs" consisting of layers of atoms that dope the CuO_2 planes but are not otherwise involved in the low-energy electronic structure. (b) View of a single CuO_2 plane showing Cu^{2+} ions arranged in a square lattice, pairs of which are separated by a single O^{2-} ion. The Cu-Cu distance is denoted a.

The nominally degenerate $3d^9$ copper orbitals are split due to the electrostatic field of the crystal lattice. An octahedral field will split the ten d orbitals into four e_g and six t_{2g} states. However, in the cuprates the apical oxygens (if they exist) are farther from the copper ions than the in-plane oxygens. This creates a square pyramidal crystal field that breaks the degeneracy of the e_g manifold. This results in the occupation of all $3d$ orbitals except $d_{x^2-y^2}$, which remains half-filled. Figure 4.6 illustrates this crystal field splitting.

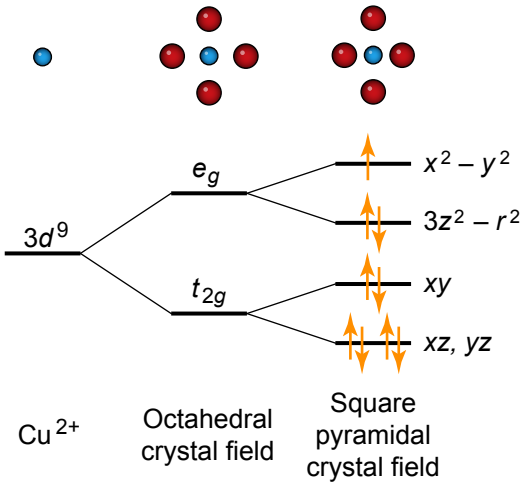

Figure 4.6: Crystal field splitting of copper ions. The nominally degenerate $3d$ copper orbitals first split into an e_g and a t_{2g} manifold because of the field of the neighboring oxygen ions. Asymmetry of the apical oxygens with respect to the in-plane oxygens further splits the states. The net result is a half-filled $d_{x^2-y^2}$ orbital, with all other states fully occupied.

4.2.2 Band structure

Because of their strong overlap, the in-plane copper $3d_{x^2-y^2}$ electrons strongly hybridize with neighboring oxygen $2p_{x,y}$ orbitals, forming three Bloch bands with mixed orbital character: bonding, non-bonding, and antibonding. As Figure 4.7 shows for wavevector (π, π), the bands with lowest energy occur when the phases of the oxygen $2p$ orbital lobes match the phases of neighboring copper $3d$ lobes. In the CuO_2 plane, with one hole per copper site, the bonding and non-bonding states are completely occupied, leaving a half-filled antibonding band.

Because the bonding and non-bonding bands are completely filled and lie at high binding energy, they do not contribute to the low-energy electronic structure of the cuprates. One can then imagine an effective one-band model for the CuO_2 plane. This can be accomplished by invoking the Zhang-Rice singlet wavefunction [78], illustrated

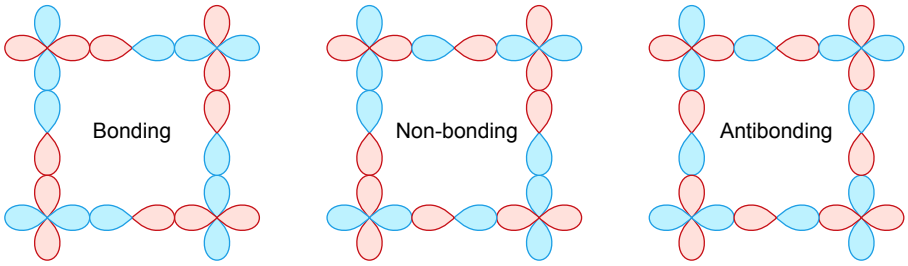

Figure 4.7: Copper–oxygen hybridization in the CuO_2 plane at wavevector (π, π). Bonding, non-bonding, and antibonding combinations can be formed depending on the relative phase of the copper $3d_{x^2-y^2}$ and oxygen $2p_{x,y}$ orbitals. The bonding and non-bonding states are fully occupied and the antibonding state is half-filled.

schematically in Figure 4.8, where a hole in the half-filled CuO_2 plane is delocalized symmetrically and coherently on the four neighboring oxygen ions of a copper atom. These composite states can then hop as a unit from one copper site to the next. The net result is a low-energy one-band square lattice Hamiltonian with an effective hopping amplitude and on-site energy. It should be noted that while this one-band model may be sufficient for describing the general electronic structure of the cuprates, the separate copper and oxygen states cannot be neglected when analyzing certain detailed features. This is especially true when comparing electron- and hole-doped cuprates, as doped holes lie within the Zhang-Rice singlet manifold while doped electrons reside in the copper-derived antibonding band.

Extended Bloch waves may be formed out of the Zhang-Rice singlet states. This can be captured with a simple square lattice tight-binding model that includes nearest-neighbor, next-nearest-neighbor, and sometimes next-next-nearest neighbor hopping (the so-called t-t'-t'' model). For the cuprates, $t \sim 0.3$ eV, but can vary considerably from material to material. Figure 4.9 shows the band dispersion and Fermi surface that arises from the one-band tight-binding model. Common to all cuprates, the Fermi surface is composed of a large hole pocket centered at (π, π), the shape of which is controlled by the parameters t' and t''. The simple tight-binding model presented here does not include electron-electron

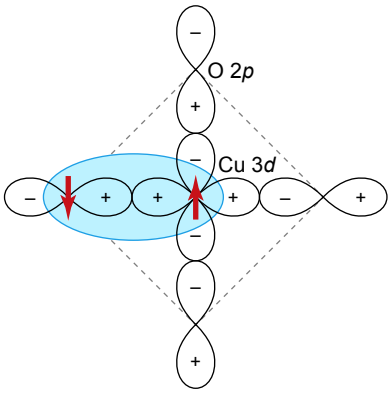

Figure 4.8: Schematic diagram of the Zhang-Rice singlet wavefunction consisting of a single hole spread out symmetrically and coherently over the four neighboring oxygen ions of a copper site. The spin of the oxygen hole and copper hole are correlated and form a singlet, one of which is shown in the figure.

correlations, which drastically change the electronic structure of the cuprates at low dopings. In this regime the tight-binding model is not applicable; correlations give rise an insulating rather than a metallic state.

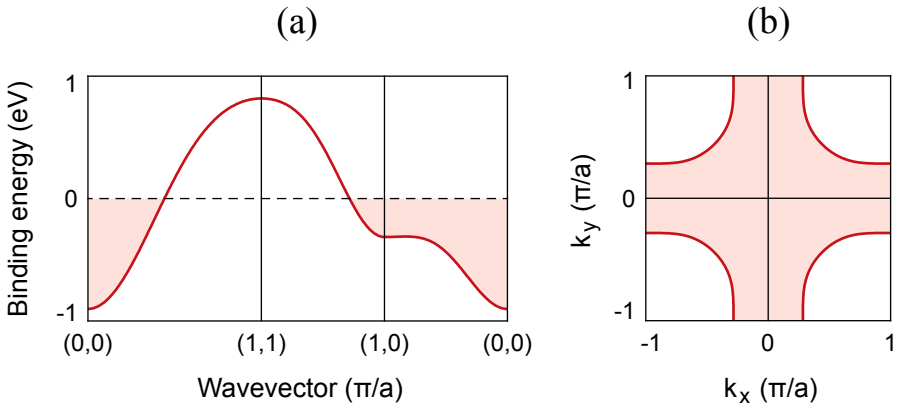

Figure 4.9: Low-energy band structure of the cuprates based on a noninteracting one-band model. (a) Band dispersion of the tight-binding model. In the absence of strong correlations, the band is metallic and crosses the Fermi level. (b) The Fermi surface is composed of a large hole pocket centered at (π, π).

4.2.3 Strong correlations

The one-band model outlined in the previous section predicts that the cuprates are metallic regardless of doping. This is not the case, however, as the undoped parent compounds of the cuprate superconductors are antiferromagnetic insulators. This discrepancy results from the complete neglect of electron-electron correlations in conventional band theory. In 1949, N. F. Mott explained why nickel oxide is insulating even though it contains a half-filled band by proposing that electron-electron Coulomb repulsion forbids double occupancy of nickel ions and thereby inhibits conduction of electrons [79]. This idea was further developed, and today materials expected to be metallic by band theory but are insulating instead due to electron–electron correlations are known as Mott insulators.

In 1963, J. Hubbard proposed a tight-binding Hamiltonian explicitly taking Mott correlations into account [80]. This widely-used model, now known as the Hubbard Hamiltonian, includes a term representing on-site electron-electron repulsion:

$$\mathcal{H} = -t \sum_{\langle i,j \rangle \sigma} \hat{c}^{\dagger}_{i\sigma} \hat{c}_{j\sigma} + U \sum_{i} \hat{n}_{i\uparrow} \hat{n}_{i\downarrow}, \tag{4.13}$$

where t is the nearest-neighbor hopping amplitude, $\langle i, j \rangle$ represents summing over all nearest-neighbors, $\hat{n}_{i\sigma} = \hat{c}^{\dagger}_{i\sigma} \hat{c}_{i\sigma}$ is the particle density operator on site i, and U represents the Coulomb energy required for double occupancy of a site. It is widely believed that the one-band Hubbard model with $U \sim t$ captures the essential physics of high-temperature superconductivity in the cuprates [20,77]. The Hubbard model not only explains why the undoped cuprates are insulating, but also why they are antiferromagnetic. When nearest-neighbor spins are antiparallel, virtual hopping to neighboring sites and back can lower the kinetic energy. This is not possible with parallel spins, as the Pauli exclusion principle forbids such a virtual process. For large U, double occupancy is completely suppressed and an effective spin model called the t-J model results.

The interaction term in the Hubbard Hamiltonian for the cuprates results in the antibonding conduction band being split into so-called lower and upper Hubbard bands, with an energy gap of size U (a few eV) separating them. This picture is illustrated in Figure 4.10(b). However, J. Zaanan, G. A. Sawatzky, and J. W. Allen have famously pointed out that in transition metal compounds, the charge transfer energy Δ describing the transfer of holes from copper to oxygen ligands ($d_i^8 p_i^6 \rightarrow d_i^9 p_i^5$) is smaller than the Hubbard splitting U describing the transfer of holes from copper to copper ($d_i^8 d_j^9 \rightarrow d_i^9 d_j^8$) [81]. As a result, the undoped cuprate are considered "charge-transfer insulators" because the insulating gap in reality exists between the antibonding-derived upper Hubbard band and the Zhang-Rice singlet band, as shown in Figure 4.10(d).

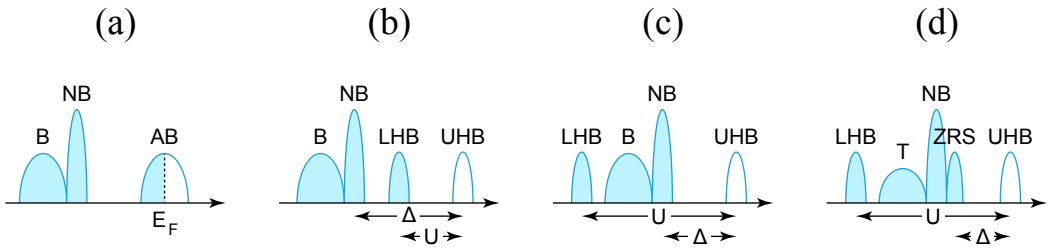

Figure 4.10: Schematic diagram of the density of states (vertical axis) of the cuprates at increasing levels of detail. (a) In the noninteracting case, the bonding (B) and non-bonding (NB) bands are full and the antibonding (AB) band is half-filled, resulting in a metallic system. (b) When Mott-Hubbard correlations are considered, the antibonding band is split into a lower Hubbard band (LHB) and an upper Hubbard band (UHB), resulting in an insulating state. (c) In transition metal compounds like the cuprates, the Hubbard splitting U is larger than the charge-transfer gap Δ. (d) Further hybridization causes the Zhang-Rice singlet (ZRS) and triplet (T) bands to form.

Although much theoretical work has gone into understanding the half-filled Mott state, the most interesting features of the cuprates—high-temperature superconductivity and associated phenomena—only occur when the antiferromagnetic insulating state is destroyed by doping. Long-range Néel order is strongly perturbed by mobile carriers, and a different ground state (such as a quantum spin liquid or the resonating valence bond state) may yield a better description of high-T_c superconductivity. Furthermore, the

BCS theory, developed for weakly-interacting Fermi liquids, cannot possibly describe the microscopic mechanism of cuprate superconductivity; it is becoming clear that a proper description will need to include the competition (or cooperation!) between antiferromagnetism and electron pairing. Even after twenty years of work, the strong correlations in cuprate superconductors present a profound challenge to physicists.

4.2.4 The cuprate phase diagram

As we have shown, the cuprates are often treated within the paradigm of doped Mott insulators, where they are separated into two categories: hole-doped (p-type) and electron-doped (n-type). The first cuprates to be discovered were hole-doped, and the highest transition temperatures are achieved with hole-doping. For these reasons, the research community has focused heavily on studying this subgroup of the cuprates. In 1989, Y. Tokura, H. Takagi, and S. Uchida discovered the first electron-doped cuprate family, $Re_{2-x}Ce_xCuO_4$ (with $T_c = 24$ K for *Re* = Nd) [82]. $Re_{2-x}Ce_xCuO_4$, crystallizing in the so-called T' structure, remains the only well-studied electron-doped family, with only a single other—the infinite-layer cuprates—discovered since then.

Within the Hubbard model in Equation 4.13, a rigorous symmetry between p-type and n-type doping exists. When next-nearest-neighbor hopping or when multi-band physics is included, however, that symmetry is broken. As shown in Figure 4.11, the actual doping–temperature phase diagram of the cuprate superconductors shows substantial asymmetry. This is especially true for the low-doping antiferromagnetic insulating phase, which appears to be much more robust and extends to much higher dopings on the electron-doped side. In some cases, it may even coexist with superconductivity. For the hole-doped cuprates, on the other hand, antiferromagnetism is rapidly suppressed

by ∼3% doping, far below the onset of superconductivity. Because the antiferromagnetic phase is so essential to the phenomenology of the cuprate material family, this asymmetry has important ramifications for the mechanism of high-temperature superconductivity.

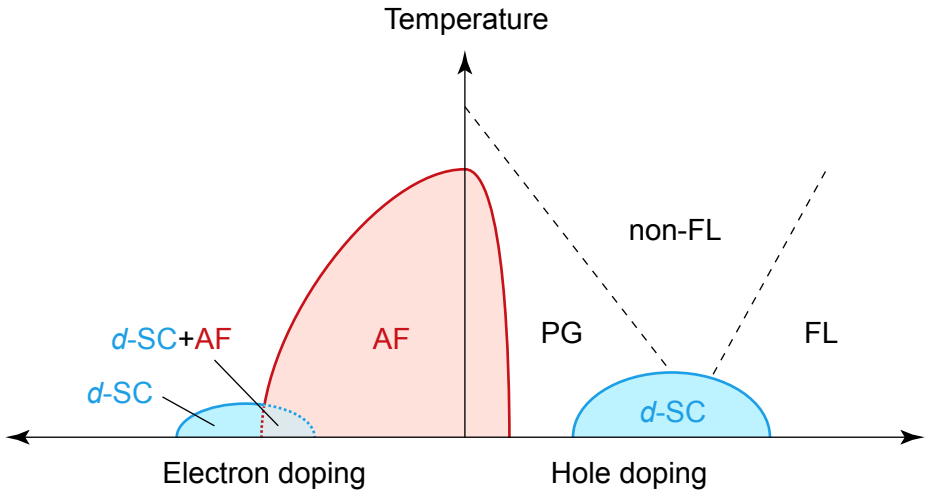

Figure 4.11: Doping–temperature phase diagram of the cuprate superconductors, showing the asymmetry between hole- and electron-doping. The antiferromagnetic (AF) phase is much more robust for n-type cuprates, and may even coexist with d-wave superconductivity (d-SC). Because the hole-doped cuprates are heavily studied, that half of the phase diagram is much more detailed and includes the poorly-understood pseudogap (PG) and non-Fermi liquid (non-FL) phases.

An intuitive understanding of the doping asymmetry of the antiferromagnetic phase can be achieved by considering how the doped carriers modify the Néel-ordered parent spin system [83]. In the case of electron doping, extra carriers reside on copper sites, resulting in spinless $3d^{10}$ ions that merely dilute the spin system. This leads to a gradual reduction in the Néel temperature as the dilution factor grows larger [84]. On the other hand, in the case of hole doping, carriers lie on oxygen orbitals. The coupling of copper spins to these carriers, whether ferromagnetic or antiferromagnetic, will induce a net ferromagnetic interaction between neighboring copper spins, strongly frustrating the antiferromagnetic background order [85]. The Néel temperature subsequently drops much more rapidly with hole doping.

In addition to the fundamental differences observed in the magnetic properties of hole-doped and electron-doped cuprates, transport properties also exhibit qualitatively different behaviors. For example, within the normal state at optimal doping, the in-plane resistivity shows a linear temperature dependence for hole-doped cuprates [86, 87] but a quadratic T^2 dependence in the electron-doped case [88]. A comprehensive understanding of high-temperature superconductivity will require an explanation of the observed doping asymmetry of the cuprates, which has been hindered by a lack of n-type material families. This dissertation seeks to remedy this experimental situation by revealing the detailed electronic structure of the infinite-layer electron-doped cuprate $Sr_{1-x}La_xCuO_2$ for the first time.

CHAPTER 5

THE INFINITE-LAYER CUPRATE FAMILY

Among the multitude of known cuprate material families and associated structures, the archetype is "infinite-layer" $ACuO_2$, where perfectly square and flat CuO_2 planes are separated by layers of alkaline earth atoms such as Ba, Ca, and Sr. Discovered in 1988 [89], $ACuO_2$ is the second and only other known electron-doped cuprate family. The infinite-layer structure is free of magnetic rare-earth ions, oxygen chains, orthorhombic distortions, incommensurate superstructures, ordered vacancies, and other complications that abound among the other cuprate material families. Furthermore, it is the only cuprate that can be made superconducting by both electron doping ($T_{c,\max} = 43$ K) [90] and hole doping ($T_{c,\max} = 110$ K) [91], making it a potential platform for decoding the complex many-body interactions responsible for high-T_c superconductivity in the cuprates.

5.1 Crystal structure

The infinite-layer cuprates have the simplest possible crystallographic structure: single CuO_2 planes separated only by alkaline earth atoms. Figure 5.1 shows the unit cell of $ACuO_2$. The structure is unique among the cuprates because the c-axis Cu-Cu distance is less than the in-plane value. There are no apical oxygen ligands, however, and this ensures a two-dimensional band dispersion by inhibiting electron hopping along the c-axis. The crystal structures of both known electron-doped cuprate families, $Re_{2-x}Ce_xCuO_4$ and $ACuO_2$, lack apical oxygens. This fact is supported by consideration of the electrostatic repulsion between doped electrons and apical oxygen ions in CuO_5 pyramids and CuO_6 octahedra, which discourages electron doping [92]. It is uncertain, however, if the absence of apical oxygens is a *necessary* condition for electron doping of cuprates.

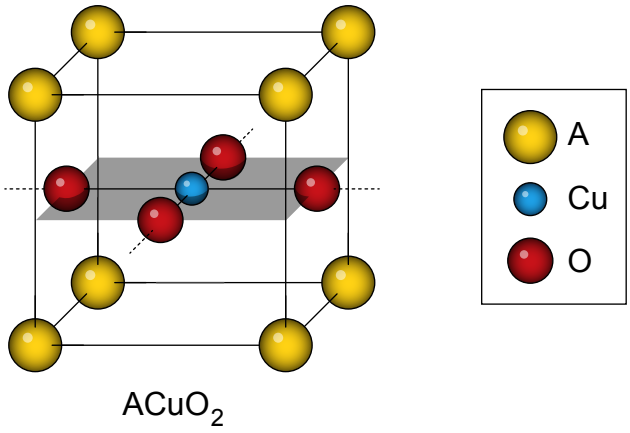

Figure 5.1: The unit cell of $ACuO_2$. The CuO_2 plane is highlighted in gray. Unlike the various hole-doped cuprate structures, apical oxygens are not present in the infinite-layer structure.

5.1.1 Doping methods

Chemical doping of electrons in $ACuO_2$ is achieved via heterovalent substitution at the alkaline earth site. For example, in $Sr_{1-x}La_xCuO_2$, each lanthanum atom donates one electron to the CuO_2 plane, resulting in x extra electrons per copper atom. This method minimizes the effects of doping inhomogeneity because the dopant disorder lies within the inactive blocking layers between planes. The mechanism of doping in the hole-doped infinite-layer materials is not yet known. The original paper presenting the discovery of p-type superconductivity in an infinite-layer material suggested that A-site deficiency plays a role [91], but many researchers now believe that excess oxygen atoms are the relevant operators, possibly forming oxygen-rich impurity layers that capture electrons [93–98]. In analogy with the electron-doping method, hole-doping of $ACuO_2$ has been attempted by substitution of monovalent sodium for calcium ($Ca_{1-x}Na_xCuO_2$), but no superconductivity was observed [99].

5.2 Synthesis

Research on the infinite-layer cuprates has been severely hindered by the inability to synthesize bulk single crystals. This is due to the fact that bulk growth of $ACuO_2$ requires high pressures, preventing the formation of large single crystals; only polycrystalline bulk samples have been grown to date. Fortunately, recent progress in growth techniques has led to high-quality superconducting thin films grown by sputtering, MBE, and pulsed-laser deposition.

5.2.1 Oxygen reduction

In spite of its structural simplicity, the infinite-layer cuprate is quite sensitive to growth conditions. Like the $Re_{2-x}Ce_xCuO_4$ family, synthesis of the electron-doped infinite-layer cuprates requires an oxygen-reduction step after growth in order to induce superconductivity. This step is carried out with a high-temperature anneal in a reducing atmosphere—often vacuum—and is universally required for superconductivity in the n-type cuprates, both for bulk and film samples.

It is widely believed that the reduction step removes a small amount of excess oxygen atoms present in the as-grown materials at the apical sites [96,100–104], although there are many alternative theories involving oxygen deficiency within the CuO_2 planes [105–108]. Neutron diffraction studies have shown that in properly reduced samples, neither interstitial oxygen nor vacancies play a significant role in the doping of $Sr_{0.90}La_{0.10}CuO_2$ [109]. The amount of excess oxygen removed during the reduction step is minuscule, estimated to be less than $\sim$1% in optimally-doped $Nd_{2-x}Ce_xCuO_4$ based on neutron diffraction and Mössbauer studies [101,110,111]. Somewhat suprisingly, the amount of oxygen removed

in the annealing step is inversely proportional to doping, with a removal rate as high as $\sim$7% for undoped Nd_2CuO_4 [101, 112].

The mechanism by which the presence of a relatively small amount of excess oxygen is able to completely suppress superconductivity is not presently known. There is some evidence that oxygen-induced disorder can stabilize antiferromagnetic correlations in the cuprates [84, 113], which would allow the antiferromagnetic phase to win out over the competing superconducting phase. ARPES experiments on $Re_{2-x}Ce_xCuO_4$ do not detect any change in the band filling or the band parameters through the oxygen reduction step. The main electronic effect of the annealing, instead, is the removal of a momentum-dependent leading-edge gap around the nodal region of the Fermi surface [102, 114]. A decrease in the quasiparticle scattering rate is also observed through the oxygen reduction step, likely due to a decrease in disorder and impurity scattering. This picture can explain why the oxygen reduction step has such a large effect on transport properties and optical responses. Although still an open issue, the general consensus is that the interplay between antiferromagnetic and superconducting orders plays a large role in the oxygen reduction puzzle.

5.2.2 Bulk growth

The infinite-layer structure was first discovered in micron-sized single-crystal samples synthesized by conventional crystal growth methods [89]. Prepared at ambient pressure, $ACuO_2$ is orthorhombic, containing edge-sharing square-planar CuO_2 chains [115]. Superconducting samples with a tetragonal structure were not discovered until a method of high pressure sintering was developed [116]. In this technique, pressures in the range 3 to 6 GPa are achieved using belt or cubic anvil presses, as illustrated in Figure 5.2. Samples

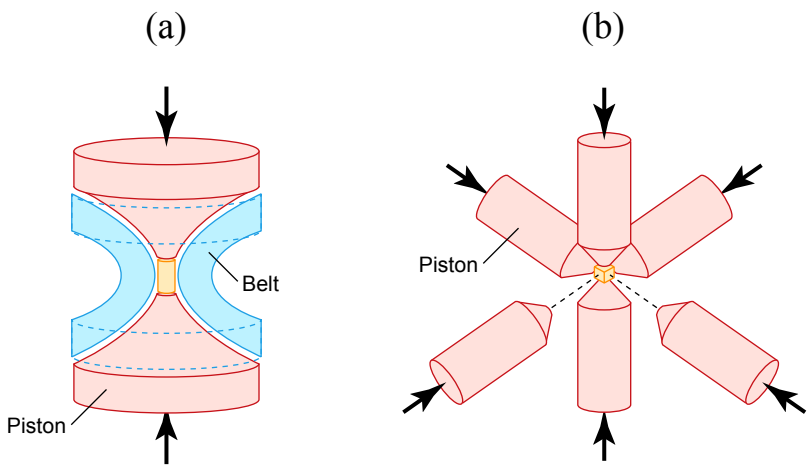

Figure 5.2: Apparatus used for high pressure growth of $ACuO_2$. Applied pressure is represented by black arrows. (a) A belt press. Two pistons compress the starting material, which is situated in the middle of a high-strength hollow cylindrical "belt." (b) A cubic anvil press. Pistons compress the starting material along six opposing directions corresponding to the sides of a cube.

grown this way are inherently polycrystalline and of relatively low structural quality, but show superconducting transitions in the range 40 to 110 K depending on the choice of alkaline earth atoms [90, 91, 117, 118]. Table 5.1 lists some of the samples studied early in the development of bulk growth methods.

Table 5.1: Early bulk $ACuO_2$ samples

Material	T_c **(K)**	**Year**
$(Ca_{0.86}Sr_{0.14})CuO_2$	—	1988 [89]
$SrCuO_2$	—	1989 [116]
$Sr_{0.8}Ba_xCuO_2$	60, 90	1991 [117]
$Sr_{1-x}Nd_xCuO_2$	40	1991 [90]
$Sr_{1-x}La_xCuO_2$	43	1991 [118]
$(Sr_{1-x}Ca_x)_{1-y}CuO_2$	110	1992 [91]

5.2.3 Film growth

Soon after the discovery of the infinite-layer cuprates, thin film samples were grown by radio frequency sputtering [119] and pulsed-laser deposition (PLD) [120–122]. The first superconducting films, grown by sputtering, were reported in 1992 [123], but their transition temperatures were substantially less than comparable bulk samples. The development of better oxide film growth techniques in the following years led to high-quality superconducting thin films grown by sputtering [104, 124, 125], MBE [126–128], and PLD [129, 130]. Crucial to the later successes was relieving the $\sim$1% compressive epitaxial strain of $SrTiO_3$ substrates by using better lattice-matched substrates, such as $KTaO_3$ and $DyScO_3$. Table 5.2 lists some early infinite-layer thin film samples.

Table 5.2: Early thin film $ACuO_2$ samples

Material	T_c **(K)**	**Method**	**Substrate**	**Year**
$CaCuO_2$	—	Sputtering	MgO (100)	1990 [119]
$(Ca_{0.86}Sr_{0.14})CuO_2$	—	PLD	$SrTiO_3$ (100)	1991 [120]
$SrCuO_2$	—	PLD	$SrTiO_3$ (100)	1992 [121]
$Sr_{0.88}Nd_{0.12}CuO_{2-y}$	16	Sputtering	$SrTiO_3$ (100)	1992 [123]
$Sr_{1-x}La_xCuO_2$	39	MBE	$KTaO_3$ (100)	2001 [126]
$Sr_{1-x}La_xCuO_2$	41	MBE	$DyScO_3$ (110)	2004 [127]

A major benefit of growing $ACuO_2$ in thin film form is epitaxial stabilization of the metastable infinite-layer structure, which avoids the need for high pressure synthesis. Clean surface terminations are polar because the atomic layers in the unit cell are charged, alternating in sign between $+2$ (Sr^{2+}) and -2 (CuO_2^{2-}) per unit cell. Polar terminations are expected to be unstable in the presence of an oxidizing gas, and growth of films may proceed cell-by-cell rather than layer-by-layer in order to preserve net charge neutrality [96]. Furthermore, density functional theory predicts that films with total thickness less than five unit cells are unstable toward the formation of a chain-type structure, which relaxes the polar instability [131]. This prediction of a thickness-controlled structural reconstruc-

tion agrees with RHEED oscillations during growth, where diffraction intensities vary widely during the deposition of the first four unit cells. Chapter 8 discusses the polar nature of $Sr_{1-x}La_xCuO_2$ in more depth.

The choice of substrate is important when growing infinite-layer thin films. Films under tensile strain are in general of better quality than compressively strained films, exhibiting lower resistivities and higher superconducting transition temperatures. This is thought to occur because tensile strain allows for easier removal of interstitial oxygen atoms. However, excess tensile strain leads to lattice defects and substrate interdiffusion, reducing the quality of the films [127]. It appears that the best substrate for the growth of superconducting $Sr_{1-x}La_xCuO_2$ is $DyScO_3$, which produces tensily strained films at low dopings and approximately unstrained films at optimal doping ($x \approx 0.10$). Other popular alternatives are $SrTiO_3$, leading to compressively strained films of low quality, and $KTaO_3$ or $GdScO_3$, leading to tensily strained films of moderate quality.

There appears to be a solubility limit for lanthanum in $Sr_{1-x}La_xCuO_2$. When growing films with $x > 0.10$, a so-called "long c-axis" impurity phase develops with ordered oxygen vacancies in the CuO_2 layers [104,126,132]. The maximum superconducting transition temperature of $Sr_{1-x}La_xCuO_2$ (43 K) therefore occurs at $x \approx 0.10$. One can imagine possibly pushing the transition temperature higher by preventing the formation of the impurity phase, but there has been little success in accomplishing this to date.

RHEED

During MBE calibration of $ACuO_2$, the alkaline earth and copper shutter opening times are calibrated by monitoring RHEED oscillations during growth. As Figure 5.3 shows, stable oscillations occur when the A/Cu flux ratio is close to one. The *absolute* fluxes of the

elements, however, cannot be determined in this way. Instead, x-ray diffraction must be used to measure the c-axis lattice constant and total thickness of a calibration film. From this information, the total number of unit cells in the calibration film can be determined. Comparison with the number of shuttering periods during the growth can be used to scale the alkaline earth and copper fluxes in order to obtain complete monolayers. Doping of the A-site is accomplished by simultaneously opening the alkaline earth and dopant source shutters. The dopant flux is calibrated using a QCM.

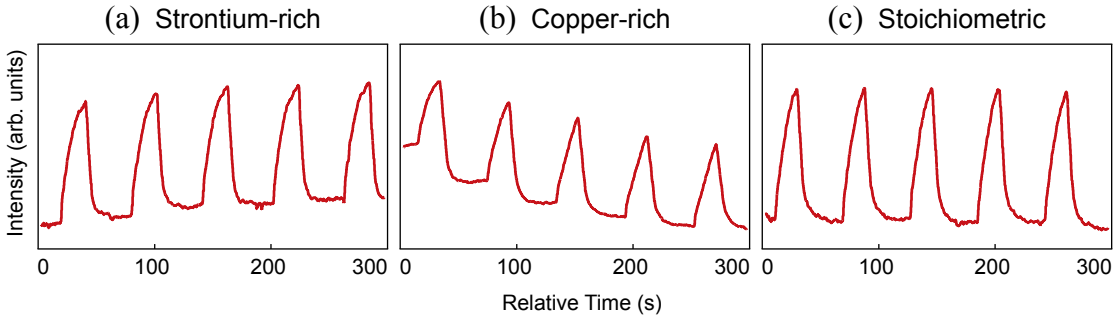

Figure 5.3: Time dependence of the (01) diffraction rod intensity during the calibration of a $SrCuO_2$ epitaxial thin film (a) in the case of a strontium-rich flux, (b) in the case of a copper-rich flux, and (c) with the Sr/Cu flux ratio close to one. The RHEED intensity drifts upward if the strontium flux is too large, downward if the copper flux is too large, and is stable if the flux ratio is close to stoichiometric.

When monitoring RHEED reflections during the growth of $ACuO_2$, an incommensurate streak between the (01) and (02) diffraction rods is observed upon the deposition of copper atomic layers, disappearing during the deposition of the following strontium layers [96,128,133]. As Figure 5.4 shows, the streak is present at the end of growth but disappears during the oxygen reduction step (anneal in vacuum). The presence of the streak during growth and subsequent disappearance upon annealing usually suggests that the film has good structural quality. At present, the origin of the incommensurate streak is not clear, but it may be associated with a loosely-bound copper-rich overlayer [129]. However, the strong influence of the vacuum annealing step on the incommensurate streak

suggests that oxygen also plays a role in its existence. An identical anneal in ozone does not result in the disappearance of the streak.

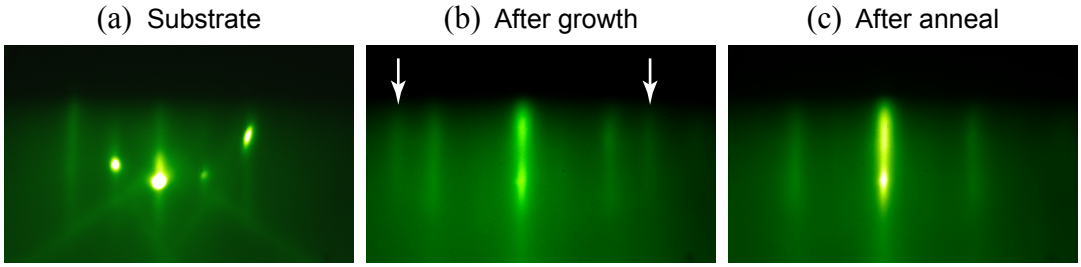

Figure 5.4: RHEED patterns during the MBE growth of a $Sr_{0.90}La_{0.10}CuO_2$ epitaxial thin film on (110) $GdScO_3$. RHEED is viewed along the pseudocubic [100] direction (a) before growth, (b) after growth, and (c) after the oxygen reduction step. The presence of the incommensurate streaks in panel (b), which vanish during the vacuum annealing step, are marked by white arrows.

Superlattices

The first infinite-layer superlattice, a $SrCuO_2/BaCuO_2$ film showing semiconducting behavior down to 7 K, was grown by PLD in 1991 [134]. As the thin film growth technique was developed, more researchers began investigating infinite-layer superlattices. These heterostructures consist of stacked sequences of $SrCuO_2$ or $CaCuO_2$ with $BaCuO_2$. For example, the first superconducting infinite-layer superlattice was $CaCuO_2/(BaCuO_2)_3$, showing zero resistance at 38 K [135]. Soon thereafter, superconductivity at 50 K was observed in $(SrCuO_2)_2/(BaCuO_2)_2$ superlattices [136]. A plausible mechanism of doping in these materials relies on the charge-uncompensated $BaCuO_2$ slabs, which contain excess oxygen atoms at apical sites and act as charge reservoir layers, doping holes into the CuO_2 planes of the other slabs [137]. Strong support for this picture comes from Raman spectroscopy [138] and extended x-ray absorption fine structure measurements [139], which show evidence of apical oxygens in the barium planes.

5.3 Properties

Because of the unavailability of large single crystals, the infinite-layer cuprates have not been investigated with the same depth as their more popular counterparts. Most studies have focused on the material $Sr_{1-x}La_xCuO_2$, usually in polycrystalline form. Experimental techniques that have been employed include transport [124, 128, 140–146], ^{63}Cu nuclear magnetic resonance [141, 147, 148], x-ray absorption near-edge spectroscopy [92, 149], core level x-ray photoelectron spectroscopy [150, 151], point-contact tunneling spectroscopy [152, 153], magnetic and nonmagnetic impurity substitution [154, 155], magnetization [156–160], muon spin rotation [161–163], and small-angle neutron scattering [164]. Some general conclusions from these studies include: confirmation that $Sr_{1-x}La_xCuO_2$ is electron-doped, evidence that strong electron correlations, similar to those seen in the hole-doped cuprates, play a large role in the electronic structure, a small O $2p \rightarrow$ Cu $3d$ charge transfer energy Δ, and lack of evidence for a pseudogap phase.

From these studies, conflicting conclusions have emerged regarding the nature of superconductivity and antiferromagnetism in $Sr_{1-x}La_xCuO_2$. Thermopower measurements indicate that electron–phonon interactions play an important role in Cooper pairing [140], an anomalously small density of states has been detected at the Fermi energy by nuclear magnetic resonance [141], angle-dependent magnetization results suggest strongly three-dimensional superconductivity [144, 156, 157] and enhanced quantum fluctuations possibly due to a competing spin density wave [157], zero-field muon spin rotation has reported both the absence of antiferromagnetic order [161] and phase separation into magnetic and superconducting domains [162], and electric field effect measurements have shown that superconductivity is dominated by electron-like rather than hole-like carriers [145].

The electron-doped infinite-layer cuprates share many material properties with the $Re_{2-x}Ce_xCuO_4$ family. In contrast with the hole-doped cuprates, which exhibit a linear T power law in resistivity over a wide temperature range in the normal state [86, 87], the electron-doped materials display a Fermi liquid T^2 power law indicative of conventional electron–electron scattering [83, 88]. A study of infinite-layer $Sr_{1-x}La_xCuO_2$, however, shows deviations from quadratic scaling above and below optimal doping. Underdoped samples ($x = 0.08$) displayed a $T^{1.78}$ power dependence and overdoped samples ($x = 0.13$) a $T^{1.39}$ dependence [128]. This behavior is thought to be caused by complex transport mechanisms beyond simple electron–electron scattering [165].

Perhaps most confounding, however, are reports of nodeless or s-wave superconductivity in $Sr_{1-x}La_xCuO_2$, in marked contrast to the d-wave pairing observed in the hole-doped cuprates and the $Re_{2-x}Ce_xCuO_4$ family. These findings come from a wide variety of probes: the lack of momentum dependence and zero-bias conductance peaks in tunneling spectroscopy [152], insensitivity to nonmagnetic impurities [154], the temperature and field dependence of specific heat [143], and the local field distribution from small-angle neutron scattering [164] and muon spin rotation [163]. Other studies, however, support an unconventional superconducting order parameter [141,147,153,160–162], and a recent phase-sensitive measurement favors a d-wave symmetry [166].

Because of the numerous conflicting results regarding the electronic structure of the infinite-layer cuprates, it is difficult to ascertain whether d-wave superconductivity and strong antiferromagnetic order are generic to the electron-doped CuO_2 plane. This dissertation resolves these long-standing questions by revealing, for the first time, the detailed electronic structure of infinite-layer $Sr_{1-x}La_xCuO_2$, a completely independent electron-doped cuprate. Our observations demonstrate a clear coexistence of superconductivity with robust antiferromagnetic order and offer an explanation for previous reports of a

nodeless superconducting gap while retaining a conventional cuprate d-wave superconducting order parameter. We confirm that the cuprate phase diagram is fundamentally asymmetric and provide a coherent framework for understanding the generic properties of all electron-doped cuprates.

CHAPTER 6

THE ELECTRONIC STRUCTURE OF $Sr_{0.90}La_{0.10}CuO_2$

In $Re_{2-x}Ce_xCuO_4$, the only well-studied n-type cuprate family, robust antiferromagnetism can persist up to a doping of $x = 0.14$ and may possibly even coexist with superconductivity [167,168]. In contrast, in all hole-doped cuprates, Néel order is rapidly suppressed by $x \approx 0.03$, with d-wave superconductivity following at higher doping levels. Studies of the $Re_{2-x}Ce_xCuO_4$ family by ARPES have shown signatures of a strong coupling to (π, π) antiferromagnetism. However, ARPES studies on hole-doped cuprate families often yield material-specific features that are idiosyncratic to particular compounds, such as the superconducting coherence peak in $Bi_2Sr_2CaCu_2O_{8+\delta}$ [169] or the chemical potential pinning in $La_{2-x}Sr_xCuO_4$ [170]. Moreover, the origin of the robust antiferromagnetism in $Re_{2-x}Ce_xCuO_4$ is complicated by rare-earth magnetism, which is known to couple to the CuO_2 plane and modify long-range magnetic order [83]. Recent state-of-the-art calculations based on dynamical mean-field theory suggest that the electron-hole asymmetry is indeed intrinsic to the cuprate phase diagram and may arise from the nature of the upper Hubbard band or the lack of apical oxygens [171,172].

From an experimental standpoint, investigating a different n-type cuprate is essential in order to definitively determine whether the strong antiferromagnetism observed in the $Re_{2-x}Ce_xCuO_4$ family is truly intrinsic to the electron-doped CuO_2 plane. The infinite-layer compound $Sr_{1-x}La_xCuO_2$ is an ideal candidate, with T_c = 43 K, the highest of all electron-doped cuprates. This chapter, based on Reference [173], presents the general electronic structure of MBE-grown $Sr_{0.90}La_{0.10}CuO_2$ thin films as observed by ARPES. The experimental results reveal a strong coupling between electrons and (π, π) antiferromagnetism that induces a Fermi surface reconstruction pushing the nodal states below the Fermi level. This removes the hole pocket near $(\pi/2, \pi/2)$, realizing nodeless super-

conductivity without requiring a change in the symmetry of the order parameter. These findings provide an explanation for the many puzzling reports of nodeless or s-wave superconductivity in $Sr_{1-x}La_xCuO_2$, verifies that robust antiferromagnetism is intrinsic to the n-type cuprate materials, and contributes to a universal understanding of all electron-doped cuprates.

6.1 Methods

The following section briefly describes the growth, measurement, and characterization of $Sr_{0.90}La_{0.10}CuO_2$ thin films. More detailed information concerning the growth and characterization can be found in Reference [128] and the supplemental material of Reference [173], respectively.

6.1.1 Film growth

The growth of superconducting $Sr_{1-x}La_xCuO_2$ thin films via layer-by-layer MBE is outlined in Reference [128]. CuO_2-terminated films of thickness 60 unit cells ($\sim$20 nm) were grown epitaxially on (110) $GdScO_3$ substrates, which have a distorted perovskite structure with a pseudocubic lattice constant of 3.968 Å [174], using a Veeco GEN10 dual-chamber oxide MBE system. Shuttered layer-by-layer deposition was performed in a background of 100% distilled O_3 at a pressure of 1×10^{-6} Torr and with a substrate temperature of 510 °C. Depositions were monitored using reflection high-energy electron diffraction. As outlined in Section 5.2.3, the strontium and copper shutter opening times were calibrated by monitoring RHEED oscillations during the growth of undoped $SrCuO_2$ films. The RHEED patterns were taken with a glancing electron beam parallel to the in-plane pseudocubic [100] direction of the substrate. After growth, samples were oxygen-reduced by

vacuum annealing at 520 °C for 30 minutes in order to eliminate any apical oxygen atoms. Samples were then cooled to 200 °C before immediate transfer under ultra-high vacuum to the ARPES chamber (<5 minutes at 2×10^{-10} Torr). All superconducting samples had a nominal lanthanum doping of $x = 0.10 \pm 0.01$, a measured doping of $x = 0.10 \pm 0.03$, and a measured $T_c = 25 \pm 5$ K.

6.1.2 ARPES measurements

ARPES measurements were performed with a VG Scienta R4000 electron spectrometer (cf. Section 2.3.4) and He-Iα photons at 21.2 eV (cf. Section 2.3.3). The base pressure of the vacuum chamber was 7×10^{-11} Torr, allowing a single sample to be measured for many days without any detectable sample degradation. Typical instrumental resolutions are ΔE = 10 meV and Δk = 0.03 Å^{-1} for the Fermi surface map, and ΔE = 6 meV for the superconducting gap measurements. E_{F} was determined by measuring polycrystalline gold in electrical contact with the sample (cf. Section 2.4.2).

Background subtraction

Spectra from all films showed a momentum-independent background present throughout the entire Brillouin zone. This background, typical of the cuprates, is thought to arise from elastic scattering of photoelectrons escaping from the surface [175]. Where mentioned below, this background has been subtracted from the spectra in order to emphasize and enhance the intrinsic features of $Sr_{1-x}La_xCuO_2$. Figure 6.1 describes the background subtraction process. By averaging ∼500 individual EDCs around the Brillouin zone in regions where low energy bands are absent, a "global" background EDC is generated (black curves in Figure 6.1). For each acquired spectrum, this EDC is scaled in order to

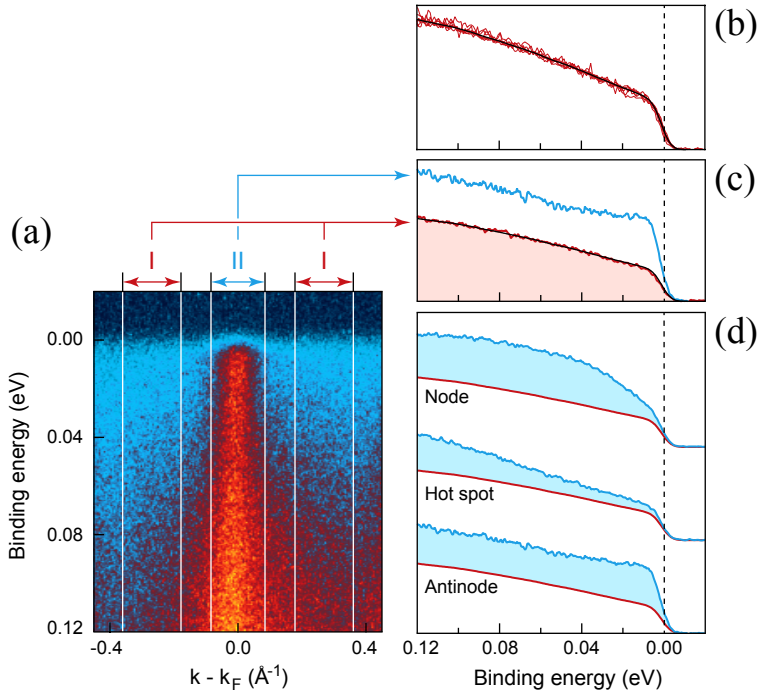

Figure 6.1: Illustration of the momentum-independent background subtraction process. (a) Spectrum showing a cut through the antinode. Two momentum regions are isolated from the full spectrum: region I (containing the background signal on both sides of the band crossing) and region II (containing the band itself along with the underlying background). (b) Background EDCs generated from the node, antinode, and hot spot scans (red curves) along with their smoothed average (black curve). The background is identical in different regions of momentum space. (c) EDCs averaged over the two regions shown in panel (a). The global background EDC is shown by the black curve and is shaded red. (d) EDCs for the node, hot spot, and antinode without background subtraction (blue curves). The global background EDC is also shown for each (red curves). Curves are offset for clarity. The blue shaded regions represent the intrinsic spectral function after background subtraction, as presented in the remainder of the text.

match the integrated intensity in region I, close to the low-energy states (region II). This scaling takes into account variations in the intensity from scan to scan as well as gradual modulations in the intensity of the background. A different background is generated for each temperature because of the broadening of the Fermi edge. After smoothing, the momentum-independent, uniform background is subtracted from EDCs wherever necessary. We emphasize that the conclusions drawn below about the superconducting gap and antiferromagnetism are robust, regardless of the presence of the background.

6.1.3 Sample characterization

In order to verify the quality and composition of the measured $Sr_{0.90}La_{0.10}CuO_2$ films, a number of characterizations were performed on the samples. Immediately after ARPES measurements, *in situ* low-energy electron diffraction was performed on the films in order to examine their surface structure. In addition, after removal from the vacuum chamber, resistivity, x-ray diffraction, x-ray photoelectron spectroscopy, and x-ray absorption spectroscopy were performed. Summaries of the results of these characterizations are given below.

Low-energy electron diffraction

Low-energy electron diffraction (LEED), performed *in situ* immediately after ARPES measurements, was used to examine the surface structure and quality of the $Sr_{0.90}La_{0.10}CuO_2$ films before exposure to air. As Figure 6.2 illustrates, LEED patterns of all $x = 0.10$ films measured by ARPES show perfectly square atomic planes with no evidence of reconstruction at the surface, preserving the simple infinite-layer structure (but see Figure 6.2 and Chapter 8 below for evidence of a reconstruction in films at lower doping levels). This is fortunate because many nominally tetragonal transition metal oxides, such as Sr_2RuO_4 [176] or $SrTiO_3$ [177], are known to support orthorhombic reconstructions at their surfaces because of their complex surface chemistry, which complicate the momentum dependence of ARPES spectra.

Interestingly, as Figure 6.2(b) shows, some $Sr_{1-x}La_xCuO_2$ samples show an anomalous LEED pattern consisting of a quadrupling of the density of reciprocal space points. This is consistent with a doubling of the crystal unit cell in both **a** and **b** lattice directions. Chapter 8 below discusses in depth the origin of this reconstruction, which likely forms

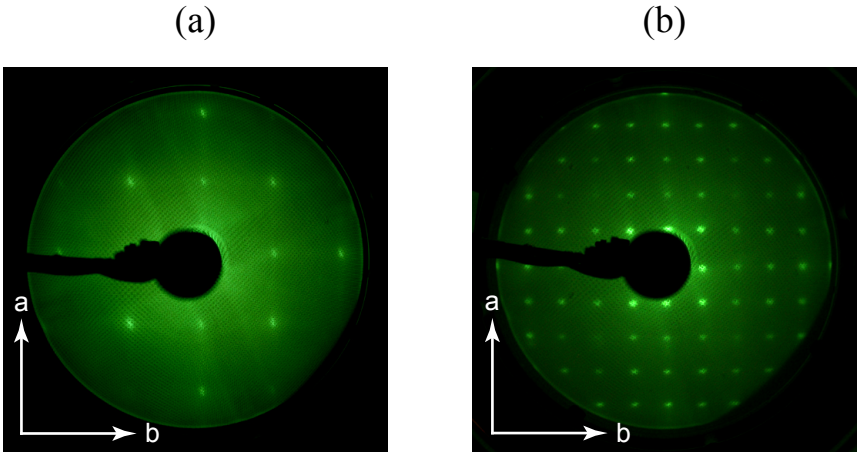

Figure 6.2: Low-energy electron diffraction of $Sr_{1-x}La_xCuO_2$ films using 100 eV electrons. (a) A typical LEED pattern of a $Sr_{0.90}La_{0.10}CuO_2$ thin film, showing a perfectly square atomic surface with no evidence of a structural reconstruction. (b) An anomalous LEED pattern observed in a $Sr_{0.95}La_{0.05}CuO_2$ sample, showing a doubling of the unit cell in the **a** and **b** directions.

from ordered oxygen vacancies in the topmost CuO_2 layer and is due to the polar nature of the infinite-layer structure. We emphasize that most $x = 0.10$ films, including all of the films presented in this chapter, did not show evidence of this reconstruction. There appears to be a doping-dependence to the reconstruction, with samples at lower doping levels displaying a higher susceptibility to the reconstruction.

Resistivity

Four-point *ex situ* resistivity measurements were performed on $Sr_{0.90}La_{0.10}CuO_2$ films in order to measure superconducting transition temperatures and widths. Superconducting samples showed a measured $T_c = 25 \pm 5$ K. The variability of T_c between films is likely due to incomplete oxygen reduction and small variations in lanthanum content. The superconducting dome in the n-type cuprates is relatively small, spanning a range $0.06 \leq x \leq 0.11$ for $Sr_{1-x}La_xCuO_2$ grown on scandate substrates [127], magnifying the

effects of any small deviations in lanthanum stoichiometry. As demonstrated in Figure 6.3, for optimal doping at $x \approx 0.10$, the temperature dependence of the resistivity in the normal state shows an approximate conventional Fermi liquid T^2 power law arising from electron–electron scattering [128], in contrast with the linear temperature dependence of the hole-doped cuprates [86, 87].

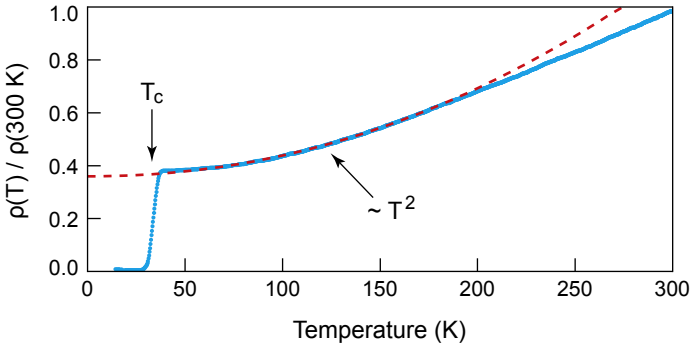

Figure 6.3: Four-point resistivity measurement of a $Sr_{0.90}La_{0.10}CuO_2$ thin film, normalized at room temperature. For this film, $T_c \approx 30$ K and the normal state resistivity approximates Fermi liquid T^2 behavior. The dashed line shows a fit to the function $\rho(T) = a + bT^2$.

X-ray diffraction

X-ray diffraction was employed to confirm growth of the intended infinite-layer phase and determine the absolute film thickness. Figure 6.4 shows a typical ω-2θ scan with clearly visible 001 and 002 diffraction peaks. The data shows a complete absence of the "long c-axis" phase [123] as well as any other impurity phase. The c-axis length is calculated to be 3.41 Å, in very good agreement with the bulk lattice constant of $Sr_{1-x}La_xCuO_2$ and with other films grown by MBE [127].

The film in Figure 6.4 also exhibits Kiessig fringes [178, 179] around the 002 diffraction peak, resulting from constructive and destructive interference of x-rays reflected from the film and substrate surfaces. The presence of these fringes generally indicates an extremely

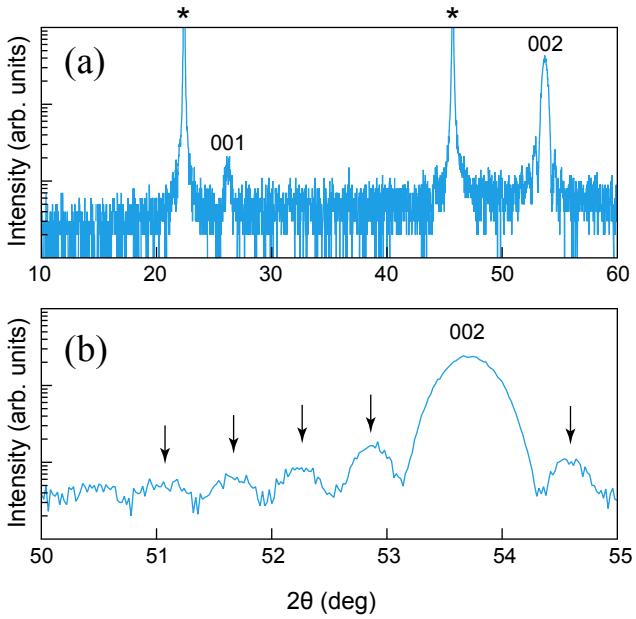

Figure 6.4: A typical ω-2θ x-ray diffraction scan (using Cu K_α radiation) for a $Sr_{0.90}La_{0.10}CuO_2$ thin film. (a) Wide-angle scan showing clear 001 and 002 c-axis diffraction peaks, both of which yield $c = 3.41$ Å. The two asterisks indicate (pseudocubic) 001 and 002 $GdScO_3$ substrate peaks ($c = 3.968$ Å). There is no evidence of an impurity phase in the film. (b) Detailed view of the 002 diffraction peak. Kiessig fringes, clearly visible on both sides of the peak and highlighted by arrows, can be used to determine the absolute thickness of the film (170 Å in this case) by using Equation 6.1.

flat interface. The fringes can be used to calculate the absolute thickness of the film using the diffraction formula

$$T = \frac{\lambda}{\Delta(2\theta)\cos(\theta_B)}, \tag{6.1}$$

where T is the film thickness, λ is the x-ray wavelength (1.542 Å for Cu K_α radiation), $\Delta(2\theta)$ is the average 2θ spacing of the fringes, and θ_B is the Bragg peak angle [180]. When applied to the data in Figure 6.4, Equation 6.1 gives a thickness of 170 Å, corresponding to 50 unit cells, in good agreement with the number of shuttering periods used to grow the film.

X-ray photoelectron spectroscopy

X-ray photoelectron spectroscopy was used to verify the lanthanum doping level of $Sr_{0.90}La_{0.10}CuO_2$ films. Although the technique is surface sensitive, exposing films to air for a short period of time (up to one day) during *ex situ* measurements does not appreciably affect the results. Figure 6.5 displays a typical x-ray photoelectron spectrum, showing the La $4d$, Cu $3s$, and Sr $3d$ core peaks. By comparing the total integrated areas (shaded in red) of the strontium and lanthanum peaks and normalizing by the photoionization cross sections [181], a lanthanum doping level of $x = 0.11 \pm 0.02$ is obtained, in good agreement with the nominal value $x = 0.10$.

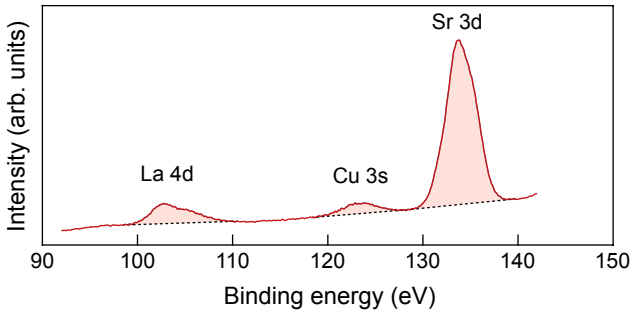

Figure 6.5: *Ex situ* x-ray photoelectron spectrum showing the La $4d$, Cu $3s$, and Sr $3d$ core peaks of a $Sr_{0.90}La_{0.10}CuO_2$ film. A lanthanum doping level of $x = 0.11 \pm 0.02$ is calculated for this film from the ratios of the normalized core peak areas.

It is interesting to note that the x-ray photoelectron spectrum for the O $1s$ core level of an annealed film consists of a doublet, as shown in Figure 6.6, which is not expected unless there are oxygen atoms in two different chemical environments within the film. Identical double-peaked O $1s$ spectra were collected from a sample that was cooled in ozone and for a sample that did not go through the annealing step. Previous x-ray photoelectron spectroscopy studies on $Sr_{0.90}La_{0.10}CuO_2$ have claimed that the weaker peak at higher binding energy is due to surface contamination [150, 151]. The fact that we see

an equivalent signal in samples unexposed to air and consistent across a wide range of annealing conditions, however, suggests a different, as-yet unknown, origin. The doublet may involve excess apical oxygens on the film surface, or it could be related to the surface reconstruction discussed in Chapter 8.

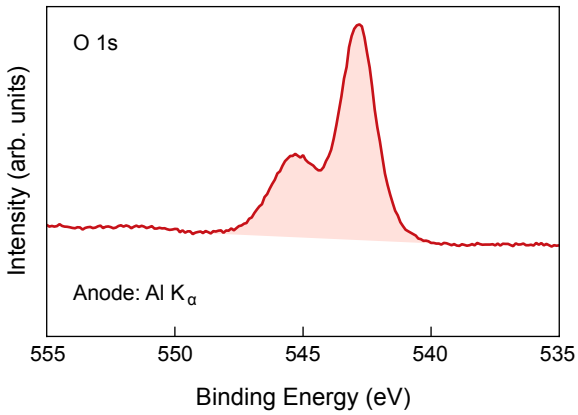

Figure 6.6: *In situ* x-ray photoelectron spectrum (using Al K_α radiation) showing the O $1s$ doublet seen in annealed (shown here) and unannealed $Sr_{0.90}La_{0.10}CuO_2$ films. The double-peaked shape of the spectrum is consistent across a wide variety of annealing conditions and suggests the presence of oxygen atoms in two different chemical environments.

X-ray absorption spectroscopy

X-ray absorption spectroscopy, employing the total electron yield method at the SGM beamline of the Canadian Light Source synchrotron, was used as an independent tool for verifying the lanthanum doping level of $Sr_{0.90}La_{0.10}CuO_2$ films. Figure 6.7 shows a typical x-ray absorption spectrum, displaying spin-orbit doublets of the La M ($3d \rightarrow 4f$) and Cu L ($2p \rightarrow 3d$) absorption edges. By comparing the two edge step heights (illustrated in gray) and normalizing by the photoabsorption cross section of the lanthanum and copper atomic cores [182], a lanthanum doping level of $x = 0.09 \pm 0.02$ was obtained, in good agreement with the nominal value $x = 0.10$.

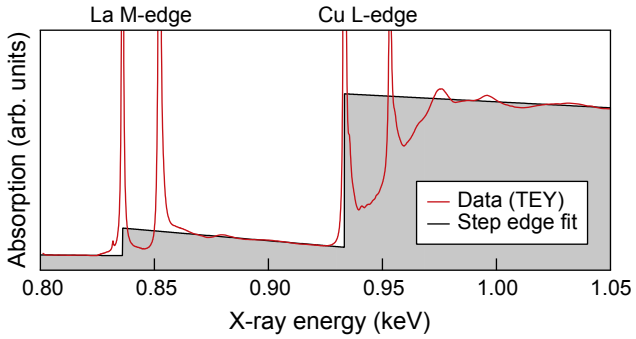

Figure 6.7: X-ray absorption spectrum showing the La M-edge and Cu L-edge of a $Sr_{0.90}La_{0.10}CuO_2$ film. A lanthanum doping level of $x = 0.09 \pm 0.02$ is calculated for this film from the x-ray absorption data (see text).

We note here the very close agreement between the nominal lanthanum doping level determined by *in situ* calibration utilizing a quartz crystal monitor and reflection high-energy electron diffraction oscillations [50], the atomic concentrations determined by both x-ray absorption spectroscopy and x-ray photoelectron spectroscopy, and the carrier concentration determined from ARPES measurements of the Fermi surface (Section 6.2.3). This suggests that the measured low-energy electronic structure of $Sr_{1-x}La_xCuO_2$ films is closely representative of the bulk, despite the polar nature of the crystal structure. This is further supported by the absence of a surface reconstruction observed by low-energy electron diffraction, as well as the similar temperature dependences of the superconducting gap measured by ARPES (see Section 6.5 below) and the superconducting transition measured by bulk resistivity.

6.2 Results from ARPES

This section presents ARPES data for $Sr_{0.90}La_{0.10}CuO_2$ thin films. Valence band spectra and a nodal dispersion are presented first, followed by a detailed Fermi surface mapping.

6.2.1 Valence band

To study the general effects of the vacuum annealing process, valence band spectra were measured for both as-grown and vacuum annealed $Sr_{0.90}La_{0.10}CuO_2$ films. As Figure 6.8 shows, a significant change in the O $2p$-derived valence band is observed after the vacuum annealing step. In particular, the leading edge of the valence band at $\sim$2 eV shifts toward higher binding energies after annealing. This is consistent with electron-doping of the film via the removal of excess oxygen atoms, which accept electrons. However, the marked change in the spectral weight of the valence band suggests an entirely different electronic structure for the as-grown film, beyond a simple doping picture. Annealed samples show slight variations in the shape of the valence band spectrum, but are qualitatively similar to that presented in Figure 6.8. The data in the remainder of this chapter are collected from properly vacuum annealed films.

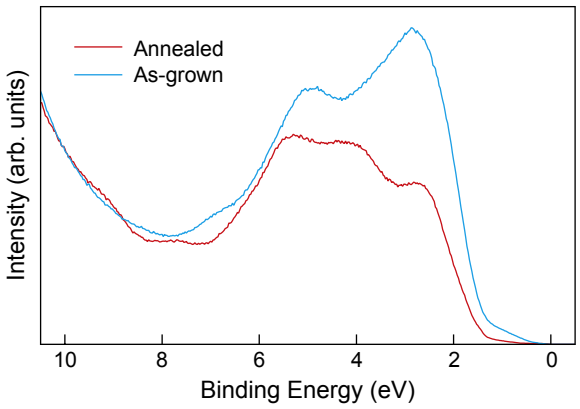

Figure 6.8: ARPES valence band spectra showing low-energy O $2p$-derived states in otherwise identical as-grown (blue) and vacuum annealed (red) $Sr_{0.90}La_{0.10}CuO_2$ films. A significant change in the valence band is observed after vacuum annealing, suggesting an entirely different electronic structure. The spectra have been normalized at high binding energy ($\sim$10 eV).

6.2.2 Nodal band dispersion

Figure 6.9 shows a cut from $(-2\pi, 0)$ to $(-\pi, \pi)$ through the node in the second Brillouin zone (cut II in Figure 6.10). The MDC-derived nodal quasiparticle dispersion, indicated by the white line, shows a clear upturn at a binding energy of about 40 meV. Low-energy kinks in band dispersions are usually interpreted in term of a coupling to one or more bosonic modes. However, a coupling of this nature results in a *decrease* in the band velocity, whereas a sharp increase in the dispersion is observed here. This is strong evidence for the opening of an energy gap at the Fermi level; the upturn is an artifact of the MDC analysis procedure, an effect commonly observed in other gapped systems [183].

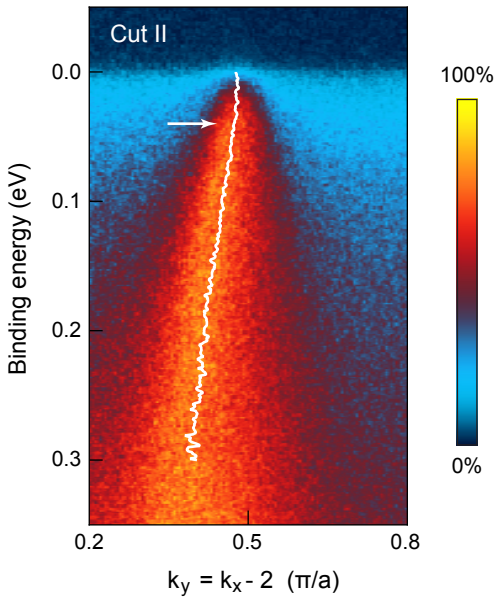

Figure 6.9: ARPES spectrum showing a cut from $(-2\pi, 0)$ to $(-\pi, \pi)$ through the node in the second Brillouin zone (cut II in Figure 6.10). The white line shows the band dispersion as determined by an MDC analysis. An upturn at 40 meV is identified by the white arrow.

6.2.3 Fermi surface

In Figure 6.10, an unsymmetrized k-resolved map of spectral weight near E_{F} is displayed. A large circular Fermi surface centered at (π, π), generic to all doped cuprates, is apparent. Fermi wavevectors (k_{F}'s) are extracted by fitting maxima in the MDCs used to generate the map. After applying appropriate symmetry operations, the set of k_{F}'s are plotted as yellow points in the areas outside of the map. Also shown is a two-dimensional tight-binding prediction for the shape of the Fermi surface (see Section 6.3 for details).

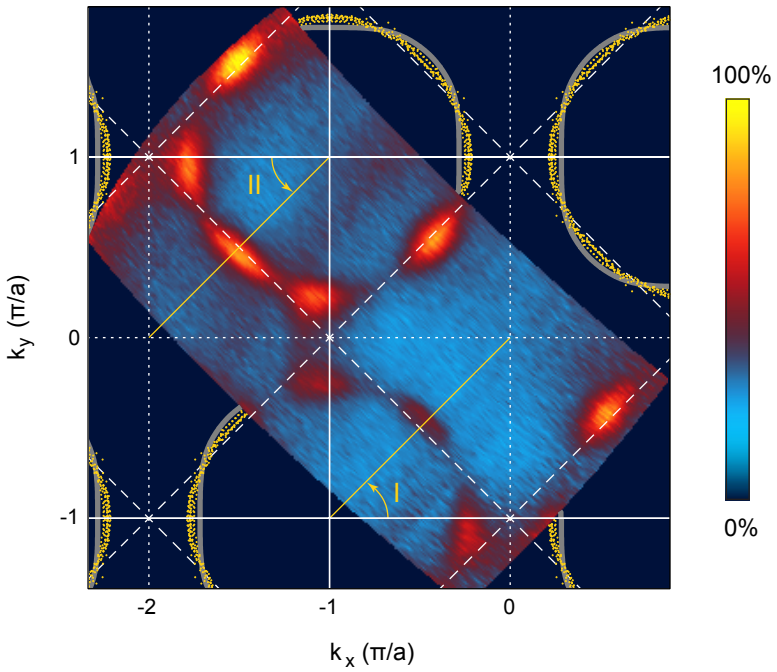

Figure 6.10: Unsymmetrized Fermi surface mapping for $Sr_{0.90}La_{0.10}CuO_2$ taken at 10 K showing spectral weight integrated within $E_{\mathrm{F}} \pm 30$ meV and normalized to a featureless background at high binding energy. Regions outside the map show the extracted k_{F}'s (yellow points) and the tight-binding Fermi surface (gray lines).

Assuming a quasi-two-dimensional Fermi surface, the experimentally determined k_{F}'s yield a Luttinger volume corresponding to $x = 0.09 \pm 0.02$, in agreement with the nominal doping level. Figure 6.11 highlights two notable features of the data. First, the

intensity is strongly modulated as a function of angle around the Fermi surface, a phenomenon originally observed in $Nd_{1.85}Ce_{0.15}CuO_4$ [184]. Second, the location of spectral weight along the nodal direction deviates significantly from the tight-binding prediction, whereas the agreement is better in other areas of momentum space. The next section presents a semi-empirical model that explains these features of the data.

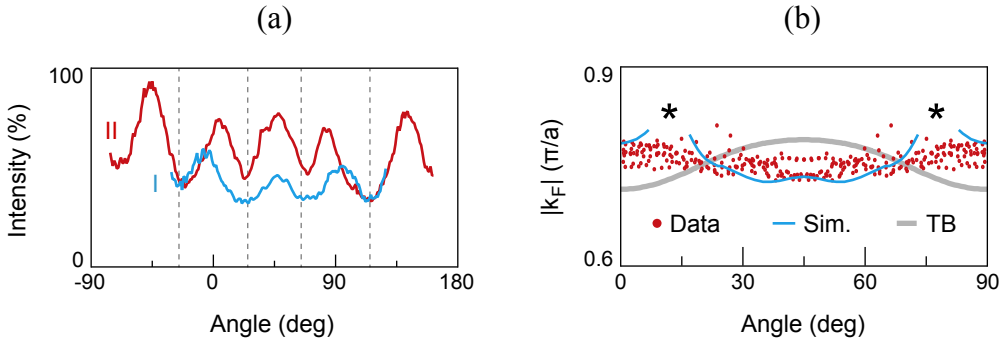

Figure 6.11: Analysis of Fermi surface mapping data. (a) Intensity versus angle along the two Fermi surface sheets, cuts I and II, as defined in Figure 6.10. Dashed lines mark where the Fermi surface crosses the antiferromagnetic zone boundary. (b) Experimental k_F's generated from the entire Fermi surface map and plotted by distance from (π, π) as a function of angle around the Fermi surface. The points deviate significantly from the tight-binding prediction but agree well with the simulation described in Section 6.3. The two asterisks mark the location of the hot spots, where a well-defined k_F cannot be reliably determined from the simulation.

6.3 Semi-empirical model of magnetism

To explain the data presented above in a comprehensive and consistent manner, we employ a simple model first proposed for the $Re_{2-x}Ce_xCuO_4$ family [184–186] whereby electrons with wavevectors **k** and **k** + (π, π) are mixed via an off-diagonal matrix element $V_{\pi\pi}$. Despite the lack of explicit strong electron correlations, this model has been shown to be successful in reproducing the key low-energy features in the electronic structure of the $Re_{2-x}Ce_xCuO_4$ family. The $V_{\pi\pi}$ term is assumed in this work to originate from static

or slowly fluctuating antiferromagnetism. It could also arise from any sufficiently strong (π, π) ordering, such as d-density wave order [187], but the strong antiferromagnetic ordering in $Re_{2-x}Ce_xCuO_4$ presents it as an obvious candidate. The term opens a gap of size $2\,|V_{\pi\pi}|$ at the intersection of the underlying band structure $\epsilon(\mathbf{k})$ with its image folded across the antiferromagnetic zone boundary $\epsilon'(\mathbf{k})$. The corresponding energies in this model are given by the equation

$$E_{\pm}(\mathbf{k}) = \frac{\epsilon(\mathbf{k}) + \epsilon'(\mathbf{k})}{2} \pm \sqrt{\left(\frac{\epsilon(\mathbf{k}) - \epsilon'(\mathbf{k})}{2}\right)^2 + |V_{\pi\pi}|^2}. \tag{6.2}$$

A schematic illustration of this bandstructure is shown in Figure 6.12. The gap results in so-called "hot spots" where spectral weight is dramatically suppressed, dividing the Fermi surface into two sheets: an electron pocket near the zone boundary at $(\pi, 0)$, and a hole pocket in the nodal region at $(\pi/2, \pi/2)$. This readily explains the observed intensity modulation displayed in Figure 6.11(a).

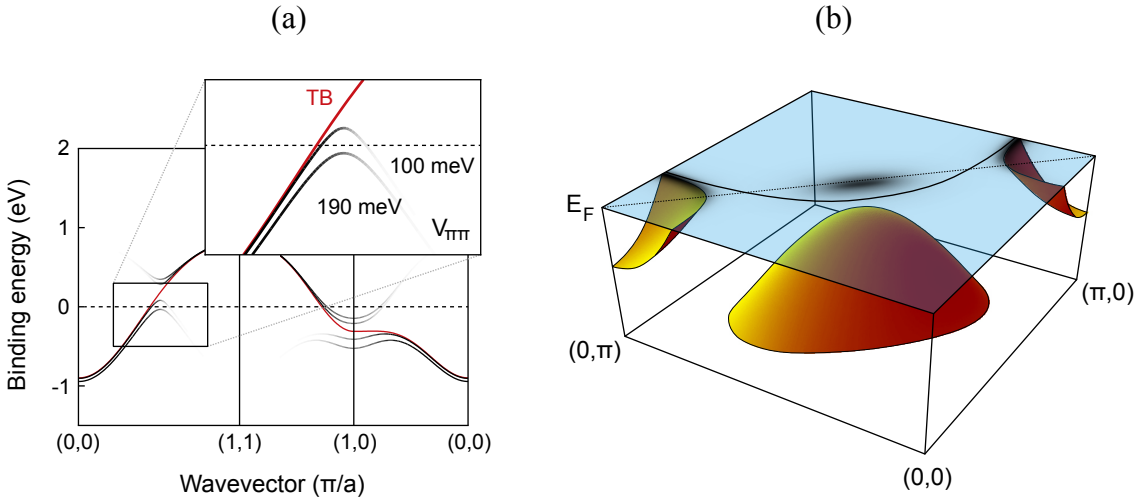

Figure 6.12: Schematic diagram of the semi-empirical model. (a) An illustration of the underlying band structure of the model. When $V_{\pi\pi} > 170$ meV, the nodal hole pocket is fully gapped (inset). (b) A three-dimensional diagram illustrating the band folding and the submergence of the nodal hole pocket below the Fermi energy for a sufficiently large value of $V_{\pi\pi}$.

To simulate this model and compare it to the experimental data, knowledge of the bare (non-magnetic, non-superconducting) band dispersion $\epsilon(\mathbf{k})$ is required. We use a simple two-dimensional tight-binding expression:

$$\begin{aligned}\epsilon(k_x, k_y) = \mu &- 2t\left[\cos\left(ak_x\right) + \cos\left(ak_y\right)\right] - 4t'\cos\left(ak_x\right)\cos\left(ak_y\right) \\ &- 2t''\left[\cos\left(2ak_x\right) + \cos\left(2ak_y\right)\right], \end{aligned} \tag{6.3}$$

where μ is the chemical potential, t is the nearest-neighbor hopping integral, t' is the next-nearest-neighbor hopping integral, and t'' is the next-next-nearest-neighbor hopping integral.

In order to determine the tight-binding parameters, we first constrain μ so that the electron filling stays fixed at $x = 0.10$. Then we vary t'/t and t''/t to reproduce the shape of the Fermi surface as predicted by density functional theory within the local density approximation (with a rigid band shift to account for an electron doping of $x = 0.10$, and for $k_z = \pi/c$ to best match the experimental Fermi surface). We performed the density functional theory calculations of $SrCuO_2$ using the full-potential linearized augmented plane wave method as implemented in the WIEN2k package [188]. Our results, displayed in Figure 6.13, are very similar to those for $CaCuO_2$ found in Reference [189]. Finally, t is adjusted to match the experimental high-energy dispersion in the nodal direction (2.4 eV·Å, the slope of the line below 0.1 eV in Figure 6.9). The resulting tight-binding parameters are given in Table 6.1 below.

In addition to the bare band dispersion, a phenomenological quasiparticle lifetime broadening term,

$$\frac{\hbar}{\tau} = \Gamma_0 + \Gamma_1|E - E_{\mathrm{F}}|, \tag{6.4}$$

is added in order to replicate the observed energy broadening in the ARPES data. The parameter values $\Gamma_0 = 70$ meV and $\Gamma_1 = 2.5$ are determined by comparing the simulation with experimental MDC widths, as illustrated in Figure 6.14.

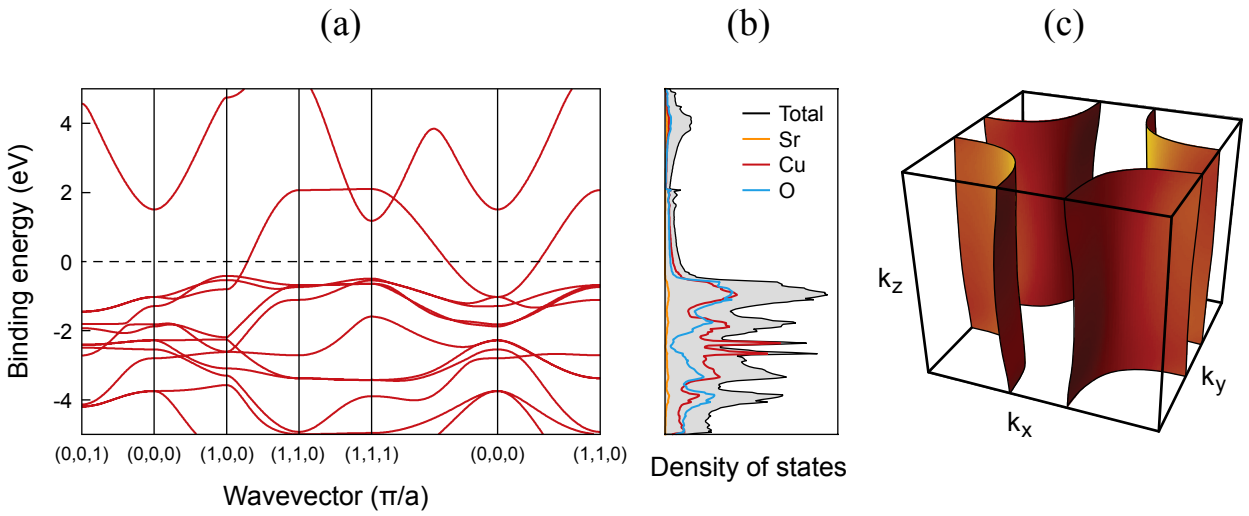

Figure 6.13: Density functional theory calculations of the band structure of $Sr_{0.90}La_{0.10}CuO_2$. (a) Spaghetti diagram showing low-energy bands. A rigid energy shift has been applied in order to account for 10% electron doping. There is very little dispersion along the c-axis. (b) Partial and total density of states. The low-energy bands are composed mostly of copper and oxygen hybridized states. (c) The three-dimensional Fermi surface of $Sr_{0.90}La_{0.10}CuO_2$.

We simulate the experimentally measured ARPES intensity (neglecting photoemission matrix elements) using a simple expression for the spectral function:

$$I(\mathbf{k}, E) \propto f(E) \left[\frac{A_+}{\left[E - E_+(\mathbf{k})\right]^2 + (\hbar/2\tau)^2} + \frac{A_-}{\left[E - E_-(\mathbf{k})\right]^2 + (\hbar/2\tau)^2} \right], \tag{6.5}$$

where $f(E)$ is the Fermi-Dirac distribution function representing temperature effects, $E_\pm(\mathbf{k})$ is the model's dispersion (Equation 6.2), τ is the empirical quasiparticle lifetime discussed above (Equation 6.4), and the coefficients $A_\pm$ are coherence factors that come about by diagonalizing the 2×2 matrix of our model and enforcing the restriction $A_+ + A_- = 1$:

$$A_\pm = \frac{1}{2}\left(1 \pm \frac{\epsilon(\mathbf{k}) - \epsilon'(\mathbf{k})}{\sqrt{\left(\epsilon(\mathbf{k}) - \epsilon'(\mathbf{k})\right)^2 + 4\left|V_{\pi\pi}\right|^2}}\right). \tag{6.6}$$

After fixing the energy dispersion and lifetime broadening, a least-squares fitting routine determines the value of $V_{\pi\pi}$ that best matches the low-energy MDC dispersion in the nodal direction (the area above 0.1 eV in Figure 6.9). We find that $V_{\pi\pi} = 190 \pm 50$ meV not

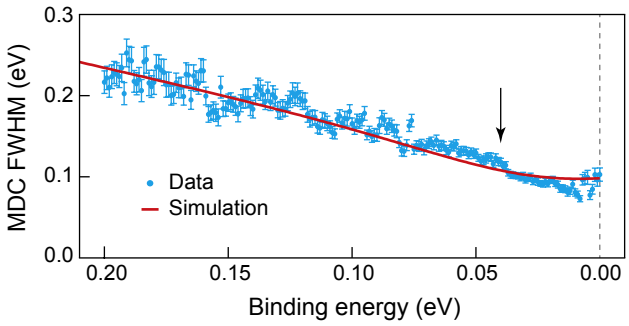

Figure 6.14: A comparison of experimental MDC full-widths at half-maximum (FWHMs) and the phenomenological lifetime broadening discussed above. Dots are derived from an MDC analysis of the experimental data shown in Figure 6.9, and the line is extracted from the simulation by an identical procedure. The gap-derived upturn in the dispersion at 40 meV also manifests itself in the quasiparticle lifetimes and is identified by an arrow.

only provides the best agreement with the extracted band dispersion, but also gives the best qualitative visual match to the experimental spectrum. However, our conclusion of gapped nodal states is robust against variations in the parameters of the simulation. Table 6.1 summarizes the semi-empirical model parameters, only one of which was varied to fit the data in the final step.

Table 6.1: $Sr_{0.90}La_{0.10}CuO_2$ model parameters

Parameter	**Description**	**Value**
μ	chemical potential	-6 meV
t	n-n hopping	215 meV
t'	n-n-n hopping	-34 meV
t''	n-n-n-n hopping	43 meV
Γ_0	broadening offset	70 meV
Γ_1	broadening energy dependence	2.5
$V_{\pi\pi}$	coupling to (π, π) order	190 meV

As illustrated in Figure 6.15, when $V_{\pi\pi}$ is sufficiently large (>170 meV in our model), the nodal pocket is pushed entirely below E_F, leaving only an electron sheet around $(\pi, 0)$. Such behavior has been reported for $Sm_{1.86}Ce_{0.14}CuO_4$ [186] and $Eu_{1.85}Ce_{0.15}CuO_4$ [190],

and is consistent with our data. Figure 6.18 shows an antiferromagnetism-induced pseudogap in the energy distribution curve at the node, and in Figure 6.16, we compare simulations of the model for $V_{\pi\pi} = 190$ meV with our data, where we find that a fully gapped nodal pocket is consistent with all of the other features of the data. The submergence of the nodal pocket shifts the near-E_{F} intensity toward $(\pi/2, \pi/2)$, explaining the inconsistency highlighted in Figure 6.11(b). Additionally, the upturn in the dispersion at 40 meV, as marked by the arrows in Figure 6.9 and 6.16(c), is an artifact of the MDC analysis procedure in the presence of a gap and is commonly observed in other systems [183]; an identical MDC-analysis of our simulation yields a similar upturn. We note that, presumably due to strong photoemission matrix element effects, the intensity of one side of the electron pocket formed at $(\pi, 0)$ is suppressed in the experimental Fermi surface map in the top panel of Figure 6.16(a), making it difficult to see the complete electron pocket.

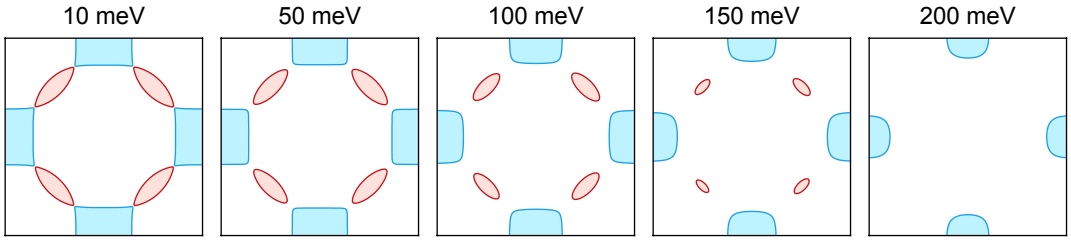

Figure 6.15: Illustration of the submergence of the nodal hole pocket (red) as a function of $V_{\pi\pi}$. The surviving electron pocket is shown in blue. We find that $V_{\pi\pi} = 190$ meV gives the best match to the experimental data for $Sr_{0.90}La_{0.10}CuO_2$.

If we revise our earlier Luttinger count assuming only small electron pockets in a folded zone (x vs. $1 + x$), we obtain a doping $x = 0.10 \pm 0.03$, again consistent with our chemical composition. The fact that in $Sr_{0.90}La_{0.10}CuO_2$ the Luttinger sum appears to agree using either the large hole pocket $(1 + x)$ or small electron pocket (x) counting scheme reflects the fact that when using the $1 + x$ scheme, our MDC analysis still counts the nodal regions as forming part of the Fermi surface even though they are, in reality,

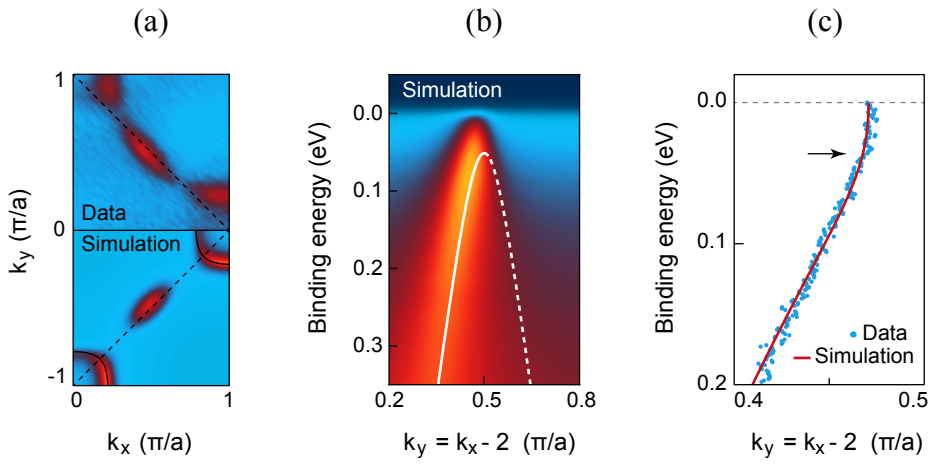

Figure 6.16: Simulation of the semi-empirical model. (a) Comparison of the experimental Fermi surface map and the simulation, neglecting final-state photoemission matrix elements. The dashed line marks the antiferromagnetic zone boundary and the solid line shows the underlying Fermi surface of the model. In the data and simulation, the weight at $(\pi/2, \pi/2)$ is not due to a true band crossing, but instead comes from the tail of the broad quasiparticle spectral function. (b) Simulation of the experimental spectrum presented in Figure 6.9. The white line shows the model's underlying band structure. (c) Nodal band dispersion, as determined by an MDC analysis. Dots are derived from the experimental data shown in Figure 6.9 and the line is extracted from the simulation in panel (b) by an identical procedure.

gapped. In the absence of (π, π) order, this large circular contour would constitute the underlying Fermi surface with an area of $1 + x$. This suggests that, at least for the purpose of counting the Luttinger volume, a simple mean-field spin-density-wave scenario appears to work for $Sr_{0.90}La_{0.10}CuO_2$ and the other electron-doped materials. This is in contrast with the hole-doped cuprates, where especially on the underdoped side there are major discrepancies in counting the doped carriers by ARPES using either an x or $1 - x$ picture [191]. This is likely related to the fact that in the most lightly electron-doped compounds, the low-energy states clearly form closed electron pockets around $(\pi, 0)$, while in the lightly hole-doped materials, the contour of low-energy excitations appears to form a discontinuous "Fermi arc" [192], which is more poorly understood and still a subject of debate. This suggests a fundamental difference between electron- and hole-doped

cuprates, specifically in the nature of the Fermi surface and the integrity of states near the antinodes at $(\pi, 0)$.

The ability to explain all experimental features using a simple model strongly suggests that the coupling of electrons to (π, π) order in $Sr_{0.90}La_{0.10}CuO_2$ results in a reconstructed Fermi surface that gaps the nodal pocket. This cuprate Fermi surface topology, comprised solely of small electron pockets, has been reported in numerous quantum oscillation measurements of $YBa_2Cu_3O_{6+\delta}$ at high magnetic fields and may be relevant to those observations, particularly because such fields have been shown to stabilize antiferromagnetism [193, 194].

6.4 Temperature dependence

By comparing the near-$E_{\rm F}$ spectral difference between the node and the hot spot, we can remove trivial temperature effects from the Fermi step and determine the temperature dependence due to the antiferromagnetic order alone. Figure 6.17 shows this spectral difference for a series of temperatures. Due to the presence of the antiferromagnetic gap, the spectral intensity measured at the hot spot is dramatically reduced relative to the node over a 200 meV energy scale below $E_{\rm F}$. This suppression drops rapidly between 150 K and 250 K. Assuming that static antiferromagnetic order exists, this could be associated with the closing of the gap above the Néel transition. From our data, we estimate a characteristic transition temperature $T^* = 220 \pm 30$ K. The similarity between our T^* and the Néel temperature $T_{\rm N}$ for other electron-doped cuprates suggests that the observed spectral change could arise from the Néel transition. However, we cannot conclusively determine if the antiferromagnetism in $Sr_{0.90}La_{0.10}CuO_2$ is static or arises from fluctuating antecedent spin correlations [83].

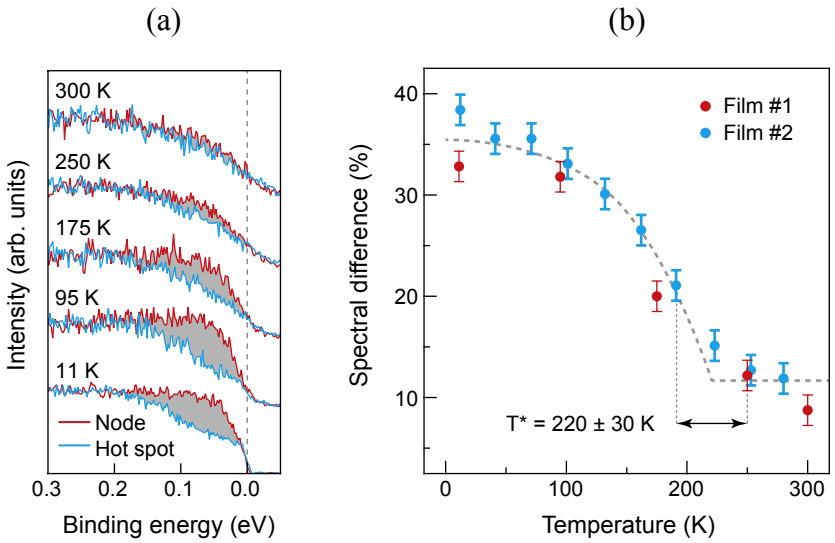

Figure 6.17: Temperature dependence of the hot spot. (a) Temperature series of background-subtracted EDCs, offset for clarity, at a node and a neighboring hot spot. (b) Difference in spectral weight between the node and hot spot, shaded gray in panel (a), as a function of temperature. The dashed line is a guide to the eye. We estimate a characteristic transition temperature $T^* = 220 \pm 30$ K.

6.5 Superconductivity

Measurements of as-grown non-superconducting $Pr_{2-x}Ce_xCuO_4$ samples have shown a gapping of nodal states that was argued to arise from the presence of excess oxygen [102]. In fact, it may be that apical oxygen atoms and strong antiferromagnetism are two sides of the same coin: the presence of excess oxygen atoms at apical sites could facilitate the formation of antiferromagnetic order, thereby gapping the nodal states. Our samples were oxygen reduced and confirmed to be superconducting by *ex situ* transport measurements with T_c's in the range 25 ± 5 K (c.f. Section 6.1.3). In addition, in Figure 6.18, measurements from two samples exhibiting clear superconducting gaps of Δ = 1 to 2 meV on the electron pockets are shown, with the gap closing upon warming above T_c. This gap value is consistent with $Re_{2-x}Ce_xCuO_4$, where $\Delta \approx 2$ meV [195, 196], and confirms that small gaps are generic to electron-doped cuprates. As argued above, the hole pocket does not

possess strong coherent weight at E_F and thus exhibits only a trivial temperature dependence due to thermal broadening of the Fermi edge.

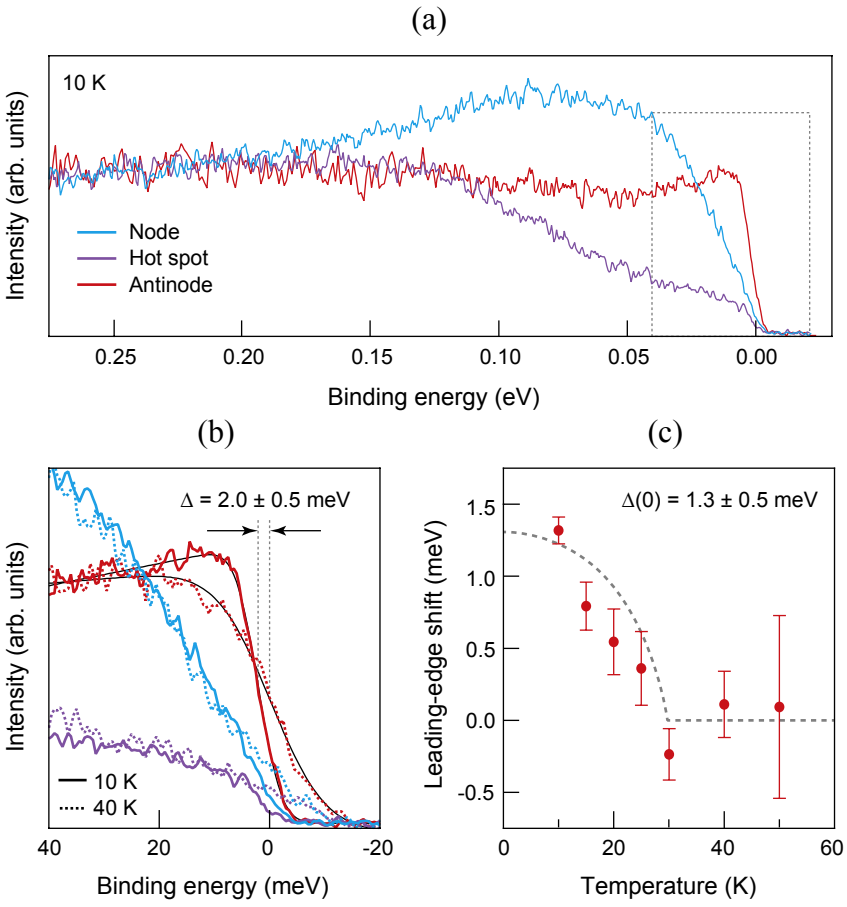

Figure 6.18: Superconductivity in $Sr_{0.90}La_{0.10}CuO_2$. (a) Comparison of low-temperature background-subtracted EDCs at the node, hot spot, and antinode for a superconducting film. (b) Close-up of the dashed box in panel (a), with high-temperature data superimposed. The antinode shows a leading-edge shift at low temperature due to the superconducting gap. The solid black lines are fits to a Fermi function. (c) Temperature dependence of the leading-edge shift for a second superconducting film. An uncertainty of ± 0.5 meV for the superconducting gap Δ in both samples is estimated from systematic errors in background subtraction and the Fermi function fitting procedure.

The gapping of the hole pocket by antiferromagnetism therefore can naturally explain the numerous reports of fully gapped superconductivity in $Sr_{0.90}La_{0.10}CuO_2$ [143,152,154, 163,164] without needing to invoke a change in the symmetry of the order parameter from

d to s. This nodeless d-wave scenario has been proposed theoretically by Yuan *et al.* [197] and Das *et al.* [198], and coexisting antiferromagnetism and superconductivity has been proposed theoretically by Sénéchal *et al.* [171]. Because the momentum range spanned by the electron pockets is narrow, we do not observe any substantial gap anisotropy, nor can we unequivocally rule out the possibility of s-wave superconductivity. However, a recent phase-sensitive measurement of $Sr_{0.90}La_{0.10}CuO_2$ shows a $d_{x^2-y^2}$ symmetry of the superconducting order parameter [166], in agreement with our findings. Our results demonstrate that cuprate high-T_c superconductivity can occur in a material with only electron-like carriers, coexistent antiferromagnetism, and without d-wave nodal quasiparticles.

6.6 Conclusion

In conclusion, we have performed the first ARPES measurements on the infinite-layer cuprate $Sr_{0.90}La_{0.10}CuO_2$. Based on the accuracy of the Luttinger count, the success of our simple model of magnetism, and the observation of a superconducting gap at $(\pi, 0)$, we conclude that strong antiferromagnetic tendencies and superconductivity coexist simultaneously and homogeneously in $Sr_{0.90}La_{0.10}CuO_2$. The unusually strong coupling of electrons to (π, π) antiferromagnetism results in a Fermi surface reconstruction comprised solely of electron-like carriers. Superconductivity is restricted only to electron pockets, providing the first direct observation of high-T_c superconductivity in a cuprate completely devoid of hole-like carriers, as recently proposed by theoretical calculations [197, 198]. Furthermore, we have demonstrated that a gapping of the nodal states near $(\pi/2, \pi/2)$ by antiferromagnetism suppresses d-wave nodal quasiparticles. This picture can provide a natural explanation of the earlier conflicting reports regarding the nature of superconductivity in $Sr_{1-x}La_xCuO_2$ [143, 152, 154, 163, 164]. By performing the first direct measurements of the electronic structure of an n-type cuprate distinct

from $Re_{2-x}Ce_xCuO_4$, we have firmly established that robust antiferromagnetism and a small superconducting gap are intrinsic features of the electron-doped cuprates and not material-specific.

CHAPTER 7

THE DOPING EVOLUTION OF $Sr_{1-x}La_xCuO_2$

As we have shown in Chapter 6, there is a clear asymmetry in the doping-controlled insulator–metal transition in the cuprates, with important ramifications for theories of high-temperature superconductivity. In this chapter, we use ARPES to examine the doping dependence of the electronic structure of thin films of $Sr_{1-x}La_xCuO_2$. We first describe the film growth and experimental methods, and then present measurements of the parent insulating state of $Sr_{1-x}La_xCuO_2$ at low doping, which show a dispersive lower Hubbard band characteristic of other cuprate parent materials. We then demonstrate that with increased electron doping, a continuous evolution from insulator to superconductor occurs as the Mott gap is gradually filled in. Finally, we discuss the linear dependence of the measured background intensity on doping.

7.1 Methods

The following section briefly describes the growth and measurement of $Sr_{1-x}La_xCuO_2$ thin films. More detailed information concerning growth and characterization can be found in Reference [128] and the supplemental material of Reference [173], respectively.

7.1.1 Film growth

$Sr_{1-x}La_xCuO_2$ thin films (x = 0.01, 0.05, and 0.10) with a nominal thickness of 60 unit cells (20 nm) and terminated with CuO_2 were deposited using a Veeco GEN10 dual-chamber oxide molecular-beam epitaxy system. The films were grown epitaxially on (110) $GdScO_3$ substrates, which have a distorted perovskite structure with a pseudocubic lattice con-

stant of 3.968 Å [174]. Shuttered layer-by-layer deposition was performed in a background of 100% distilled O_3 at a pressure of 1×10^{-6} Torr and with a substrate growth temperature of 510 °C. Depositions were monitored using RHEED. After growth, samples were oxygen-reduced by vacuum annealing at 520 °C for 30 minutes in order to eliminate excess oxygen atoms. The films were then cooled to 200 °C before immediate transfer under ultra-high vacuum to the ARPES chamber. Samples with $x = 0.10$ were superconducting, exhibiting bulk resistance transitions in the range 25 ± 5 K.

7.1.2 ARPES measurements

ARPES measurements were performed with a VG Scienta R4000 electron spectrometer and He-Iα photons (21.2 eV) at a base pressure of 7×10^{-11} Torr and with an instrumental resolution better than ΔE = 20 meV and Δk = 0.03 Å^{-1}. The sample temperature was held at 200, 30, and 10 K for x = 0.01, 0.05, and 0.10, respectively. The Fermi level E_{F} was determined by measuring polycrystalline gold in electrical contact with the sample. Experimental results were confirmed by studying multiple samples. After ARPES measurements, samples were characterized by *in situ* LEED to examine surface structure and quality. X-ray photoelectron spectroscopy was used to verify the stoichiometry of the films, confirming the lanthanum doping level to within 10% of x.

7.2 Parent electronic structure

The undoped parent compounds of the cuprates are Mott (or, more accurately, charge-transfer) insulators in which strong local Coulomb interactions invalidate a conventional band structure picture. Instead, the low-energy electronic structure is composed of a

fully-occupied lower Hubbard band, which typically has a bandwidth of $\sim$0.3 eV and a minimum in momentum space at $(\pi/2, \pi/2)$, and an unoccupied upper Hubbard band separated by the Mott gap [199].

7.2.1 Experimental data

In Figure 7.1, we show ARPES data for $Sr_{0.99}La_{0.01}CuO_2$, where $x = 0.01$ was intentionally added to prevent electrostatic charging of the sample which was observed in stoichiometric $SrCuO_2$ films. A small shoulder in the tail of the valence band is clearly present. After subtraction of a background EDC obtained by averaging the valence band tail near $(0, 0)$, we observe a dispersive peak with a broad lineshape, characteristic of the lower Hubbard band in other parent cuprates [200, 201]. The spectral shape of the lower Hubbard band is due to Franck-Condon broadening in which the coupling to a bosonic mode causes the spectral function to split into a set of discrete peaks. Each peak represents a resonance with a different boson occupation number, with the true quasiparticle pole residing in the low-binding-energy tail of intensity [200]. At $(\pi/2, \pi/2)$, the lineshape can be well-fitted to a simple three-parameter Gaussian function, shown in Figure 7.1(c), with the intensity maximum in the lower Hubbard band at a binding energy of 0.81 eV and a full-width at half-maximum of 0.41 eV. This compares well with the lower Hubbard band observed in other cuprate parent compounds, such as $Ca_2CuO_2Cl_2$ [200] and Nd_2CuO_4 [201], as shown in Table 7.1. The position of the lower Hubbard band in $Ca_2CuO_2Cl_2$ is omitted because it is strongly cleave-dependent. Measurement temperatures are included in the table because the width of the lower Hubbard band has a strong temperature dependence.

As Figure 7.1(d) shows, the lower Hubbard band is dispersive, exhibiting a symmetrical energy minimum at $(\pi/2, \pi/2)$. The single-band t-t'-t''-J model is often used to de-

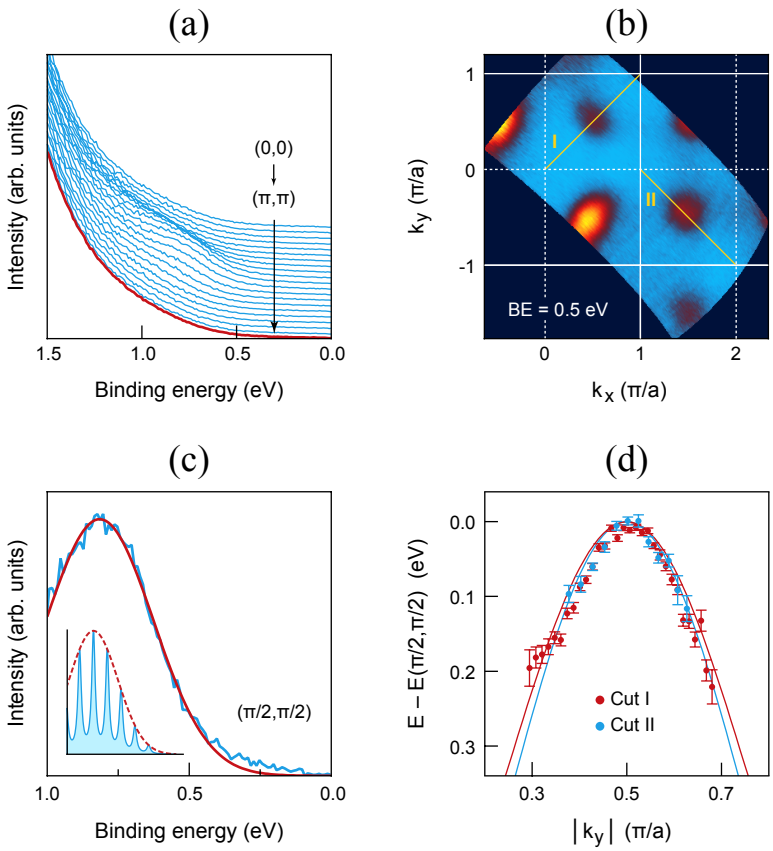

Figure 7.1: The low-energy electronic structure of $Sr_{0.99}La_{0.01}CuO_2$. (a) EDCs (offset for clarity) along a diagonal cut from $(0,0)$ to (π,π) through the lower Hubbard band, which is visible as a bump at the foot of the valence band. The bold red line shows the background EDC subtracted from the data in the remaining panels in order to enhance the lower Hubbard band. (b) Momentum space map of spectral weight at a binding energy of 0.5 eV showing the lower Hubbard band at $(\pi/2,\pi/2)$ and equivalent points. (c) EDC at $(\pi/2,\pi/2)$ after background subtraction. The peak has a Franck-Condon lineshape (demonstrated schematically in the lower left inset) and can be fit to a Gaussian (red curve). The "foot" in the low-binding-energy region deviates slightly from the Gaussian and most likely reflects low-energy levels occupied by the small amount of dopants added to the sample. (d) Dispersion of the lower Hubbard band as a function of momentum along Cut I from $(0,0)$ to (π,π) (red points) and along perpendicular Cut II from $(\pi,0)$ to $(2\pi,-\pi)$ (blue points), as determined by Gaussian fitting. The smooth curves show the dispersion predicted by the t-t'-t''-J model.

Table 7.1: Parameters of the lower Hubbard band in selected cuprates

Material	Position (eV)	Width (eV)	Temperature (K)	Reference
$Ca_2CuO_2Cl_2$	—	0.34	>180	[200]
Nd_2CuO_4	1.30	0.36	10 - 20	[201]
$SrCuO_2$	0.81	0.41	160	This work

scribe the motion of a doped hole in a two-dimensional antiferromagnetic insulator. Here the t' and t'' parameters are renormalized effective hopping amplitudes that are necessary in order to reproduce the dispersion along the $(\pi, 0)$ to $(0, \pi)$ direction that is clearly observed in experiment. The dispersion relation of the model, relative to the energy at $(\pi/2, \pi/2)$, follows the equation [202]:

$$E(k_x, k_y) = -0.55J\left(\cos k_x + \cos k_y\right)^2 - 4t' \cos k_x \cos k_y - 2t''\left(\cos 2k_x + \cos 2k_y\right). \quad (7.1)$$

By fixing $J = 150$ meV and allowing t' and t'' to vary in order to match the experimentally measured curvature in the nodal and transverse directions, we obtain a good fit to the data with $t' = -53$ meV and $t'' = 66$ meV. This is similar to the values $J = 140$ meV, $t' = -38$ meV, and $t'' = 22$ meV from Reference [202], obtained by fitting to self-consistent Born approximation calculations of $Sr_2CuO_2Cl_2$, another undoped cuprate. The similarity suggests a universality of the electronic structure of the cuprates at low doping.

7.2.2 Comparison of the lower Hubbard band with theory

Figure 7.2 compares the observed lower Hubbard band with theoretical predictions for the band structure of $SrCuO_2$. Density functional theory, within the local density approximation and using the full-potential linearized augmented plane wave method as implemented in the WIEN2k package [188], was used to calculate the band structure of $SrCuO_2$. The calculated dispersion is very similar to that for $CaCuO_2$ found in Reference [189].

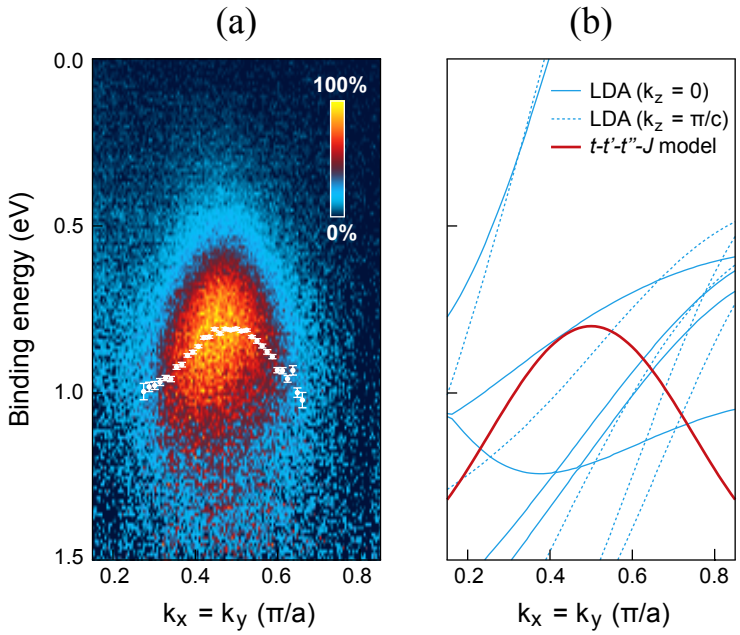

Figure 7.2: Comparison of the lower Hubbard band with theory. (a) Experimental spectrum along $(0, 0)$ to (π, π) after background subtraction showing the lower Hubbard band. The white dots show the band dispersion as extracted by an EDC analysis. (b) Theoretical band structure expected by density functional theory (blue curves) and the t-t'-t''-J model (red curve). The latter does a much better job of predicting the observed electronic structure.

The low-energy valence band is derived mainly from copper and oxygen orbitals, forming a complex manifold of states that do not hybridize with the lower Hubbard band and that are removed in the background-subtraction procedure. The calculated Cu $3d_{x^2-y^2}$ band, relevant to superconductivity and other low-energy physics, differs markedly from the experimental data, highlighting the effects of strong electron correlations, which turn $SrCuO_2$ from a half-filled metal into an antiferromagnetic insulator. While weak interaction methods such as density functional theory predict a metallic state, the t-t'-t''-J model in conjunction with Franck-Condon broadening does a much better job of predicting the observed electronic structure. It accounts for the bandwidth change from $8t \sim 3$ eV to $2J \sim 0.3$ eV and the dispersion symmetry around the antiferromagnetic zone boundary in momentum space at $(\pi/2, \pi/2)$.

7.3 Filling in the Mott gap

Upon the addition of n-type carriers into the CuO_2 planes via the substitution of trivalent lanthanum for divalent strontium in the intervening layers of $Sr_{1-x}La_xCuO_2$, the Mott gap is gradually filled in as the upper Hubbard band evolves into a continuous hole-like Fermi surface centered at (π, π).

7.3.1 Nodal spectra

The nodal spectra presented in Figure 7.3 show that rather than closing abruptly, the Mott gap appears to soften upon electron doping from 1% to 10%. This conflicts with a conventional band picture, where the lowest-lying unoccupied valence states are filled in as the electron doping rises, increasing the chemical potential and pushing all occupied states higher in energy. Instead, there appears to be a qualitative change in the nature of the low-energy excitations of the system: the incoherent localized states that make up the lower Hubbard band give way to a coherent itinerant band dispersing through the Fermi level. Unfortunately, significant doping-induced changes in the valence band shape and structure prevent an unambiguous determination of a chemical potential shift during the doping evolution of $Sr_{1-x}La_xCuO_2$.

Figure 7.3(d) highlights a notable feature in the nodal dispersion derived from an MDC analysis: at approximately 0.2 eV, the dispersion appears to "boomerang" backwards. This phenomenon is observed at multiple equivalent points in momentum space and is not consistent with single-band physics. Instead, the effect arises from a two-component spectral function illustrated in Figure 7.4(b): a coherent low-energy band forming the Fermi surface and a large contribution of incoherent spectral weight at higher

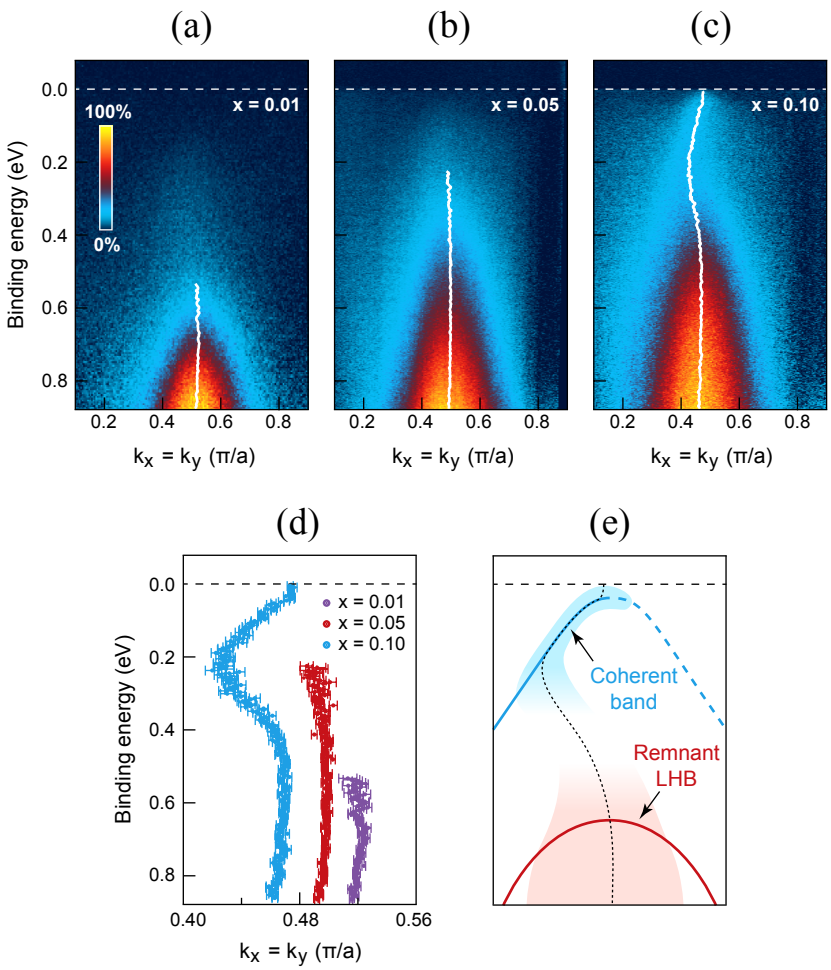

Figure 7.3: Evolution of nodal electronic structure with doping. Spectra along $(0, 0)$ to (π, π) after background subtraction (a) for $x = 0.01$, (b) for $x = 0.05$, and (c) for $x = 0.10$. As the doping level increases, the spectral weight of the lower Hubbard band shifts to lower binding energy and gradually fills in the Mott gap. At $x = 0.10$, a coherent band near the Fermi level is visible. (d) MDC-derived dispersion for $x = 0.01$, 0.05, and 0.10 (also shown as white lines in the preceding panels). The lower Hubbard band maximum appears to shift away from $(\pi/2, \pi/2)$ with increased doping. The "boomerang" phenomenon is clearly visible for $x = 0.10$. (e) Schematic diagram showing the qualitative form of the spectral function for $x = 0.10$. Spectral weight fills in the Mott gap, forming a coherent band on top of the remnant lower Hubbard band. The "boomerang" phenomenon in MDC-derived dispersions, shown by the black dashed line, is an artifact arising from the presence of two concurrent bands.

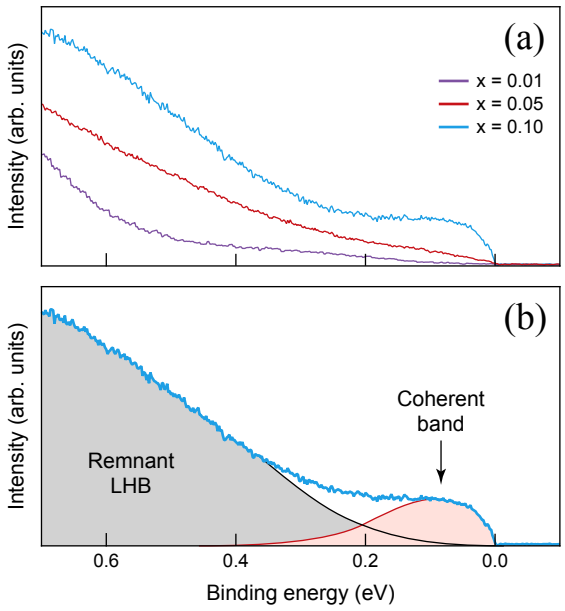

Figure 7.4: Nodal energy distribution curves. (a) Doping dependence of EDCs at $(\pi/2, \pi/2)$ for $x = 0.01$, 0.05, and 0.10. As the doping level increases, states are filled in near the Fermi level. (b) An illustration of the two-component spectral function for $x = 0.10$. The EDC is made up of a coherent low-energy band and an incoherent high-energy remnant lower Hubbard band.

energies from a remnant lower Hubbard band that survives even at $x = 0.10$. This behavior differs from the hole-doped cuprates or the $Re_{2-x}Ce_xCuO_4$ family, where so-called "waterfalls" are observed at higher binding energies [203]. Recent sophisticated theoretical calculations that take into account strong electron correlations have predicted the existence of both a coherent low-energy band and an incoherent high-energy branch at 10% electron doping [171, 172], the observation of which we report here. Figure 7.3(d) also shows that the lower Hubbard band maximum appears to shift from $(\pi/2, \pi/2)$ towards $(0, 0)$ with doping at a rate of approximately 8.5×10^{-3} $(\pi/a)/\%$, which is quantitatively similar to the behavior observed for p-type $Ca_{2-x}Na_xCuO_2Cl_2$, where the lower Hubbard band shifts with hole doping at a rate of 7.5×10^{-3} $(\pi/a)/\%$ [200]. Interestingly, the maximum shifts in the same direction for both electron and hole doping. The prominence of the remnant lower Hubbard band in the experimental data highlights the important role

that strong local electron correlations play in the electronic structure of $Sr_{1-x}La_xCuO_2$ even at relatively high doping levels.

7.3.2 Constant energy maps

Figure 7.5 shows how the spectral weight of $Sr_{1-x}La_xCuO_2$ evolves in momentum space with increasing electron doping. At the Fermi level, the $x = 0$ sample lacks intensity because it is in an insulating state. As carriers are added to the system, spectral weight first develops at $(\pi, 0)$ and equivalent points, as evidenced by the Fermi surface map of the $x = 0.05$ sample. This behavior is similar to that seen in the electron-doped $Re_{2-x}Ce_xCuO_4$ family, where at low doping levels the Fermi surface is composed of small electron pockets centered at $(\pi, 0)$ [201]. By $x = 0.10$, a fully-formed Fermi surface consisting of a large hole pocket centered at (π, π) has evolved. This Fermi surface is punctuated by a periodic modulation of intensity, forming the "hot spots" that are indicative of antiferromagnetic order [204]. In fact, as we have shown in Chapter 6, in $Sr_{0.90}La_{0.10}CuO_2$, the antiferromagnetic order appears to coexist with superconductivity. Figure 7.5 also displays maps at higher binding energies, where all three doping levels show evidence of a remnant lower Hubbard band which takes the form of diffuse regions of spectral weight centered around $(\pi/2, \pi/2)$ and is coexistent with the coherent bands dispersing through the Fermi level.

An interesting feature in the Fermi surface map of the $x = 0.05$ sample, as circled in Figure 7.5(b), is weak but finite spectral weight at $(0, 0)$ and (π, π). Bands at these locations in momentum space are expected by neither tight-binding, density functional theory, nor the t-t'-t''-J model. Instead, as elaborated in Chapter 8 below, it appears that the observed intensity is the result of a $p(2\times2)$ surface reconstruction of the sample, which causes shadows of the real spectral weight at $(\pi, 0)$ to be reflected onto these locations in

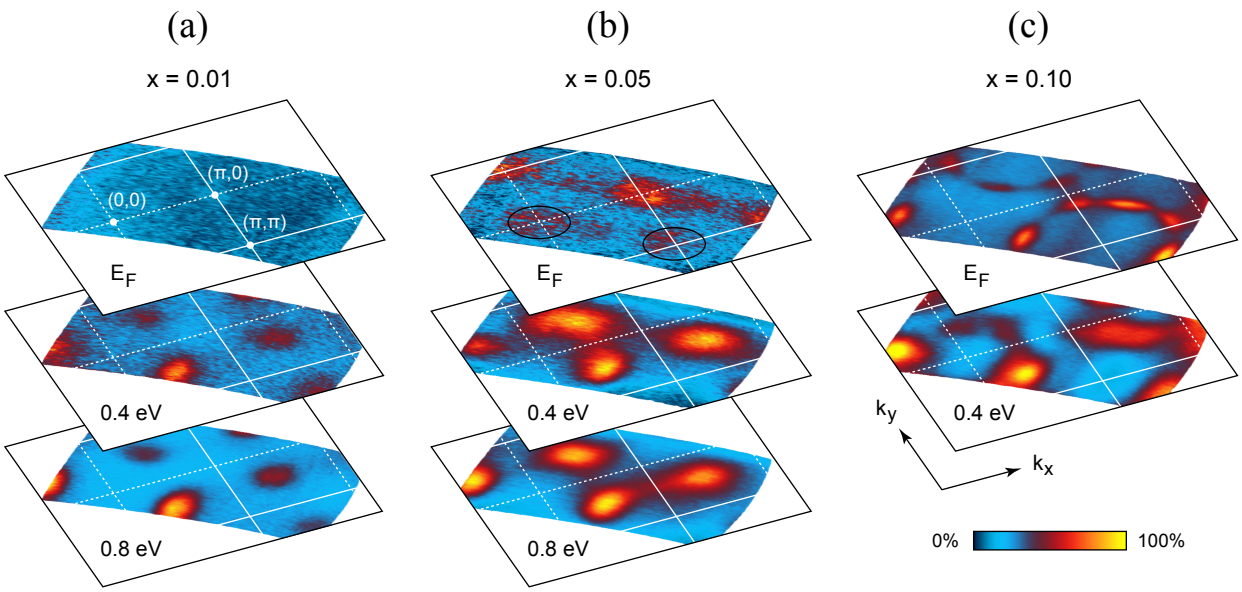

Figure 7.5: Momentum space evolution of spectral intensity with doping. Constant energy spectral maps (a) for $x = 0.01$, (b) for $x = 0.05$, and (c) for $x = 0.10$, integrated within ± 50 meV of the specified binding energy. At the Fermi level, the insulating $x = 0.01$ sample shows no spectral weight, while the $x = 0.05$ sample shows an accumulation of weight at $(\pi, 0)$. By $x = 0.10$, a large hole-like Fermi surface centered at (π, π) and with characteristic "hot spots" has developed. At higher binding energies, there is clear evidence for a coexisting lower Hubbard band with intensity near $(\pi/2, \pi/2)$ for all three doping levels. The circled regions at the top of panel (b) show shadow band reflections from spectral weight at $(\pi, 0)$ due to a $p(2 \times 2)$ surface reconstruction in this sample, as discussed in Chapter 8 below.

momentum space. At higher binding energies, evidence of this reconstruction is absent because reflections from intense regions of the remnant lower Hubbard band fall onto each other.

7.4 Background intensity

Spectra from all films showed a momentum-independent background present throughout the entire Brillouin zone, giving rise to spectral weight near the Fermi level even where no low-energy bands are expected. This background, typical of the cuprates, is

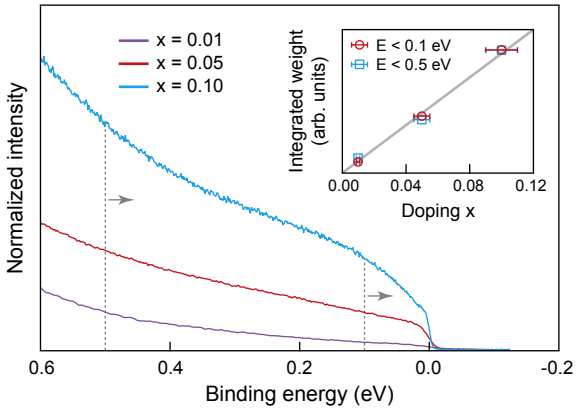

Figure 7.6: Doping dependence of the background signal. Main panel: Energy distribution curves averaged over momentum space near $(0, 0)$, where no low-energy bands are expected, and normalized to the high-energy valence band. A significant background signal that grows with doping is observed. Inset: Normalized spectral weight integrated up to a binding energy of 0.1 eV (circles) and 0.5 eV (squares) as a function of doping. The data fall on a straight line regardless of the integration range (vertical dashed lines in the main panel), indicating that the background intensity is directly proportional to doping. Error bars are 10% of doping.

thought to arise from elastic scattering of photoelectrons escaping from the surface [175]. Figure 7.6 demonstrates that this background, if properly normalized to the doping-independent high-energy valence band, is linearly proportional to the doping level x. There are two possible explanations for this proportionality: higher doping levels increase the number of low-energy electrons which are scattered in the photoemission process, or the rising dopant disorder increases the final-state scattering rate. The observed linear doping dependence indicates that only one explanation can hold. Because we clearly observe an increased density of electrons which fill in the Mott gap as the doping level is raised, this suggests that the former explanation is dominant and that dopant disorder has little effect on the formation of the background intensity.

Within, for example, a tight-binding model or density functional theory, the density of states at the Fermi level is expected to decrease gradually with electron doping in the cuprates. We observe here, however, a linear rise in the density of low-energy carriers

with increasing x. It is not surprising that these theories get this behavior wrong, as they neglect strong electron correlations and predict metallic behavior even at low doping. As Section 7.3 discusses above, it appears instead that within the insulator-to-metal transition in $Sr_{1-x}La_xCuO_2$, carriers gradually fill in the Mott gap as it closes to form a metallic state. This results in a continuous increase in the density of low energy states with doping, causing the observed increase in the background intensity.

Finally, we point out that the observed background intensity measured in all $Sr_{1-x}La_xCuO_2$ films is unusually high relative to other complex oxide thin films. As we discuss in Chapter 8 below, a polar reconstruction occurs in the infinite-layer films. This reconstruction presumably creates an electronically "dead" topmost CuO_2 layer. In this case, photoemission experiments will probe the first buried CuO_2 layer, resulting in an enhanced background signal that we observe here. We emphasize that his background is a final-state effect and is not related to the intrinsic quasiparticle scattering rate.

7.5 Conclusion

In this chapter, we have studied the doping dependence of thin films of the infinite-layer electron doped cuprate $Sr_{1-x}La_xCuO_2$. At low doping, a dispersive lower Hubbard band characteristic of cuprate parent compounds is observed. The t-t'-t''-J model in conjunction with Franck-Condon broadening does an excellent job of predicting the observed electronic structure. As electron doping is increased, an evolution from Mott insulator to metallic superconductor is observed as spectral weight gradually fills in the Mott gap. At the Fermi level, spectral weight appears first at $(\pi, 0)$, before growing to form a large hole pocket centered at (π, π). This behavior is similar to that seen in the $Re_{2-x}Ce_xCuO_4$ material family. We observe a two-component spectral function arising from the very

clear coexistence of a remnant lower Hubbard band with a coherent low-energy band, even for $x = 0.10$. Finally, we observe a relatively strong background intensity with a linear doping dependence. This strong background may be related to the polar surface reconstruction discussed in Chapter 8 below.

This work shows that strong local correlations remain important in the cuprates even at high doping levels. These correlations give rise to a spectrally intense remnant lower Hubbard band that coexists with coherent low-energy bands dispersing through the Fermi level. Unlike within a conventional band picture, the Mott gap in $Sr_{1-x}La_xCuO_2$ is steadily filled in with increased electron doping instead of closing abruptly. This suggests a complex doping evolution in $Sr_{1-x}La_xCuO_2$ whereby electron states shift from localized to itinerant in a continuous manner. In what ways the localized electrons in the system interact with the itinerant electrons and how that affects the interplay between magnetism and superconductivity in the material remain open questions.

CHAPTER 8

THE POLAR SURFACE RECONSTRUCTION IN $Sr_{1-x}La_xCuO_2$

The metastable infinite-layer structure lies near a manifold of other low-energy structural phases, such as the edge-sharing chain-type structure [115]. One consequence is an elevated sensitivity to oxygen stoichiometry: all as-grown films require a vacuum annealing step in order to eliminate excess oxygen and form the desired structure. Furthermore, the infinite-layer structure is intrinsically polar, alternating between charged $(CuO_2)^{2-}$ and Sr^{2+} layers. As Figure 8.1 shows, RHEED patterns before and after the oxygen reduction step show a clear structural change within the films, and LEED performed on an unreduced film shows a number of extra spots that do not correspond to the infinite-layer structure. In this chapter, we describe electron diffraction probes that show evidence of a surface reconstruction consistent with the polar nature of $Sr_{1-x}La_xCuO_2$.

8.1 Surface reconstruction

Even within the right structural phase, many nominally tetragonal transition metal oxides, such as Sr_2RuO_4 [176] or $SrTiO_3$ [177], are known to support surface reconstructions because of their complex surface chemistry. *In situ* electron diffraction probes are sensitive to such reconstructions.

8.1.1 Electron diffraction

As demonstrated in Figure 8.2, both RHEED, performed after growth at high temperature, and LEED, performed after ARPES at low temperature, indicate that some $Sr_{1-x}La_xCuO_2$ samples with low doping levels show a $p(2 \times 2)$ surface reconstruction.

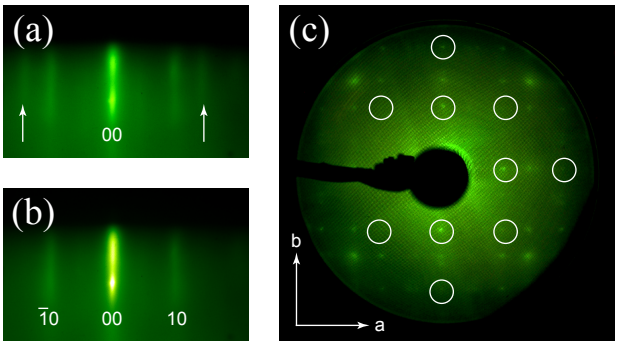

Figure 8.1: Structural change induced by the oxygen reduction step. (a) RHEED image along the [100] direction before the vacuum annealing step for an $x = 0.10$ film. White arrows highlight extra diffraction streaks present in all as-grown films. (b) RHEED image after oxygen reduction for the same film. The extra RHEED streaks vanish during the annealing step. (c) LEED image of an unannealed $x = 0.10$ film taken with 100 eV electrons. Circles show where Bragg peaks are located for films with the proper infinite-layer structure. A number of extra spots are visible.

The origin of this reconstruction is not clear, but could be related to the thermodynamically unstable polar surface of $Sr_{1-x}La_xCuO_2$. A divergence in the electric potential, a so-called polar catastrophe, can be avoided by a transfer of charge from the top surface to the bottom surface of the sample [205].

8.1.2 Model of reconstruction

The $Sr_{1-x}La_xCuO_2$ films studied in this work are terminated with a CuO_2 layer, and the extra RHEED streaks form during the vacuum annealing step. This strongly suggests that the reconstruction is related to the reduction of oxygen in the material. Furthermore, half an oxygen vacancy per unit cell will change the net charge of the terminal CuO_2 atomic layer from -2 to -1, consistent with a stabilization of the divergent surface potential. Under these constraints, just four structures (related by the trivial C_4 rotation group) are consistent with a $p(2 \times 2)$ reconstruction. One such structure is displayed in Figure 8.3.

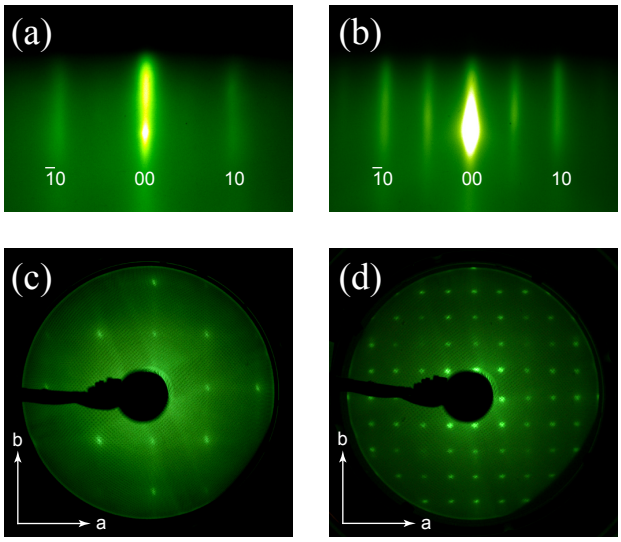

Figure 8.2: Evidence of surface reconstruction by electron diffraction. RHEED images along the [100] direction after the vacuum annealing step for $Sr_{1-x}La_xCuO_2$ samples with (a) $x = 0.10$ and (b) $x = 0$. The latter image shows extra diffraction streaks consistent with a doubled lattice constant. LEED images taken with 100 eV electrons for films with (c) $x = 0.10$ and (d) $x = 0.05$. The latter image again shows very clear evidence of a $p(2 \times 2)$ surface reconstruction.

This model of reconstruction consists of domains of ordered oxygen vacancy dimers, and the measured widths of both RHEED streaks and LEED spots indicate that such structural order persists over a length scale of ∼10 unit cells. We emphasize that the clear $(1/2, 1/2)$ diffraction peaks in LEED measurements definitively rule out the possibility that the surface consists of domains of $p(2 \times 1)$ and $p(1 \times 2)$ reconstructions, a fact greatly limiting the set of possible oxygen vacancy structures. A single domain of our proposed model would result in an anisotropic LEED structure factor. Because we observe four-fold symmetric diffraction patterns, the films likely contain domains of all four rotation states.

Despite a drastic reconstruction of the terminal CuO_2 surface of $Sr_{1-x}La_xCuO_2$, the majority of ARPES measurements are consistent with a pristine unreconstructed material. As Figure 7.5(b) shows, the Fermi surface map of the $x = 0.05$ sample shows some evidence of a $p(2\times2)$ reconstruction in the form of weak shadow bands at $(0, 0)$ and (π, π),

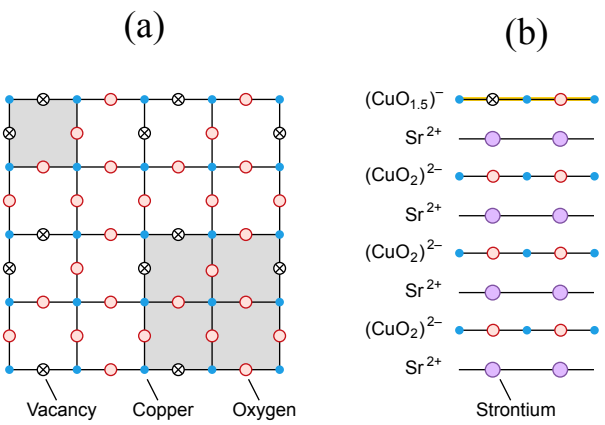

Figure 8.3: Proposed model of surface reconstruction. (a) One of four possible surface structures composed of oxygen vacancies and consistent with a $p(2 \times 2)$ reconstruction. The three other structures are related by 90° rotations. Upper left and lower right shaded squares shows the original unit cell and the doubled unit cell, respectively. (b) Layer-by-layer view showing the proposed oxygen vacancy reconstruction of the terminal CuO_2 plane (highlighted in yellow). The vacancies result in a net -1 charge per unit cell on the topmost plane, avoiding the electric potential divergence associated with a polar catastrophe.

but most ARPES data can be analyzed without considering the reconstruction. The most likely explanation is that the top layer is electronically "dead" and photoemission experiments are probing the first buried CuO_2 plane in the material. This will slightly suppress the photoemission band intensity, explaining the high relative background discussed in Section 7.4.

We note that for $x \leq 0.05$, more than half of films showed evidence of a reconstruction either by RHEED or LEED, while for $x = 0.10$, only one out of eight showed the phenomenon. Table 8.1 enumerates the fraction of ARPES films that showed evidence of the reconstruction by RHEED as a function of doping. The observed variability could be related to the fact that the formation of long-range structural order, which is necessary to observe the reconstruction by diffraction probes, may be sensitive to temperature and other effects. It is possible that the origin of the apparent doping dependence is caused by increased lanthanum dopant disorder, which could melt the oxygen vacancy ordering.

More likely, however, is that higher doping levels result in better metallic screening of the polar electric potential divergence. Whatever the case, it appears that in $Sr_{1-x}La_xCuO_2$, a polar catastrophe is avoided via a structural rather than an electronic reconstruction.

Table 8.1: Fraction of ARPES samples showing reconstruction

Doping Level	Fraction Reconstructed	Sample Size
$x = 0.01$	100%	1
$x = 0.05$	50%	2
$x = 0.10$	12.5%	8

8.2 Thickness-controlled transition during growth

Recently, Zhong *et al.* predicted that ultrathin films of polar $SrCuO_2$ grown on nonpolar $SrTiO_3$ substrates would exhibit a thickness-controlled transition from a chain-type structure to the bulk infinite-layer structure upon going from four to five unit cells [131]. As Figure 8.4(a) shows, we observe evidence for such a transition in RHEED oscillations during the growth of the first few unit cells of $SrCuO_2$ on (001) $SrTiO_3$. The first four unit cells show unstable oscillations, and only after deposition of the fourth unit cell do the oscillations stabilize. Interestingly, when growing films on polar $GdScO_3$ substrates, this behavior is suppressed and the first four deposition periods show oscillations that are qualitatively similar to those during the growth of thicker films. This structural rearrangement, occurring during the formation of the first few unit cells of a film, is related to the polar nature of the material, as mitigation of the polar catastrophe requires forming a layer of charge $+1$ (instead of $+2$ from a pristine strontium atomic plane) on the bottom face of the film. This may explain why film growth on a polar substrate such as $GdScO_3$ results in stable RHEED oscillations even during deposition of the first atomic layers.

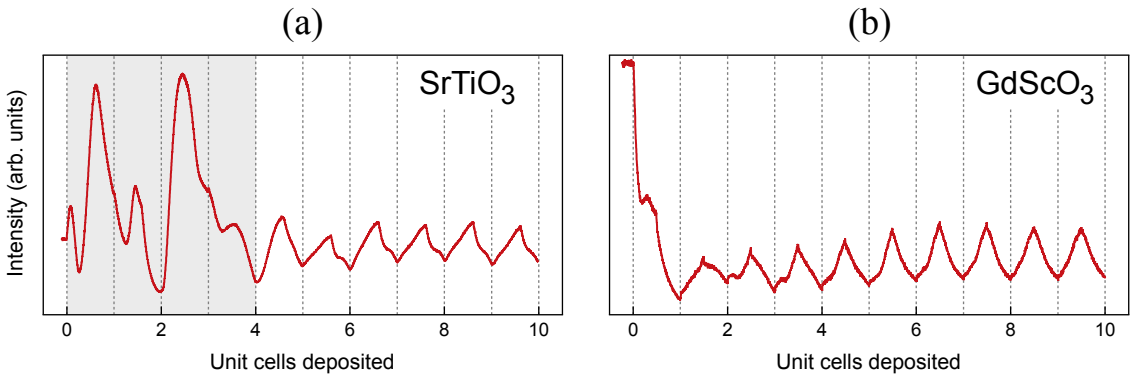

Figure 8.4: RHEED oscillations during the growth of $Sr_{1-x}La_xCuO_2$. (a) Thickness-controlled transition for a film grown on nonpolar (001) $SrTiO_3$. Deposition of the first four unit cells results in a wildly varying RHEED intensity (highlighted in gray). Stable oscillations are observed only after depositing the fourth unit cell. (b) Stable oscillations for a film grown on polar (110) $GdScO_3$.

8.3 Conclusion

In this chapter, we have studied the polar surface of thin films of $Sr_{1-x}La_xCuO_2$. Electron diffraction probes shows evidence for a surface structural reconstruction that can be explained by considering the polar nature of $Sr_{1-x}La_xCuO_2$. It appears that in $Sr_{1-x}La_xCuO_2$, a polar catastrophe is avoided via a structural rather than an electronic reconstruction. In addition, we have confirmed the theoretical prediction of a thickness-controlled transition in ultrathin films of $Sr_{1-x}La_xCuO_2$ grown on nonpolar substrates [131]. Our observation of a surface reconstruction in $Sr_{1-x}La_xCuO_2$ highlights the need for deeper investigation into the stability and structural changes that occur in polar complex oxide thin films. Both *in situ* ARPES and electron diffraction of thin film samples offer powerful probes of such changes.

CHAPTER 9

CONCLUSION

We have presented the very first direct measurements of the electronic structure of the infinite-layer cuprate $Sr_{1-x}La_xCuO_2$. Single crystals of this material cannot be grown in bulk, severely limiting the kinds of experimental probes that can be used to investigate it. To circumvent this problem, we have used epitaxial stabilization in a thin film approach, taking advantage of our unique *in situ* ARPES capabilities. Before now, most knowledge about the electron-doped side of the cuprate phase diagram has been derived by generalizing from a single material family: $Re_{2-x}Ce_xCuO_4$. Our work for the first time supplies independent confirmation of these conclusions and provides a coherent framework for understanding the generic properties of n-type cuprates. This chapter briefly summarizes our findings and offers concluding remarks and future directions of research.

9.1 Summary

We have examined thin films of $Sr_{1-x}La_xCuO_2$ with angle-resolved photoemission spectroscopy. Chapters 1, 2, and 3 introduced the field of modern condensed matter physics, including two of its most powerful experimental techniques: angle-resolved photoemission spectroscopy and molecular-beam epitaxy. Chapters 4 and 5 discussed the high-temperature superconducting cuprates, and in particular the infinite-layer material family. Chapters 6, 7, and 8 presented the major findings of this work by discussing significant experimental observations, including the coexistence of superconductivity with antiferromagnetic order, the doping evolution, and the polar surface reconstruction in $Sr_{1-x}La_xCuO_2$. Below we summarize some of the conclusions of this dissertation.

9.1.1 *In situ* ARPES

The physical union of MBE and ARPES experimental systems, although technically challenging, is an extremely fruitful endeavor. A state-of-the-art growth technique like MBE is required in order to synthesize the kinds of materials that are relevant to modern condensed matter theory, such as complex transition metal oxides, superlattices, and interfacial systems. On the other hand, a powerful technique like ARPES is necessary for an in depth study of these novel electronic systems. Only by combining the two techniques is one able to fully harness the power of each. In our case, the method has allowed a material that cannot be grown in bulk to be probed for the first time by ARPES.

9.1.2 The infinite-layer cuprate

The infinite-layer cuprate is the "theorist's cuprate" because of its extremely simple structure. It is free of magnetic rare-earth ions, oxygen chains, orthorhombic distortions, incommensurate superstructures, ordered vacancies, and other complications. Furthermore, it is the only cuprate that can be made superconducting by both electron and hole doping, making it a potential platform for decoding the complex many-body interactions responsible for high-temperature superconductivity in the cuprates. Furthermore, the ability to grow the material in thin film form opens up possibilities for engineering artificial layered systems.

In $Sr_{0.90}La_{0.10}CuO_2$, we observe a fully-formed Fermi surface with a conspicuous intensity modulation resulting from antiferromagnetic order. Based on the accuracy of the Luttinger count, the success of our simple model of magnetism, and the observation of a superconducting gap at $(\pi, 0)$, we conclude that strong antiferromagnetic tendencies and superconductivity coexist simultaneously and homogeneously in $Sr_{0.90}La_{0.10}CuO_2$. The

unusually strong coupling of electrons to (π, π) antiferromagnetism results in a Fermi surface reconstruction comprised solely of electron-like carriers, and superconductivity is restricted only to electron pockets. Furthermore, we have demonstrated that a gapping of the nodal states near $(\pi/2, \pi/2)$ by antiferromagnetism suppresses d-wave nodal quasiparticles. This picture can provide a natural explanation of the earlier conflicting reports regarding the nature of superconductivity in $Sr_{1-x}La_xCuO_2$ [143, 152, 154, 163, 164]. We have firmly established that robust antiferromagnetism and a small superconducting gap are intrinsic features of the electron-doped cuprates and not material-specific, verifying a fundamental asymmetry in the cuprate phase diagram.

In $Sr_{1-x}La_xCuO_2$ at low doping levels, a dispersive lower Hubbard band characteristic of cuprate parent compounds is observed. The t-t'-t''-J model in conjunction with Franck-Condon broadening does an excellent job of predicting the observed electronic structure. As electron doping is increased, an evolution from Mott insulator to metallic superconductor is observed as spectral weight gradually fills in the Mott gap. At the Fermi level, spectral weight appears first at $(\pi, 0)$, before growing to form a large hole pocket centered at (π, π). Somewhat surprisingly, we observe the very clear coexistence of a remnant lower Hubbard band with a coherent low-energy band even at the relatively high doping level of $x = 0.10$. This fact suggests that strong local correlations remain important in the cuprates even at high doping levels. These correlations give rise to a spectrally intense remnant lower Hubbard band that coexists with a coherent low-energy band dispersing through the Fermi level, signaling a complex doping evolution in $Sr_{1-x}La_xCuO_2$ whereby electron states shift from localized to itinerant in a continuous manner.

Finally, we have studied the polar surface of $Sr_{1-x}La_xCuO_2$. Both RHEED and LEED show evidence for a surface structural reconstruction that can be explained by considering the polar nature of the material. Indeed, it appears that in $Sr_{1-x}La_xCuO_2$, a polar

catastrophe is avoided via a structural rather than an electronic reconstruction. Our observation of a surface reconstruction in $Sr_{1-x}La_xCuO_2$ highlights the complex structural changes that are known to occur in polar complex oxide thin films.

9.1.3 Verification of theory

This work has verified a number of theoretical predictions in the literature. We have provided the first direct observation of high-T_c superconductivity in a cuprate completely devoid of hole-like carriers, as recently proposed by mean-field theory calculations [197, 198]. Furthermore, we have reported the coexistence of a low-energy band with an incoherent high-energy branch at 10% electron doping, which has been predicted by variational cluster-perturbation theory [171] and dynamical mean-field theory [172]. Both methods are successful because they explicitely take into account strong electron correlations. Finally, we have confirmed the prediction of a thickness-controlled transition in ultrathin films of $Sr_{1-x}La_xCuO_2$ grown on nonpolar $SrTiO_3$ substrates [131].

9.2 Discussion and speculation

This section discusses some of the implications of our work and speculates on its wider applicability. In particular, the coexistence of antiferromagnetic order with superconductivity and the clear intrinsic asymmetry of the cuprate phase diagram hint at important paradigm shifts in the ways that high-T_c cuprates are conceptualized.

9.2.1 Coexisting magnetism and superconductivity

Given the fact that clear signs of antiferromagnetism and superconductivity are seen simultaneously in the same sample, we may draw one of two conclusions: antiferromagnetism and superconductivity coexist homogeneously in $Sr_{1-x}La_xCuO_2$, or phase separation occurs. Indeed, the very possibility of antiferromagnetism and superconductivity coexisting has been an object of debate for many years. In $Re_{2-x}Ce_xCuO_4$, neutron scattering [167,206] and scanning tunneling spectroscopy [207] support phase separation, and in $Sr_{1-x}La_xCuO_2$, muon spin rotation indicates the formation of magnetic and nonmagnetic domains [162]. The observation of a remnant lower Hubbard band (cf. Section 7.3) may support this picture as well; the high-energy lower Hubbard band could arise via photoemission from regions of the material that are antiferromagnetic, and the low-energy band from regions that are superconducting. We hold, however, that antiferromagnetism and superconductivity coexist uniformly in $Sr_{1-x}La_xCuO_2$. Many theoretical models support this possibility [208–210], and the experimental data also appear to confirm coexistence—the success of the spin density wave model and accurate Luttinger count both require a homogeneous interaction between itinerant electrons and antiferromagnetic order. Furthermore, if phase separation is to occur, percolation of electron droplets in the CuO_2 plane is necessary for a sample to macroscopically superconduct, and there is no evidence of such a transition in $Sr_{1-x}La_xCuO_2$. An interesting theory unifying antiferromagnetism and d-wave superconductivity, $SO(5)$ theory [211], combines antiferromagnetic and superconducting order parameters into a single "superspin" object, since they have the same origin (the U-term in the Hubbard model, or equivalently, the J-interaction in the t-J model). The main conclusion of $SO(5)$ theory is that antiferromagnetism and superconductivity are complimentary in the cuprates, and a uniformly mixed phase of antiferromagnetism and superconductivity, similar to what we observe in $Sr_{1-x}La_xCuO_2$, is possible.

9.2.2 Electron-hole asymmetry and hole superconductivity

Because most coarse-grained theoretical models of high-T_c superconductivity are electron-hole symmetric, the asymmetry in the cuprate phase diagram must originate from microscopic interactions in the CuO_2 plane. The observed differences between p-type and n-type cuprates can therefore yield invaluable clues about the mechanism of high-T_c superconductivity. A longstanding theory of superconductivity is "hole superconductivity" [212], in which the presence of hole-like carriers is essential, even in electron-doped materials. Studies of $Re_{2-x}Ce_xCuO_4$ have lent support to this idea [213, 214], while a recent investigation claims that electron carriers are more important [145]. The experiments presented in this dissertation are the first direct observations of high-T_c superconductivity in a material completely absent of hole-like carriers, as the Fermi surface of $Sr_{1-x}La_xCuO_2$ consists exclusively of electron pockets. "Hole superconductivity" may therefore be falsified.

Nevertheless, it appears that holes are necessary in order to reach the highest critical temperatures in the cuprate family, and we speculate that the true pairing mechanism of the cuprates is stronger for holes. The obvious microscopic differences—holes reside on Zhang-Rice states [78] derived from O $2p_{x,y}$ orbitals and frustrate antiferromagnetism, while electrons reside on Cu $3d_{x^2-y^2}$ orbitals and merely dilute the spin system—are manifestly sensitive to spin interactions and enable us to draw conclusions about spin-based mechanisms of pairing. For example, in the "spin-bag" theory of high-T_c superconductivity [208], carriers form an attraction by sharing a local "bag" of suppressed antiferromagnetism. Electrons frustrate antiferromagnetic order to a lesser extent than holes, and the more robust antiferromagnetic order in the n-type cuprates can inhibit the spin-bag pairing mechanism, offering possible explanations for the stronger superconductivity observed in the hole-doped cuprates.

9.2.3 Differences between $Sr_{1-x}La_xCuO_2$ and $Re_{2-x}Ce_xCuO_4$

In the most well-studied $Re_{2-x}Ce_xCuO_4$ materials (*Re* = Nd and $Pr_{1-y}La$), there is evidence of significant *Re*–Cu spin coupling that modifies long-range magnetic order [83]. In contrast, in less-studied $Re_{2-x}Ce_xCuO_4$ materials (*Re* = Sm and Eu), there is no evidence for such a coupling. If we assume that it is not a coincidence that *Re* = Sm and Eu also happen to be the materials that, like $Sr_{1-x}La_xCuO_2$, exhibit a gapped nodal region and more robust antiferromagnetic order, we may speculate that *Re*–Cu coupling for *Re* = Nd and $Pr_{1-y}La$ melts the long-range antiferromagnetic order that is intrinsic to the electron-doped CuO_2 plane. This idea is supported by exact diagonalization of the t-t'-t''-J model [215], where fully gapped nodal states exist for electron doping. We also conjecture that the non-monotonic d-wave gap seen for *Re* = $Pr_{0.89}La$ [216] is the result of a partially-formed spin pseudogap at the node, and that the true underlying superconducting gap symmetry is pure d-wave. Indeed, it is conceivable that many conclusions drawn from studies of the $Re_{2-x}Ce_xCuO_4$ materials are affected by *Re*–Cu spin coupling. The ability to compare results with a completely independent and simple material family like $Sr_{1-x}La_xCuO_2$ is invaluable for establishing which conclusions are general and which are idiosyncratic to a particular material.

9.2.4 Implications for quantum oscillation experiments

We have seen that, even at dopings as large as $x = 0.10$, robust antiferromagnetic order can reconstruct the Fermi surface of $Sr_{1-x}La_xCuO_2$ in such a manner that small electron pockets are formed out of the large underlying hole pocket characteristic of the cuprates. This finding has particular relevance to the many quantum oscillation measurements of $YBa_2Cu_3O_{6+\delta}$, where the observation of small electron pockets has been a longstanding

mystery [217, 218]. Neutron scattering studies have shown that large magnetic fields, such as those applied during quantum oscillation experiments, can stabilize antiferromagnetism order [193, 194]. If the effects of this field-stabilized antiferromagnetism are similar to those of the intrinsic magnetic order in $Sr_{1-x}La_xCuO_2$ observed here, small electron pockets are a natural consequence.

9.3 Future directions

This dissertation has investigated only the fundamental and most obvious aspects of the electronic structure of $Sr_{1-x}La_xCuO_2$. It has laid down a foundation for understanding the nature of the infinite-layer cuprates in particular and the electron-doped cuprates in general, but has barely scratched the surface of experimental possibilities. Below we offer some interesting future directions of research.

9.3.1 Ultrathin films

In Chapter 8 above, we showed that ultrathin films of $Sr_{1-x}La_xCuO_2$ grown on nonpolar $SrTiO_3$ substrates undergo a thickness-controlled transition between four and five unit cells. As we have discussed, this phenomenon is most likely related to the polar nature of the material. For example, a buildup of electrostatic potential could induce the observed transition to the infinite-layer structural phase [131]. It is not clear what crystal or electronic structure forms during growth of the first few unit cells, but performing ARPES and LEED on thin films of $Sr_{1-x}La_xCuO_2$ as a function of thickness is experimentally feasible and could provide an answer.

9.3.2 Hole doping

The maximum superconducting transition temperature of the electron-doped infinite-layer cuprate is 43 K [90], while that of the hole-doped analog is substantially higher at 110 K [91]. It is not at all clear what the mechanism of hole doping is in the p-type materials. The original paper suggested that A-site deficiency plays a role, but many researchers now believe that excess oxygen atoms are the relevant operators, possibly forming oxygen-rich impurity layers that capture electrons [93–98]. Attempts to grow a superconducting hole-doped infinite-layer thin film by MBE have failed so far, but more work must be done. Possible avenues to explore include growing strontium-deficient $Sr_{1-\delta}CuO_2$ samples, or thin films of $SrCuO_{2+\delta}$ synthesized under high ozone pressure and without an oxygen reduction step. If a hole-doped film can be grown, one could imagine, for example, creating an all-cuprate p-n junction.

9.3.3 Interfacial systems

In recent years, interfaces have been recognized for their novel properties. For example, the discovery of a two-dimensional electron gas at the interface of $SrTiO_3$ and $LaAlO_3$, both insulators, sparked a rush of experimental and theoretical investigation [219]. Relevant to this work, Reference [220] contains theoretical calculations showing that a heterostructure consisting of a thin undoped cuprate on top of a manganite will result in an electron-doped interface because the Fermi level of a manganite will lie above the bottom of the upper Hubbard band of a cuprate parent compound. Growing manganite and infinite-layer thin films with MBE is relatively easy, and it should be feasible to take things one step further by growing a thin $SrCuO_2$ layer on top of a manganite film, possibly realizing an interfacially-doped cuprate as predicted by theory.

9.3.4 Superlattices

Somewhat surprisingly, much work has already been carried out in the area of infinite-layer superlattices [137]. This has mostly taken the form of growth and characterization of heterostructures consisting of stacked sequences of $SrCuO_2$ or $CaCuO_2$ with $BaCuO_2$. For example, the first superconducting infinite-layer superlattice was $CaCuO_2/(BaCuO_2)_3$, showing zero resistance at 38 K [135]. Soon thereafter, superconductivity at 50 K was observed in $(SrCuO_2)_2/(BaCuO_2)_2$ superlattices [136]. With the *in situ* ARPES approach presented in this dissertation, it is finally possible to study the detailed electronic structure of these superlattices by ARPES, taking advantage of the full capabilities of MBE. Although photoemission is surface-sensitive, superlattices with relatively thin repeat units should be amenable to study.

REFERENCES

[1] R. Mattuck, *A Guide to Feynman Diagrams in the Many-Body Problem* (McGraw-Hill, New York, 1976).

[2] L. D. Landau, Sov. Phys. JETP **3,** 920 (1957).

[3] L. D. Landau, Sov. Phys. JETP **5,** 101 (1957).

[4] L. D. Landau, Sov. Phys. JETP **8,** 70 (1959).

[5] F. Bloch, Z. Phys. **52,** 555 (1928).

[6] D. Pines and P. Nozieres, *The Theory of Quantum Liquids, Volume I* (Westview Press, Boulder, 1994).

[7] N. W. Ashcroft and N. D. Mermin, *Solid State Physics* (Brooks/Cole, Australia, 1976).

[8] H. Hertz, Ann. Phys. (Berlin) **267,** 983 (1887).

[9] P. Lenard, Ann. Phys. (Berlin) **2,** 359 (1900).

[10] A. Einstein, Ann. Phys. (Berlin) **322,** 132 (1905).

[11] M. Planck, Ann. Phys. (Berlin) **309,** 553 (1901).

[12] R. A. Millikan, Phys. Rev. **7,** 355 (1916).

[13] C. N. Berglund and W. E. Spicer, Phys. Rev. **136,** A1030 (1964).

[14] C. N. Berglund and W. E. Spicer, Phys. Rev. **136,** A1044 (1964).

[15] E. O. Kane, Phys. Rev. Lett. **12,** 97 (1964).

[16] N. V. Smith, M. M. Traum, and F. J. DiSalvo, Solid State Comm. **15,** 211 (1974).

[17] N. V. Smith, M. M. Traum, and F. J. DiSalvo, Phys. Rev. Lett. **32,** 1241 (1974).

[18] J. G. Bednorz and K. A. Müller, Z. Physik B **64,** 189 (1986).

[19] S. Hüfner, *Photoelectron Spectroscopy: Principles and Applications* (Springer, Berlin, 2003).

[20] A. Damascelli, Z. Hussain, and Z.X. Shen, Rev. Mod. Phys. **75,** 473 (2003).

[21] M. P. Seah and W. A. Dench, Surf. Interface Anal. **1,** 2 (1979).

[22] P. A. M. Dirac, Proc. R. Soc. Lond. A **114,** 243 (1927).

[23] M. Randeria, H. Ding, J.-C. Campuzano, A. Bellman, G. Jennings, T. Yokoya, T. Takahashi, H. Katayama-Yoshida, T. Mochiku, and K. Kadowaki, Phys. Rev. Lett. **74,** 4951 (1995).

[24] A. Roth, *Vacuum Technology* (North-Holland, Amsterdam, 1982).

[25] T. Kiss, T. Shimojima, K. Ishizaka, A. Chainani, T. Togashi, T. Kanai, X.-Y. Wang, C.-T. Chen, S. Watanabe, and S. Shin, Rev. Sci. Instrum. **79,** 023106 (2008).

[26] J. D. Koralek, J. F. Douglas, N. C. Plumb, J. D. Griffith, S. T. Cundiff, H. C. Kapteyn, M. M. Murnane, and D. S. Dessau, Rev. Sci. Instrum. **78,** 053905 (2007).

[27] S. Souma, T. Sato, T. Takahashi, and P. Baltzer, Rev. Sci. Instrum. **78,** 123104 (2007).

[28] S. Suga, A. Sekiyama, G. Funabashi, J. Yamaguchi, M. Kimura, M. Tsujibayashi, T. Uyama, H. Sugiyama, Y. Tomida, G. Kuwahara, S. Kitayama, K. Fukushima, K. Kimura, T. Yokoi, K. Murakami, H. Fujiwara, Y. Saitoh, L. Plucinski, and C. M. Schneider, Rev. Sci. Instrum. **81,** 105111 (2010).

[29] J. W. Harter, P. D. C. King, E. J. Monkman, D. E. Shai, Y. Nie, M. Uchida, B. Burganov, S. Chatterjee, and K. M. Shen, Rev. Sci. Instrum. **83,** 113103 (2012).

[30] A. Y. Cho and J. R. Arthur, Prog. Solid State Chem. **10,** 157 (1975).

[31] D. T. J. Hurle, *Handbook of Crystal Growth, Volume 3a: Thin Films and Epitaxy* (North-Holland, Amsterdam, 1994).

[32] D. C. Tsui, H. L. Stormer, and A. C. Gossard, Phys. Rev. Lett. **48,** 1559 (1982).

[33] K. Seshan, *Handbook of Thin Film Deposition: Processes and Technologies* (William Andrew Inc., New York, 2002).

[34] K. Ploog, A. Fischer, R. Trommer, and M. Hirose, J. Vac. Sci. Technol. **16,** 290 (1979).

[35] R. A. Betts and C. W. Pitt, Electron. Lett. **21,** 960 (1985).

[36] W. A. Doolittle, A. G. Carver, and W. Henderson, J. Vac. Sci. Technol. B **23,** 1272 (2005).

[37] S. Hosokawa and S. Ichimura, Rev. Sci. Instrum. **62,** 1614 (1991).

[38] C. D. Theis and D. G. Schlom, J. Vac. Sci. Technol. A **14,** 2677 (1996).

[39] D. G. Schlom, J. H. Haeni, J. Lettieri, C. D. Theis, W. Tian, J. C. Jiang, and X. Q. Pan, Mater. Sci. Eng. B **87,** 281 (2001).

[40] J. H. Haeni, C. D. Theis, D. G. Schlom, W. Tian, X. Q. Pan, H. Chang, I. Takeuchi, and X.-D. Xiang, Appl. Phys. Lett. **78,** 3292 (2001).

[41] S. N. Ruddlesden and P. Popper, Acta Cryst. **10,** 538 (1957).

[42] S. N. Ruddlesden and P. Popper, Acta Cryst. **11,** 54 (1958).

[43] Haynes International, Inc., Kokomo, Indiana.

[44] R. F. C. Farrow, *Molecular Beam Epitaxy: Applications to Key Materials* (Noyes Publications, New Jersey, 1995).

[45] M. Knudsen, Ann. Phys. (Leipzig) **4,** 999 (1909).

[46] Veeco Instruments, Inc., Plainview, New York.

[47] E. Coleman, T. Siegrist, D. A. Mixon, P. L. Trevor, and D. J. Trevor, J. Vac. Sci. Technol. A **9,** 2408 (1991).

[48] V. Zhukov, I. Popova, and J. T. Yates, J. Vac. Sci. Technol. A **18,** 992 (2000).

[49] J. E. Mahan, K. M. Geib, G. Y. Robinson, and R. G. Long, J. Vac. Sci. Technol. A **8,** 3692 (1990).

[50] J. H. Haeni, C. D. Theis, and D. G. Schlom, J. Electroceram. **4,** 385 (2000).

[51] M. Volmer and A. Weber, Z. Phys. Chem. **119,** 277 (1926).

[52] I. N. Stranski and L. Krastanow, Akad. Wiss. Wien Math.-Naturwiss. Kl. IIb **146,** 797 (1939).

[53] F. C. Frank and J. H. van der Merwe, Proc. R. Soc. London, Ser. A **198,** 205 (1949).

[54] K. Byrappa and T. Ohachi, *Crystal Growth Technology* (William Andrew Inc., New York, 2003).

[55] S. Clarke and D. D. Vvedensky, Phys. Rev. Lett. **58,** 2235 (1987).

[56] G. Koster, B. L. Kropman, G. J. H. M. Rijnders, D. H. A. Blank, and H. Rogalla, Appl. Phys. Lett. **73,** 2920 (1998).

[57] J. E. Kleibeuker, G. Koster, W. Siemons, D. Dubbink, B. Kuiper, J. L. Blok, C.-H. Yang, J. Ravichandran, R. Ramesh, J. E. ten Elshof, D. H. A. Blank, and G. Rijnders, Adv. Funct. Mater. **20,** 3490 (2010).

[58] H. K. Onnes, Leiden Comm. **120b, 122b, 124c,** (1911).

[59] M. Tinkham, *Introduction to Superconductivity* (Dover Publications, New York, 1996).

[60] W. Meissner and R. Ochsenfield, Naturwissenschaften **21,** 787 (1933).

[61] F. Steglich, J. Aarts, C. D. Bredl, W. Lieke, D. Meschede, W. Franz, and H. Schäfer, Phys. Rev. Lett. **43,** 1892 (1979).

[62] M. K. Wu, J. R. Ashburn, C. J. Torng, P. H. Hor, R. L. Meng, L. Gao, Z. J. Huang, Y. Q. Wang, and C. W. Chu, Phys. Rev. Lett. **58,** 908 (1987).

[63] Y. Kamihara, T. Watanabe, M. Hirano, and H. Hosono, J. Am. Chem. Soc. **130,** 3296 (2008).

[64] F. London and H. London, Proc. Roy. Soc. (London) **A149,** 71 (1935).

[65] V. L. Ginzburg and L. D. Landau, Zh. Eksperum. i Teor. Fiz. **20,** 1064 (1950).

[66] J. Bardeen, L. N. Cooper, and J. R. Schrieffer, Phys. Rev. **108,** 1175 (1957).

[67] A. A. Abrikosov, Zh. Eksperum. i Teor. Fiz. **32,** 1442 (1957).

[68] L. N. Cooper, Phys. Rev. **104,** 1189 (1956).

[69] H. Fröhlich, Phys. Rev. **79,** 845 (1950).

[70] E. Maxwell, Phys. Rev. **78,** 477 (1950).

[71] C. A. Reynolds, B. Serin, W. H. Wright, and L. B. Nesbitt, Phys. Rev. **78,** 487 (1950).

[72] A. B. Migdal, Zh. Eksperum. i Teor. Fiz. **34,** 1438 (1958).

[73] G. M. Eliashberg, Zh. Eksperum. i Teor. Fiz. **38,** 966 (1960).

[74] A. J. Leggett, Nature Phys. **2,** 134 (2006).

[75] D. J. Van Harlingen, Rev. Mod. Phys. **67,** 515 (1995).

[76] C. C. Tsuei and J. R. Kirtley, Rev. Mod. Phys. **72,** 969 (2000).

[77] P. W. Anderson, Science **235,** 1196 (1987).

[78] F. C. Zhang and T. M. Rice, Phys. Rev. B **37,** 3759 (1988).

[79] N. F. Mott, Proc. Phys. Soc. A **62,** 416 (1949).

[80] J. Hubbard, Proc. Roy. Soc. (London) **276,** 1365 (1963).

[81] J. Zaanan, G. A. Sawatzky, and J. W. Allen, Phys. Rev. Lett. **55,** 418 (1985).

[82] Y. Tokura, H. Takagi, and S. Uchida, Nature **337,** 345 (1989).

[83] N. P. Armitage, P. Fournier, and R. L. Greene, Rev. Mod. Phys. **82,** 2421 (2010).

[84] M. Matsuda, Y. Endoh, K. Yamada, H. Kojima, I. Tanaka, R. J. Birgeneau, M. A. Kastner, and G. Shirane, Phys. Rev. B **45,** 12548 (1992).

[85] A. Aharony, R. J. Birgeneau, A. Coniglio, M. A. Kastner, and H. E. Stanley, Phys. Rev. Lett. **60,** 1330 (1988).

[86] M. Gurvitch and A. T. Fiory, Phys. Rev. Lett. **59,** 1337 (1987).

[87] H. Takagi, B. Batlogg, H. L. Kao, J. Kwo, R. J. Cava, J. J. Krajewski, and W. F. Peck, Jr., Phys. Rev. Lett. **69,** 2975 (1992).

[88] C. C. Tsuei, A. Gupta and G. Koren, Physica C **161,** 415 (1989).

[89] T. Siegrist, S. M. Zahurak, D. W. Murphy, and R. S. Roth, Science **334,** 231 (1988).

[90] M. G. Smith, A. Manthiram, J. Zhou, J. B. Goodenough, and J. T. Markert, Nature **351,** 549 (1991).

[91] M. Azuma, Z. Hiroi, M. Takano, Y. Bando, and Y. Takeda, Nature **356,** 775 (1992).

[92] G. Er, S. Kikkawa, M. Takahashi, and F. Kanamaru, Physica C **276,** 315 (1997).

[93] S. Adachi, H. Yamauchi, S. Tanaka, and N. Môri, Physica C **208,** 226 (1993).

[94] M. Kawaii, Z. Liu, R. Sekine, and H. Koinuma, Jpn. J. Appl. Phys. **32,** 1208 (1993).

[95] Z. Hiroi, M. Azuma, M. Takano, and Y. Takeda, Physica C **208,** 286 (1993).

[96] R. Feenstra, X. Li, M. Kanai, T. Kawai, S. Kawai, J. D. Budai, E. C. Jones, Y. R. Sun, J. R. Thompson, S. J. Pennycook, D. K. Christen, Physica C **224,** 300 (1994).

[97] H. Zhang, Y. Y. Wang, H. Zhang, V. P. Dravid, L. D. Marks, P. D. Han, D. A. Payne, P. G. Radaelli, and J. D. Jorgensen, Nature **370,** 352 (1994).

[98] S. Tao and H.-U. Nissen, Phys. Rev. B **51,** 8638 (1995).

[99] S. Oh and J. N. Eckstein, Thin Solid Films **483,** 301 (2005).

[100] W. Jiang, J. L. Peng, Z. Y. Li, and R. L. Greene, Phys. Rev. B **47,** 8151 (1993).

[101] A. J. Schultz, J. D. Jorgensen, J. L. Peng, and R. L. Greene, Phys. Rev. B **53,** 5157 (1996).

[102] P. Richard, M. Neupane, Y.-M. Xu, P. Fournier, S. Li, P. Dai, Z. Wang, and H. Ding, Phys. Rev. Lett. **99,** 157002 (2007).

[103] P. Richard, M. Neupane, Y.-M. Xu, P. Fournier, S. Li, P. Dai, Z. Wang, and H. Ding, Physica B **403,** 1170 (2008).

[104] Z. Z. Li, V. Jovanović, H. Raffy, and S. Megtert, Physica C **469,** 73 (2009).

[105] P. Richard, G. Riou, I. Hetel, S. Jandl, M. Poirier, and P. Fournier, Phys. Rev. B **70,** 064513 (2004).

[106] G. Riou, P. Richard, S. Jandl, M. Poirier, P. Fournier, V. Nekvasil, S. N. Barilo, and L. A. Kurnevich, Phys. Rev. B **69,** 024511 (2004).

[107] H. J. Kang, P. Dai, B. J. Campbell, P. J. Chupas, S. Rosenkranz, P. L. Lee, Q. Huang, S. Li, S. Komiya, and Y. Ando, Nat. Mater. **6,** 224 (2007).

[108] Y.-L. Wang, Y. Huang, L. Shan, S. L. Li, P. Dai, C. Ren, and H.-H. Wen, Phys. Rev. B **80,** 094513 (2009).

[109] J. D. Jorgensen, P. G. Radaelli, D. G. Hinks, J. L. Wagner, S. Kikkawa, G. Er, and F. Kanamaru, Phys. Rev. B **47,** 14654 (1993).

[110] G. H. Kwei, S.-W. Cheong, Z. Fisk, F. H. Garzon, J. A. Goldstone, and J. D. Thompson, Phys. Rev. B **40,** 9370 (1989).

[111] A. Nath, N. S. Kopelev, V. Chechersky, J.-L. Peng, R. L. Greene, B. O, M. I. Larkin, and J. T. Markert, Science **265,** 73 (1994).

[112] P. G. Radaelli, J. D. Jorgensen, A. J. Schultz, J. L. Peng, and R. L. Greene, Phys. Rev. B **49,** 15322 (1994).

[113] J. W. Harter, B. M. Andersen, J. Bobroff, M. Gabay, and P. J. Hirschfeld, Phys. Rev. B **75,** 054520 (2007).

[114] D. Song, S. R. Park, C. Kim, Y. Kim, C. Leem, S. Choi, W. Jung, Y. Koh, G. Han, Y. Yoshida, H. Eisaki, D. H. Lu, Z.-X. Shen, and C. Kim, Phys. Rev. B **86,** 144520 (2012).

[115] M. T. Gambardella, B. Domengès, B. Raveau, Mater. Res. Bull. **27,** 629 (1992).

[116] M. Takano, Y. Takeda, H. Okada, M. Miyamoto, and T. Kusaka, Physica C **159,** 375 (1989).

[117] M. Takano, M. Azuma, Z. Hiroi, Y. Bando, and Y. Takeda, Physica C **441,** 375 (1991).

[118] G. Er, Y. Miyamoto, F. Kanamaru and S. Kikkawa, Physica C **181,** 206 (1991).

[119] I. Yazawa, N. Terada, K. Matsutani, R. Sugise, M. Jo, and H. Ihara, Jpn. J. Appl. Phys. **29,** L566 (1990).

[120] M. Kanai, T. Kawai, and S. Kawai, Appl. Phys. Lett. **58,** 771 (1991).

[121] C. Niu and C. M. Lieber, J. Am. Chem. Soc. **114,** 3570 (1992).

[122] D. P. Norton, B. C. Chakoumakos, J. D. Budai, and D. H. Lowndes, Appl. Phys. Lett. **62,** 1679 (1993).

[123] H. Adachi, T. Satoh, Y. Ichikawa, K. Setsune, and K. Wasa, Physica C **196,** 14 (1992).

[124] V. P. Jovanović, L. Fruchter, Z. Z. Li, and H. Raffy, Phys. Rev. B **81,** 134520 (2010).

[125] V. P. Jovanović, Z. Z. Li, and H. Raffy, Supercond. Sci. Technol. **24,** 055002 (2011).

[126] S. Karimoto, K. Ueda, M. Naito, and T. Imai, Appl. Phys. Lett. **79,** 2767 (2001).

[127] S. Karimoto and M. Naito, Appl. Phys. Lett. **84,** 2136 (2004).

[128] L. Maritato, A. Galdi, P. Orgiani, J. W. Harter, J. Schubert, K. M. Shen, and D. G. Schlom, J. Appl. Phys. **113,** 053911 (2013).

[129] V. Leca, D. H. A. Blank, G. Rijnders, S. Bals, and G. van Tendeloo, Appl. Phys. Lett. **89,** 092504 (2006).

[130] V. Leca, G. Vişănescu, C. Back, R. Kleiner, and D. Koelle, Appl. Phys. A **93,** 779 (2008).

[131] Z. Zhong, G. Koster, and P. J. Kelly, Phys. Rev. B **85,** 121411R (2012).

[132] B. Mercey, A. Gupta, M. Hervieu, and B. Raveau, J. Solid State Chem. **116,** 37 (1995).

[133] Z. Liu, T. Hanada, R. Sekine, M. Kawai, and H. Koinuma, Appl. Phys. Lett. **65,** 1717 (1994).

[134] M. Yoshimoto, H. Nagata, J. Gong, H. Ohkubo, and H. Koinuma, Physica C **185,** 2085 (1991).

[135] X. Li, T. Kawai, S. Kawai, Jpn. J. Appl. Phys. **33,** L18 (1994).

[136] D. P. Norton, B. C. Chakoumakos, J. D. Budai, D. H. Lowndes, B. C. Sales, J. R. Thompson, and D. K. Christen, Science **265,** 2074 (1994).

[137] G. Balestrino and A. Tebano, Supercond. Sci. Technol. **16,** R29 (2003).

[138] S. Zhu, D. P. Norton, J. E. Chamberlain, F. Shahedipour, and H. W. White, Phys. Rev. B **54,** 97 (1996).

[139] S. Colonna, F. Arciprete, A. Balzarotti, G. Balestrino, P. G. Medaglia, and G. Petrocelli, Physica C **334,** 64 (2000).

[140] E. C. Jones, D. P. Norton, B. C. Sales, D. H. Lowndes, and R. Feenstra, Phys. Rev. B **52,** 743R (1995).

[141] G. V. M. Williams, R. Dupree, A. Howes, S. Krämer, H. J. Trodahl, C. U. Jung, M.-S. Park, and S.-I. Lee, Phys. Rev. B **65,** 224520 (2002).

[142] D. P. Norton, B. C. Chakoumakos, J. D. Budai, and D. H. Lowndes, Phys. Stat. Sol. (b) **236,** 143 (2003).

[143] Z. Y. Liu, H. H. Wen, L. Shan, H. P. Yang, X. F. Lu, H. Gao, M.-S. Park, C. U. Jung and S.-I. Lee, Europhys. Lett. **69,** 263 (2005).

[144] V. P. Jovanović, Z. Z. Li, H. Raffy, A. A. Sinchenko, and P. Monceau, Phys. Rev. B **80,** 024501 (2009).

[145] L. Fruchter, F. Bouquet, and Z. Z. Li, Phys. Rev. B **84,** 092502 (2011).

[146] J. Tomaschko, V. Leca, T. Selistrovski, R. Kleiner, and D. Koelle, Phys. Rev. B **84,** 214507 (2011).

[147] T. Imai, C. F. Slichter, J. L. Cobb, and J. T. Markert, J. Phys. Chem. Solids **56,** 1921 (1995).

[148] K. Mikhalev, K. Kumagai, Y. Furukawa, V. Bobrovskii, T. Dyachkova, N. Kadirova, and A. Gerashenko, Physica C **304,** 165 (1998).

[149] R. S. Liu, J. M. Chen, P. Nachimuthu, R. Gundakaram, C. U. Jung, J. Y. Kim, and S. I. Lee, Solid State Comm. **118,** 367 (2001).

[150] R. P. Vasquez, C. U. Jung, J. Y. Kim, M.-S. Park, H.-J. Kim, and S.-I. Lee, J. Phys. Condens. Matter **13,** 7977 (2001).

[151] J. Tomaschko, C. Raisch, V. Leca, T. Chassé, R. Kleiner, and D. Koelle, Phys. Rev. B **84,** 064521 (2011).

[152] C.-T. Chen, P. Seneor, N.-C. Yeh, R. P. Vasquez, L. D. Bell, C. U. Jung, J. Y. Kim, M.-S. Park, H.-J. Kim, and S.-I. Lee, Phys. Rev. Lett. **88,** 227002 (2002).

[153] M. L. Teague, A. D. Beyer, M. S. Grinolds, S. I. Lee, and N.-C. Yeh, Europhys. Lett. **85,** 17004 (2009).

[154] C. U. Jung, J. Y. Kim, M.-S. Park, M.-S. Kim, H.-J. Kim, S. Y. Lee, and S.-I. Lee, Phys. Rev. B **65,** 172501 (2002).

[155] C. U. Jung, J. Y. Kim, S.-I. Lee, M.-S. Kim, Physica C **391,** 319 (2003).

[156] M.-S. Kim, T. R. Lemberger, C. U. Jung, J.-H. Choi, J. Y. Kim, H.-J. Kim, and S.-I. Lee, Phys. Rev. B **66,** 214509 (2002).

[157] V. S. Zapf, N.-C. Yeh, A. D. Beyer, C. R. Hughes, C. H. Mielke, N. Harrison, M. S. Park, K. H. Kim, and S.-I. Lee, Phys. Rev. B **71,** 134526 (2005).

[158] H. C. Kima, M.-H. Kima, M. H. Junga, M.-S. Park, S.-I. Lee, Physica C **378,** 886 (2006).

[159] D. Di Castro, R. Khasanov, A. Shengelaya, K. Conder, D.-J. Jang, M.-S. Park, S.-I. Lee, and H. Keller, J. Phys. Condens. Matter **21,** 275701 (2009).

[160] L. Fruchter, V. Jovanovic, H. Raffy, S. Labdi, F. Bouquet, and Z. Z. Li, Phys. Rev. B **82,** 144529 (2010).

[161] A. Shengelaya, R. Khasanov, D. G. Eshchenko, D. Di Castro, I. M. Savić, M. S. Park, K. H. Kim, S.-I. Lee, K. A. Müller, and H. Keller, Phys. Rev. Lett. **94,** 127001 (2005).

[162] K. H. Satoh, S. Takeshita, A. Koda, R. Kadono, K. Ishida, S. Pyon, T. Sasagawa, and H. Takagi, Phys. Rev. B **77,** 224503 (2008).

[163] R. Khasanov, A. Shengelaya, A. Maisuradze, D. Di Castro, I. M. Savić, S. Weyeneth, M. S. Park, D. J. Jang, S.-I. Lee, and H. Keller, Phys. Rev. B **77,** 184512 (2008).

[164] J. S. White, E. M. Forgan, M. Laver, P. S. Häfliger, R. Khasanov, R. Cubitt, C. D. Dewhurst, M.-S. Park, D.-J. Jang, H.-G. Lee, and S.-I. Lee, J. Phys. Condens. Matter **20,** 104237 (2008).

[165] P. Orgiani, C. Adamo, C. Barone, A. Galdi, A. Y. Petrov, D. G. Schlom, and L. Maritato, Phys. Rev. B **76,** 012404 (2007).

[166] J. Tomaschko, S. Scharinger, V. Leca, J. Nagel, M. Kemmler, T. Selistrovski, D. Koelle, and R. Kleiner, Phys. Rev. B **86,** 094509 (2012).

[167] K. Yamada, K. Kurahashi, T. Uefuji, M. Fujita, S. Park, S.-H. Lee, and Y. Endoh, Phys. Rev. Lett. **90,** 137004 (2003).

[168] E. M. Motoyama, G. Yu, I. M. Vishik, O. P. Vajk, P. K. Mang, and M. Greven, Nature **445,** 186 (2007).

[169] D. L. Feng, D. H. Lu, K. M. Shen, C. Kim, H. Eisaki, A. Damascelli, R. Yoshizaki, J.-I. Shimoyama, K. Kishio, G. D. Gu, S. Oh, A. Andrus, J. O'Donnell, J. N. Eckstein, and Z.-X. Shen, Science **289,** 277 (2000).

[170] A. Ino, T. Mizokawa, A. Fujimori, K. Tamasaku, H. Eisaki, S. Uchida, T. Kimura, T. Sasagawa, and K. Kishio, Phys. Rev. Lett. **79,** 2101 (1997).

[171] D. Sénéchal, , Phys. Rev. Lett. **94,** 156404 (2005).

[172] C. Weber, K. Haule, and G. Kotliar, Nature Phys. **6,** 574 (2010).

[173] J. W. Harter, L. Maritato, D. E. Shai, E. J. Monkman, Y. Nie, D. G. Schlom, and K. M. Shen, Phys. Rev. Lett. **109,** 267001 (2012).

[174] R. Uecker, B. Velickov, D. Klimm, R. Bertram, M. Bernhagen, M. Rabe, M. Albrecht, R. Fornari, and D. G. Schlom, J. Cryst. Growth **310,** 2649 (2008).

[175] A. Kaminski, S. Rosenkranz, H. M. Fretwell, J. Mesot, M. Randeria, J. C. Campuzano, M. R. Norman, Z. Z. Li, H. Raffy, T. Sato, T. Takahashi, and K. Kadowaki, Phys. Rev. B **69,** 212509 (2004).

[176] A. Damascelli, D. H. Lu, K. M. Shen, N. P. Armitage, F. Ronning, D. L. Feng, C. Kim, Z.-X. Shen, T. Kimura, Y. Tokura, Z. Q. Mao, and Y. Maeno, Phys. Rev. Lett. **85,** 5194 (2000).

[177] N. Erdman, K. R. Poeppelmeier, M. Asta, O. Warschkow, D. E. Ellis, and L. D. Marks, Nature **419,** 55 (2002).

[178] H. Kiessig, Ann. Phys. (Berlin) **10,** 715 (1931).

[179] H. Kiessig, Ann. Phys. (Berlin) **10,** 769 (1931).

[180] K. L. Saenger and I. C. Noyan, J. Appl. Phys. **89,** 3125 (2001).

[181] J. J. Yeh and I. Lindau, At. Data Nucl. Data Tables **32,** 1 (1985).

[182] B. L. Henke, E. M. Gullikson, and J. C. Davis, At. Data Nucl. Data Tables **54,** 181 (1993).

[183] M. Eschrig and M. R. Norman, Phys. Rev. Lett. **89,** 277005 (2002).

[184] N. P. Armitage, D. H. Lu, C. Kim, A. Damascelli, K. M. Shen, F. Ronning, D. L. Feng, P. Bogdanov, Z.-X. Shen, Y. Onose, Y. Taguchi, Y. Tokura, P. K. Mang, N. Kaneko, and M. Greven, Phys. Rev. Lett. **87,** 147003 (2001).

[185] H. Matsui, K. Terashima, T. Sato, T. Takahashi, S.-C. Wang, H.-B. Yang, H. Ding, T. Uefuji, and K. Yamada, Phys. Rev. Lett. **94,** 047005 (2005).

[186] S. R. Park, Y. S. Roh, Y. K. Yoon, C. S. Leem, J. H. Kim, B. J. Kim, H. Koh, H. Eisaki, N. P. Armitage, and C. Kim, Phys. Rev. B **75,** 060501 (2007).

[187] S. Chakravarty, R. B. Laughlin, D. K. Morr, and C. Nayak, *Phys. Rev. B* **63,** 094503 (2001).

[188] P. Blaha, K. Schwarz, G. K. H. Madsen, D. Kvasnicka, and J. Luitz, *WIEN2K, An Augmented Plane Wave + Local Orbitals Program for Calculating Crystal Properties* (Karlheinz Schwarz, Techn. Universität Wien, Austria, 2001).

[189] L. F. Mattheiss and D. R. Hamann, Phys. Rev. B **40,** 2217 (1989).

[190] M. Ikeda, T. Yoshida, A. Fujimori, M. Kubota, K. Ono, H. Das, T. Saha-Dasgupta, K. Unozawa, Y. Kaga, T. Sasagawa, and H. Takagi, Phys. Rev. B **80,** 014510 (2009).

[191] J.-Q. Meng, M. Brunner, K.-H. Kim, H.-G. Lee, S.-I. Lee, J. S. Wen, Z. J. Xu, G. D. Gu, and G.-H. Gweon, Phys. Rev. B **84,** 060513R (2011).

[192] K. M. Shen, F. Ronning, D. H. Lu, F. Baumberger, N. J. C. Ingle, W. S. Lee, W. Meevasana, Y. Kohsaka, M. Azuma, M. Takano, H. Takagi, Z.-X. Shen, Science **307,** 901 (2005).

[193] B. Lake, H. M. Ronnow, N. B. Christensen, G. Aeppli, K. Lefmann, D. F. McMorrow, P. Vorderwisch, P. Smeibidl, N. Mangkorntong, T. Sasagawa, M. Nohara, H. Takagi, and T. E. Mason, Nature **415,** 299 (2002).

[194] D. Haug, V. Hinkov, A. Suchaneck, D. S. Inosov, N. B. Christensen, C. Niedermayer, P. Bourges, Y. Sidis, J. T. Park, A. Ivanov, C. T. Lin, J. Mesot, and B. Keimer, Phys. Rev. Lett. **103,** 017001 (2009).

[195] N. P. Armitage, D. H. Lu, D. L. Feng, C. Kim, A. Damascelli, K. M. Shen, F. Ronning, Z.-X. Shen, Y. Onose, Y. Taguchi, and Y. Tokura, Phys. Rev. Lett. **86,** 1126 (2001).

[196] I. Diamant, R. L. Greene, and Y. Dagan, Phys. Rev. B **80,** 012508 (2009).

[197] Q. Yuan, X.-Z. Yan, and C. S. Ting, Phys. Rev. B **74,** 214503 (2006).

[198] T. Das, R. S. Markiewicz, and A. Bansil, Phys. Rev. Lett. **98,** 197004 (2007).

[199] E. Dagotto, Rev. Mod. Phys. **66**, 763 (1994).

[200] K. M. Shen, F. Ronning, D. H. Lu, W. S. Lee, N. J. C. Ingle, W. Meevasana, F. Baumberger, A. Damascelli, N. P. Armitage, L. L. Miller, Y. Kohsaka, M. Azuma, M. Takano, H. Takagi, and Z.-X. Shen, Phys. Rev. Lett. **93**, 267002 (2004).

[201] N. P. Armitage, F. Ronning, D. H. Lu, A. Damascelli, K. M. Shen, D. L. Feng, H. Eisaki, Z.-X. Shen, P. K. Mang, N. Kaneko, M. Greven, Y. Onose, Y. Taguchi, and Y. Tokura, Phys. Rev. Lett. **88**, 257001 (2002).

[202] T. Tohyama and S. Maekawa, Supercond. Sci. Technol. **13,** R17 (2000).

[203] B. Moritz, F. Schmitt, W. Meevasana, S. Johnston, E. M. Motoyama, M. Greven, D. H. Lu, C. Kim, R. T. Scalettar, Z.-X. Shen, and T. P. Devereaux, New J. Phys. **11,** 093020 (2009).

[204] N. P. Armitage, D. H. Lu, C. Kim, A. Damascelli, K. M. Shen, F. Ronning, D. L. Feng, P. Bogdanov, Z.-X. Shen, Y. Onose, Y. Taguchi, Y. Tokura, P. K. Mang, N. Kaneko, and M. Greven, Phys. Rev. Lett. **87,** 147003 (2001).

[205] N. Nakagawa, H. Y. Hwang, and D. A. Muller, Nature Mater. **5,** 204 (2006).

[206] P. Dai, H. J. Kang, H. A. Mook, M. Matsuura, J. W. Lynn, Y. Kurita, S. Komiya, and Y. Ando, Phys. Rev. B **71,** 100502R (2005).

[207] J. Zhao, F. C. Niestemski, S. Kunwar, S. Li, P. Steffens, A. Hiess, H. J. Kang, S. D. Wilson, Z. Wang, P. Dai, and V. Madhavan, Nature Phys. **7,** 719 (2011).

[208] J. R. Schrieffer, X.-G. Wen, and S.-C. Zhang, Phys. Rev. Lett. **60,** 944 (1988).

[209] M. Capone and G. Kotliar, Phys. Rev. B **74,** 054513 (2006).

[210] T. Das, R. S. Markiewicz, and A. Bansil, Phys. Rev. B **74,** 020506R (2006).

[211] S.-C. Zhang, Science **275,** 1089 (1997).

[212] J. E. Hirsch, Phys. Lett. A **134,** 451 (1989).

[213] M. M. Qazilbash, A. Koitzsch, B. S. Dennis, A. Gozar, H. Balci, C. A. Kendziora, R. L. Greene, and G. Blumberg, Phys. Rev. B **72,** 214510 (2005).

[214] Y. Dagan and R. L. Greene, Phys. Rev. B **74,** 024506 (2007).

[215] T. Tohyama, Phys. Rev. B **70,** 174517 (2004).

[216] H. Matsui, K. Terashima, T. Sato, T. Takahashi, M. Fujita, and K. Yamada, Phys. Rev. Lett. **95,** 017003 (2005).

[217] C. Jaudet, D. Vignolles, A. Audouard, J. Levallois, D. LeBoeuf, N. Doiron-Leyraud, B. Vignolle, M. Nardone, A. Zitouni, R. Liang, D. A. Bonn, W. N. Hardy, L. Taillefer, and C. Proust, Phys. Rev. Lett. **100,** 187005 (2008).

[218] S. E. Sebastian, N. Harrison, C. H. Mielke, R. Liang, D. A. Bonn, W. N. Hardy, and G. G. Lonzarich, Phys. Rev. Lett. **103,** 256405 (2009).

[219] A. Ohtomo and H. Y. Hwang, Nature **427,** 423 (2004).

[220] S. Yunoki, A. Moreo, E. Dagotto, S. Okamoto, S. S. Kancharla, and A. Fujimori, Phys. Rev. B **76,** 064532 (2007).